NORTHWESTERN UNIVERSITY

Exploration of Light-Absorbing Nanomaterials for Organic Photocatalysis and Solar Fuels

Production

A DISSERTATION

SUBMITTED TO THE GRADUATE SCHOOL

IN PARTIAL FULFILLMENT OF THE REQUIREMENTS

for the degree

DOCTOR OF PHILOSOPHY

Field of Chemistry

By

Benjamin Nagasing

EVANSTON, ILLINOIS

March 2021

Abstract

Exploration of Light-Absorbing Nanomaterials for Organic Photocatalysis and Solar Fuels

Production

Benjamin Nagasing

This dissertation investigates the use of organic and semiconductor nanomaterials as chromophores in solar fuels production and energy transfer-mediated [2+2] cycloadditions. A series of novel *N*-annulated perylene chromophore amphiphiles was synthesized via a modular synthesis. These perylene amphiphiles were found to self-assemble in aqueous solution, forming extended ribbon-like nanostructures that could form gels in the presence of cross-linking divalent salts. The assemblies exhibited weak electronic coupling, unlike similar previously studied molecules, likely due to an edge-to-face interaction between perylene units. The assemblies were used to photosensitize a CO_2 reduction catalyst which photocatalyzed the reduction of CO_2 to CO under aqueous conditions in the presence of light and a sacrificial hole quencher. Photosensitization of a similar catalyst with $CuInS_2$@ZnS quantum dots (QDs) was also explored; specifically, potential binding interactions between the catalyst and QDs' surface was investigated by ^1H NMR and UV-vis spectroscopies as well as cyclic voltammetry and X-ray techniques. Finally, QDs were investigated as triplet sensitizers of a [2+2] cycloaddition between olefins and imines to form azetidines. Imine substrates were found to undergo unproductive isomerization even when sensitized by QDs with excited state energies below that of the imines due to non-vertical energy transfer. This thesis demonstrates the challenges and potential of designing both organic soft material and semiconductor nanomaterials for photocatalytic applications.

Acknowledgments

The completion of this very modest dissertation was an extremely challenging and humbling task for me and pushed me to grow both personally and professionally. I could not have made it to this point without the support of many friends, family, mentors, colleagues, and collaborators. I will try to acknowledge as many as I can below.

I must first thank my research advisor, Emily, for her unwavering patience and support. I don't think I can adequately express my gratitude in this space. I learned so much from Emily about how to ask hard, incisive scientific questions and think critically about results, among other things. She gave me a second opportunity to explore research while being open to my pursuit of alternative career paths, for which I am also very grateful.

I also thank Prof. SonBinh Nguyen and Prof. Mercouri Kanatzidis for taking the time to sit on my committee and for providing valuable feedback at various stages of my graduate studies. I thank Prof. Stupp for initially taking me into his laboratory and for creating a vibrant research environment in which I was able to learn a lot, even if it ultimately wasn't the right place for me.

I have numerous colleagues, mentors, and friends to thank: Adam Weingarten, Roman Kazantzev, Adam Dannenhoffer, Stacey Chin, Ben Jones, Adam Preslar, Leo Barreda, Mark Hendricks, Oliver Dumele, Ivan Ramos Sasselli, Francesca Arcudi, Luka Dordevic, Hiroaki Sai, Ashwin Narayanan, Jack Edelbrock, Allie Edelbrock, Nick Sather, Garrett Lau, Shichen Lian, Mohamad Kodaimati, Kaitlyn Redfern, Cameron Rogers, Rafael Lopez-Arteaga, Jack Olding, Paul Ohno, Matthew Kirschner, Aidan Caravana, Prof. Regan Thomson, all of the other members of the Weiss and Stupp labs with whom I worked and interacted, my soccer team Give 'em El,

Table of Contents

List of Figures

electrode, and Ag wire pseudoreference (a ferrocene internal standard was used and the value

List of Schemes

Chapter 1 : Introduction

1.1.   Chapter Summary

This chapter introduces the motivation for studying light-driven chemical processes, namely the potential to capture light energy from the sun and convert it into fuel or useful chemical work. Basic photophysical processes and intermolecular electron and energy transfer are first introduced, as well as the types of chromophores capable of such processes. This is followed by an introduction to solar fuels, specifically the motivation for and challenges of photocatalytic CO_2 reduction. Supramolecular chemistry is briefly discussed as a set of design principles to potentially improve the photophysical properties of chromophores or facilitate their interactions with external catalysts and substrates for photocatalytic applications.

1.2.   The Need for Alternative Fuels and Sustainable Chemical Processes

Global energy demand is rapidly increasing and expected to at least double by the year 2050.[2] The vast majority of the world's energy supply is currently derived from non-renewable, carbon-based sources such as oil and natural gas, the waste products of which are straining the environment to its limit.[3] Major consensus has been reached that these greenhouse gas emissions are the main driver of global warming. Avoiding an increase in average world temperature of more than 1.5 °C is critical to prevent widespread irreparable damage of ecosystems, coastal cities, and populations in arid climates, as well as other negative outcomes. These realities necessitate the immediate development of renewable, carbon-neutral fuels derived from solar, wind, or hydrothermal power. Driving other processes, such as organic chemical reactions, using renewable energy sources is also a key goal to reduce overall nonrenewable fuels consumption.[4-5]

1.3. Photochemistry

1.3.1 Introduction to photophysics and photochemistry
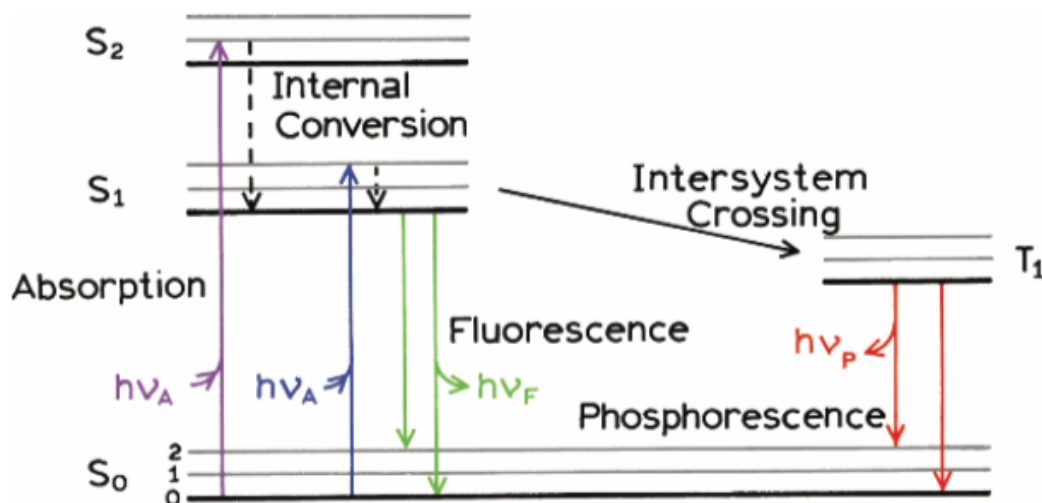
Scheme 1.1. Jablonski diagram outlining photophysical processes that occur within a chromophore. Adapted from reference.[1]

The chemistry of light-driven processes is a rich and complex field. This section aims only to provide a brief overview of the basic photophysical and photochemical processes that enable the transformation of light energy into chemical energy and underpin the applications discussed later in this dissertation. This section generally describes processes that occur in a molecule, but most are applicable or analogous to processes that occur in semiconductors as well. Either way, the light absorbing material of interest will be called a chromophore. Scheme 1.1 depicts a Jablonski diagram, which demonstrates the fundamental photophysical processes that can occur in a molecular system following light excitation.[1] Absorption of light results in excitation of an electron to a higher energy state. The first process likely to occur after any excitation is internal conversion (IC), in which energy is released as vibrations (heat) as the excited electron rapidly falls to lower excited states. Following this process, the electron could continue to release energy as heat as it relaxes to the ground electronic state. Alternatively, relaxation can occur via release of a photon in the process of fluorescence. If heavy metal atoms are present, the molecule may also undergo a

process called intersystem crossing (ISC), in which the excited electron changes spin, resulting in a triplet excited state (T_1), which is lower in energy than the singlet excited state (S_1). From this triplet excited state, relaxation can occur either via IC or release of a photon, which is called phosphorescence in this case, differentiated from fluorescence because it typically has a much longer timescale due to the disallowed nature of the transition from triplet excited state to singlet ground state. These processes are all intramolecular, occurring within a single molecule.

1.3.2   *Intermolecular photochemical processes*

Electron transfer (ET) and energy transfer (EnT) are two primary intermolecular processes that account for much of the behavior observed in photochemical systems. Other intermolecular photochemical phenomena, in particular those involving molecular aggregation, will be discussed in Section 1.5 and Chapter 2. ET is the process of transferring an excited state electron from the excited molecule to an empty orbital/state of another molecule.[6] Hole transfer (HT) is an analogous process in which an electron is transferred from another molecule into the partially unoccupied ground state orbital of the excited molecule. A "hole" is a quasiparticle indicating the absence of an electron and is typically more commonly used when discussing semiconductor photophysics. To clarify, in this dissertation the term "electron transfer" is used when referring to transfer of an electron from the excited chromophore to another species, and "hole transfer" when referring to transfer of a hole from the excited chromophore to another species (which is equivalent to an electron transfer from another species to the excited chromophore). The thermodynamics of photoinduced electron transfer are described by the following equation:

$$\Delta G_{ET} = -\mathcal{F}[E_{ox}(D^{\bullet+}/D) - E_{red}(A/A^{\bullet-})] - w - E_{0,0}$$

where $\mathcal{F}$ is Faraday's constant, E_{ox} and E_{red} are the oxidation and reduction potentials of the electron donor and acceptor, respectively, w is an electrostatic work term (typically small in

magnitude and therefore disregarded), and $E_{0,0}$ is the excited state energy of the chromophore. This equation allows one to determine whether ET or HT can occur in a given system; ΔG must be negative for spontaneous ET or HT to occur.

Energy transfer (EnT) is another primary intermolecular photochemical process, in which the excited state energy of the chromophore is transferred to another species, exciting that species to its excited state.[7-8] Two mechanisms are proposed for this process. In Forster resonance energy transfer (FRET), fluorescence of the chromophore is absorbed by the acceptor species, leading to excitation. Therefore, spectral overlap must exist between the fluorescence spectrum of the donor chromophore and the absorption spectrum of the acceptor. The other mechanism is Dexter energy transfer, which occurs only at short distances and requires wavefunction overlap, as energy transfer is completed via a superexchange mechanism. Spectral overlap is not necessarily required and thus "dark" states of acceptor molecules (states that do not absorb light, often triplet states) can be accessed.

1.3.3 Photocatalysis

Photocatalysis is a subset of photochemistry in which a chromophore, via either ET, HT, or EnT, drives some chemical reactivity and is regenerated either by completion of a reaction cycle or by the presence of sacrificial electron or hole quenchers. Scheme 1.2 shows a generalized version of this process. The photocatalyst is excited by light, then transfers an electron to an acceptor A, which could be either a substrate or a sacrificial electron acceptor. A$^{\bullet-}$ can then proceed to undergo open shell reactivity with other reagents or with the hole quencher (electron
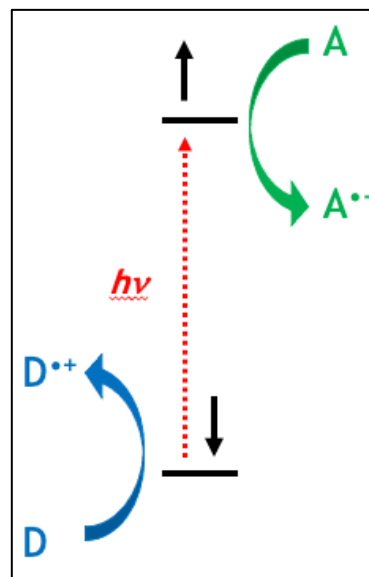
Scheme 1.2. Schematic depicting ET (green) to electron acceptor (A) and HT (blue) to hole acceptor (or electron donor, D) from an excited photocatalyst.

donor) D, which is oxidized by HT to form $D^{\bullet+}$. Photoinduced ET or HT to A or D occur only if ΔG (as determined by the free energy equation given in the previous section) is negative. For EnT, sacrificial reagents are not required, as no ET or HT takes place; energy is simply transferred from chromophore to the substrate, after which the chromophore returns to its initial state. Photocatalysis has been explored for a very wide variety of organic reactions using various types of chromophores (see Section 1.3.4).[6, 9-10] There are numerous potential advantages to developing photocatalytic methods for reactions. Most photocatalytic reaction take place at room temperature and use reagents that are less toxic than equivalent chemical transformations. Light is a readily available and renewable energy source. As will be discussed further in Section 1.4, photocatalysis drives the photosynthetic generation of fuels from sunlight.[11]

1.3.4   Types of chromophores

Chromophores, light absorbing molecules or materials that can undergo the processes reviewed above, can mostly be divided into three main categories: i) transition-metal complexes, ii) organic dyes, and iii) semiconductors (including those in nanomaterial form). Transition-metal complexes often contain noble metals such as ruthenium or iridium. Though these metals are prohibitively rare and expensive and thus unlikely to be used at scale, they play an important role in the photochemistry of their complexes.[9] When excited, these complexes typically undergo a metal-to-ligand charge transfer (MLCT), which results in an intramolecular charge separation in which the excited electron has moved from the metal center to the ligand. In addition, due to strong spin-orbit coupling, which occurs due to the presence of the heavy noble metal atom, ISC can occur to a triplet MLCT state, which is very long-lived, on the order of microseconds. These two phenomena result in high probability of ET or HT to an acceptor.

Organic dyes are considerably cheaper than rare-earth transition metal complexes and can also strongly absorb visible light.[6] However, most (but not all) cannot easily access triplet excited states and are therefore limited to singlet excited states that typically decay on the nanosecond time scale, leading to less efficient ET and/or HT. The manipulation of the photophysical properties of organic dyes by self-assembly into supramolecular structures is a potential strategy to mitigate this disadvantage and will be discussed shortly.

The third category, generally termed semiconductor materials, may contain any semiconductor that can absorb a significant amount of light, which ultimately depends on the band structure and thus the intrinsic structure and composition of the material. In this work, the semiconductors of interest are nanocrystals called quantum dots (QDs).[12] QDs are quasi-spherical nanocrystals which, because their sizes are smaller than their excitonic Bohr radii, exhibit quantum confinement effects. As a result, their band gaps, and therefore excited state energies, can be easily tuned simply by changing the nanocrystal size, providing considerable flexibility when considering QDs for use in applications involving ET and/or HT or EnT processes. In addition, due to their nanocrystalline nature QDs possess huge surface area to volume ratios and have surface capping organic species called ligands. These ligands can dictate the rate at which acceptors reach the QD surface and therefore control the rate of ET and/or HT.[13-14] The ligands can also exchange with acceptors if the acceptor has a suitable binding group, such as a carboxylate or phosphonate. These features differentiate QDs from molecular dyes and complexes and impart potential for greater control over photocatalytic processes.[15-16] Efforts have also been made to construct supramolecular assemblies of QDs and will be discussed in Section 1.5.2.

1.4.   Solar Fuels

The term "solar fuels" refers to a fuel that can be artificially produced *via* sunlight and has a carbon-neutral life cycle.[17] It is important to note that "fuels" can ideally be stored indefinitely and at a high energy ratio. This is the key difference between solar fuels and solar electricity, i.e. solar photovoltaics, which produce an electrical current that must be used instantly or stored in a battery, which generally have much lower gravimetric storage densities than liquid fuels. Production of solar fuels in principle is accomplished by mimicking plants in "artificial photosynthesis".[11] This process is essentially a series of redox reactions in which water is oxidized to oxygen and either protons are reduced to hydrogen gas or carbon dioxide is reduced to a carbonaceous fuel. Light absorption by chromophores drives ET and HT in these redox processes. Thus, light energy is transformed into chemical energy. Due to the numerous challenges of integrating reductive and oxidative chemistry into a single device, researchers have primarily focused on either the reductive or oxidative side of the overall reaction in isolation, using sacrificial reagents to complete the redox cycle.

1.4.1   Carbon dioxide reduction

Carbon dioxide (CO_2) is one of the main "greenhouse gases" driving the increase in global average temperatures. It is the most oxidized form of carbon, produced when a fuel has been fully oxidized (burned). Reducing CO_2 results in compounds that can be burned to release the energy expended in the reductive process. Therefore, the reduction of CO_2 driven by sunlight could produce a "carbon-neutral" cycle in which no net CO_2 is released into the atmosphere, and the ultimate source of energy is sunlight (the "fossil fuels" currently used are technically a form of this cycle, but with the timescale of consumption rapidly outpacing that of production). CO_2 reduction is considered by some to be a better long-term target for solar fuels than proton reduction

to hydrogen gas, as CO_2 could potentially be reduced to methanol, which as a liquid would be much easier to store than hydrogen.

However, CO_2 reduction is an inherently challenging process. The formal one-electron reduction potential is approximately -2.0 V vs. SCE, primarily due to an unfavorably change in geometry from planar to bent upon reduction to the radical anion.[18] Multielectron reduction coupled to proton transfer results in much more favorable reduction potentials; for example, the two-electron, two-proton reduction of CO_2 to CO is -0.70 V vs. SCE, and the six-electron, six-proton reduction of CO_2 to methanol is -0.38 V vs SCE.[18] Unfortunately, the need for multiple electron and proton transfers results in significant kinetic limitations that make the overall process quite challenging in practice. Heterogeneous[19] and homogeneous[20] catalysts have been developed to lower the energy barriers for these processes.

1.4.2   Photosensitization of catalysts

As many CO_2 reduction catalysts typically do not absorb significant amounts of visible light, chromophores can be used to "photosensitize" catalysts via ET (in tandem with a sacrificial hole quencher to regenerate the chromophore).[11, 20] As mentioned in Section 1.3.2, successful ET requires $\Delta G_{ET} < 0$. Due to the aforementioned high reduction potential of CO_2, catalysts for CO_2 reduction typically have high reduction potentials. Even if the mechanism of reduction involves thermodynamically less challenging proton-coupled electron transfer, high overpotentials are typically required, likely due to the difficulty of initial electron transfer to CO_2 or instability of intermediates.[18, 21] The high reduction potentials of these catalysts limit the choice of chromophores to those capable of transferring elections to these species. This will be further discussed in specific contexts in Chapters 2 and 3.

1.5.   Supramolecular chemistry

Supramolecular chemistry is most simply and broadly defined as "chemistry beyond the molecule".[22] It involves the design of molecules and/or experimental conditions such that "self-assembly" can occur, that is, molecules will spontaneously order themselves to create "supramolecular" structures. This can be accomplished via a variety of motifs, including but not limited to hydrogen bonding, solvophobic effects, and electrostatic attraction.[23] The assembly of molecules into larger ordered structures can often result in emergent properties that do not exist in the monomeric ensemble.[24] Self-assembled systems have been also been designed using nanoparticles.[25] The use of organic dyes and QDs in self-assembled systems are briefly discussed below.

1.5.1   Self-assembly of organic aromatic dye molecules

The self-assembly of organic aromatic dye molecules has generally been accomplished by taking advantage of $\pi-\pi$ stacking between aromatic molecules in addition to controlling the solubility of these molecules by judicious choice of hydrophobic or hydrophilic tail moieties.[23, 26] The self-assembly of perylene-based molecules, particularly perylene diimides (PDI, also referred to as perylene bisimides, PBI), have been thoroughly explored in both organic and aqueous solution.[27] Aggregation of PDI molecules leads to strong electronic coupling within supramolecular stacks, which has been exploited for a number of applications, as further discussed in Chapter 2.

1.5.2   Self-assembly of QDs

Numerous schemes have been developed to controllably form supramolecular assemblies of QDs.[25] Ditopic ligands are often used, particularly when growing films, to covalently link QDs together. Electrostatic approaches have also been used to attract QDs of different charges to each

other.[28] Adding a bridging metal ion such as Zn^{2+} can assemble QDs capped with carboxylate ligands.[29] Self-assembly of QDs of different size can result in efficient energy transfer (EnT) to specific sites, an important design principle in solar energy conversion systems.[30]

The self-assembly of QDs with specific molecules, particularly catalysts, is another goal of supramolecular QD systems. QDs have been linked to homogeneous carbon dioxide reduction catalysts by electrostatic assembly.[31-33] Our efforts towards characterizing a QD-catalyst assembly will discussed in Chapter 3.

1.6.   Dissertation Outline

This dissertation explores the use of organic and semiconductor photosensitizers in photocatalytic CO_2 reduction and EnT-sensitized reactions, focusing on the potential advantages conveyed by self-assembly as well as catalyst and substrate interactions with QD surfaces. Chapter 2 describes the synthesis and self-assembly of novel chromophores and their use as photosensitizers of an iron porphyrin CO_2 reduction catalyst. Chapter 3 discusses efforts towards the characterization of a possible binding interaction between the surface of $CuInS_2$@ZnS QDs and an iron porphyrin CO_2 reduction catalyst. In Chapter 4, efforts towards the development of an EnT-sensitized aza Paterno-Buchi reaction between olefins and imines enabled by substrate binding to QD surfaces are presented. Finally, concluding remarks and some future directions are given in Chapter 5.

Chapter 2 : Self-Assembly of *N*-annulated Perylene Chromophore Amphiphiles for Aqueous Photocatalytic CO₂ Reduction

2.1. Chapter Summary

This chapter describes the synthesis of novel *N*-annulated perylene chromophore amphiphiles, their self-assembly in aqueous solution, and their usage in photosensitizing an iron porphyrin CO_2 reduction catalyst. First, the previous development of perylene monoimide (PMI) chromophore amphiphiles for use as photosensitizers of proton reduction catalysts is discussed, highlighting the advantages provided by self-assembly in that system. The challenges of CO_2 reduction relative to proton reduction (discussed in section 1.4.2) are briefly reiterated to demonstrate motivation for a new class of perylene chromophore amphiphiles based on the *N*-annulated perylene core. The synthesis of these molecules is reported, followed by characterization of their self-assembly in aqueous solution and photosensitization of an iron porphyrin catalyst. This work shows that amphiphilic *N*-annulated perylene derivatives can self-assemble in aqueous solution, but that differences in the structure of the aromatic core significantly change the stacking arrangement of the perylenes, which affects the strength of intermolecular electronic coupling and may decrease their effectiveness as photosensitizers in photocatalytic schemes, though further work is required to make definitive conclusions.

2.2. Introduction

As discussed in section 1.5, self-assembly is one strategy that has been pursued to mitigate the fast charge recombination of organic dyes by promoting exciton diffusion through aggregated dye stacks. Previously, Stupp *et al.* synthesized amphiphilic PMI chromophores, which formed long nanoribbons with crystalline domains when dissolved in aqueous solution.[34] These PMI assemblies were found to exhibit strong electronic coupling, likely in part due to their highly ordered nature, and were efficient photosensitizers of a homogeneous nickel proton reduction catalyst. Further work found that modification of the length of the water-solubilizing alkylcarboxylate tail had a

strong effect on the extent of electronic coupling and morphology of the nanostructures formed and established a positive correlation between strong electronic coupling and effectiveness in photosensitization of the nickel proton reduction catalyst.[35] The PMI aromatic core could also be modified with various alkylamine tails at the 9-position, resulting in further variation in electronic coupling and morphology.[36] Theoretical work established that strong electronic coupling between PMI monomers was the result of mixing between bright localized Frenkel excitons and dark charge transfer excitons, and that the high dielectric environment (aqueous solution) enabled enhanced exciton diffusion and charge separation within the PMI stacks.[37]

While these PMI assemblies efficiently photosensitize proton reduction catalysts, they do not have enough driving force to photosensitize CO_2 reduction catalysts, which as discussed in Section 1.4.1 can only be photosensitized by chromophores with high reduction potentials. Unfunctionalized perylene is significantly more reducing than PMI, which has a lower reduction potential due to the electron-withdrawing monoimide functional group. *N*-annulation of the perylene core at the bay position results in a visible-light absorbing aromatic core that still retains a relatively high LUMO capable of reducing the iron porphyrin CO_2 reduction catalyst 5,10,15,20-tetra(4′-*N,N,N*-trimethylanilinium) porphyrin pentachloride (**FeTMA**).[38] It was hypothesized that the advantageous features of amphiphilic PMI assemblies could be reproduced using the *N*-annulated perylene core, which is easily be functionalized by S$_N$2 alkylation.[39] A series of these molecules was synthesized, and their self-assembly in aqueous solution and photosensitization of **FeTMA** was studied.

2.3.   Results and Discussion

2.3.1   Synthesis of N-annulated perylene amphiphiles
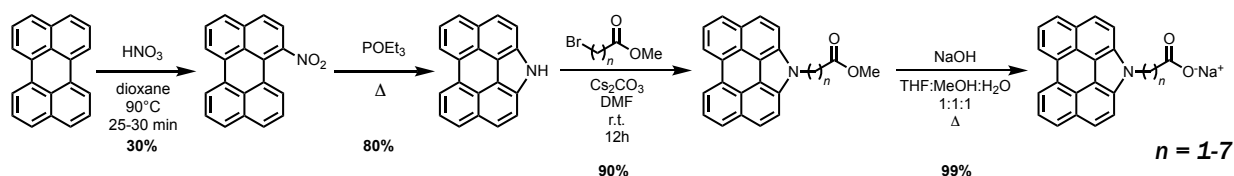
Figure 2.1. Synthesis of *N*-annulated perylene amphiphiles.

The *N*-annulated perylene core was synthesized via existing literature procedures (Figure 2.1, first two steps).[38, 40] Unfunctionalized perylene was treated with concentrated nitric acid in hot dioxane, leading to a mixture of 1- and 3-nitroperylene isomers, which could be separated by column chromatography. Pure 1-nitroperylene was refluxed in neat triethylphosphite, leading to a reductive cyclization via the Cadogan reaction. The *N*-annulated product conveniently crystallized from solution when cooled to room temperature. Nucleophilic addition of esterified carboxyalkyl tails containing 1 to 7 methylene units were easily added in the presence of cesium carbonate in *N,N*-dimethylformamide solution.[39] After column purification, the methyl ester was cleaved with sodium hydroxide to yield a water-soluble *N*-annulated perylene amphiphile, which will be referred to as **Ln**, where **n** is the number of methylene groups between the core and the carboxylate group.

2.3.2   Self-assembly of N-annulated perylene amphiphiles

N-annulated perylene amphiphiles were dissolved in aqueous solution by suspending the free carboxylic acid in water and adding 1-2 equivalents of sodium hydroxide to deprotonate the acid. The UV-vis spectra of compounds **L1-L7** dissolved in aqueous solution, as well as a representative

spectrum of these compounds in organic solution (DMSO), are shown in Figure 2.2. Generally, a slight shift in peak wavelength and/or a change in relative intensity of vibronic bands was observed. These spectral features are consistent with aggregation,[27] which is expected for amphiphilic aromatic molecules dissolved in aqueous solution.[23] Unlike PMI
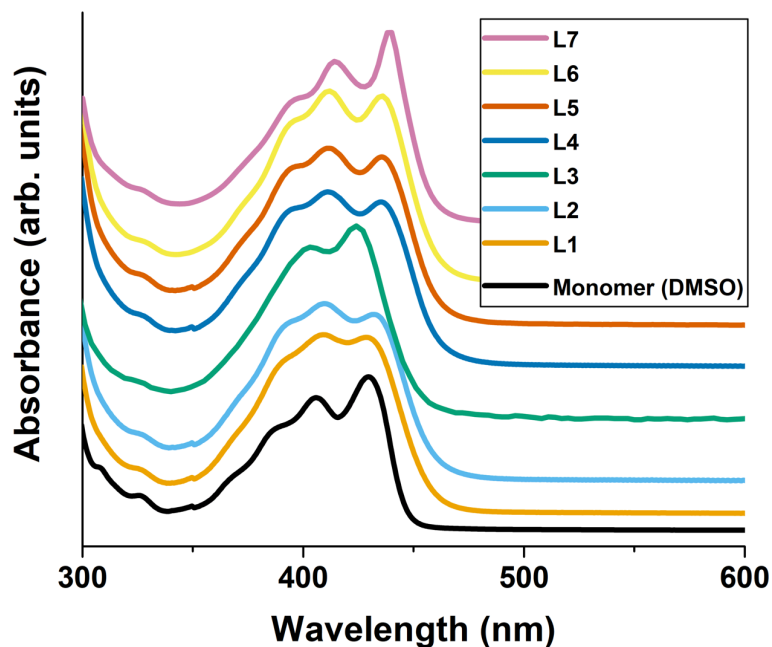
Figure 2.2. UV-vis spectra of "monomer" (black, **L5** dissolved in organic solvent, DMSO), and *N*-annulated perylene amphiphiles **L1-L7** dissolved in basic aqueous solution.

amphiphile assemblies, both the wavelength shift and changes in peak intensity are relatively small, suggesting only weak electronic coupling between *N*-annulated perylene units.
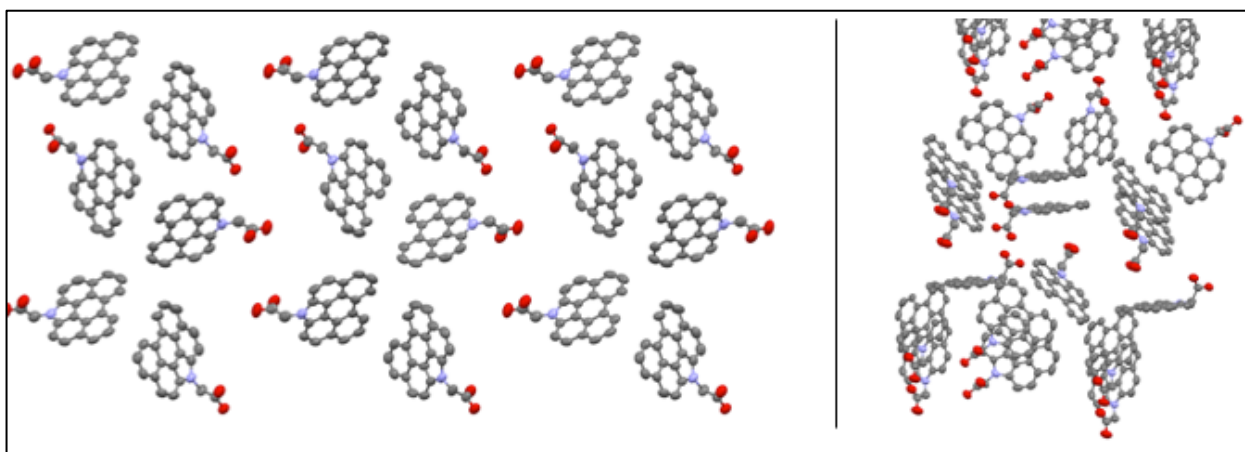
Figure 2.3. Two views of crystal structure of **L1**, grown from slow evaporation of DMSO.

Further insight into the reason for weak electronic coupling was found in the crystal structure of the free acid of **L1**, grown by slow evaporation of DMSO. While not an exact comparison, the crystal structure suggests a preferred packing arrangement for the aromatic *N*-annulated perylene core. As shown in Figure 2.3, the *N*-annulated perylene core appears to prefer packing in a
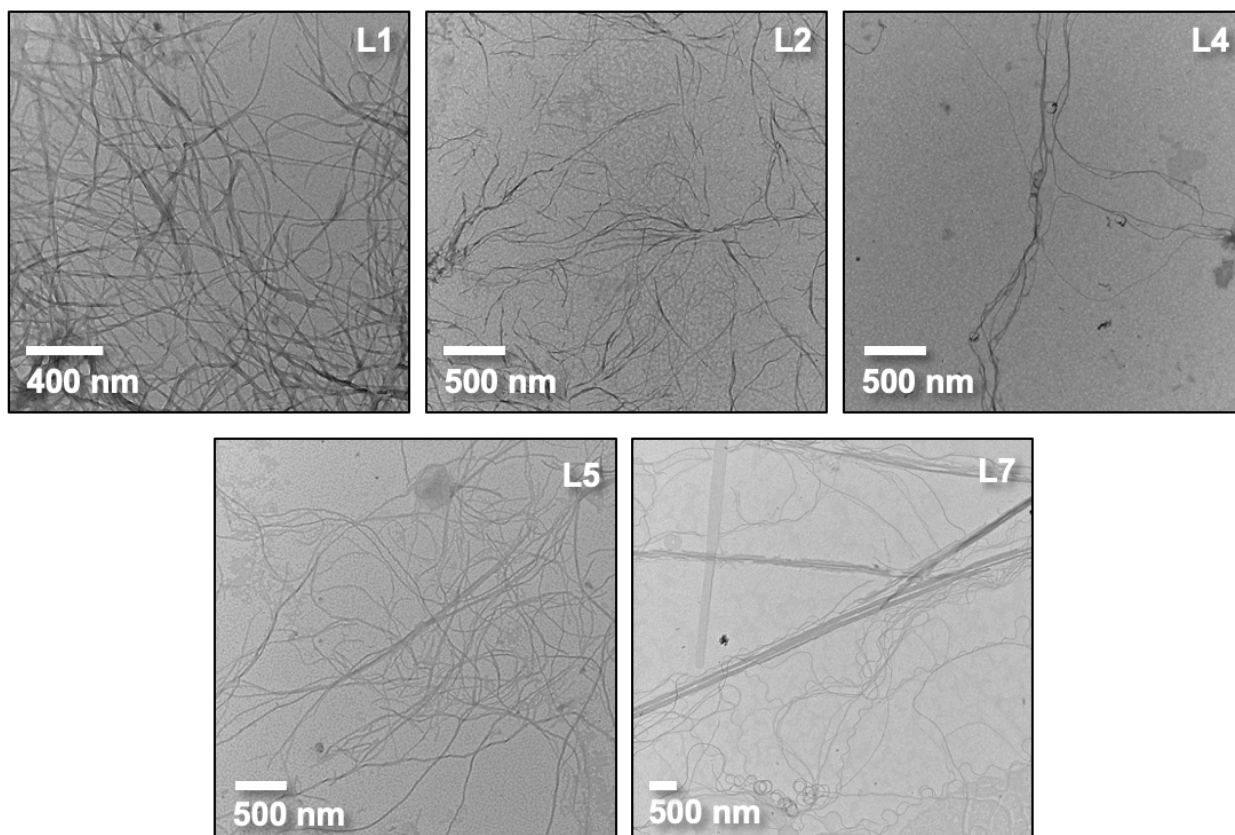
Figure 2.4. TEM images of (clockwise from top left) L1, L2, L4, L7, and L5, aqueous solutions deposited directly on TEM grids.

herringbone shape. This packing arrangement has been observed in the crystal structure of perylene and similar molecules and is related to a favorable side to face interaction between aromatic units.[41] Some face to face $\pi-\pi$ stacking can be observed but does not appear to repeat over more than two molecules. Overall, the tendency towards herringbone-like stacking is likely the dominant motif and is probably responsible for weak electronic coupling between the aromatic molecules.

The self-assembled nanostructures formed by dissolution of **L1, L2, L4, L5,** and **L7** in aqueous solution were observed by transmission electron microscopy (TEM). In general, long ribbon-like structures were formed as shown in Figure 2.4. **L3** and **L5** were also observed by cryogenic TEM, shown in Figure 2.6, which avoids drying effects that could lead to the false appearance of
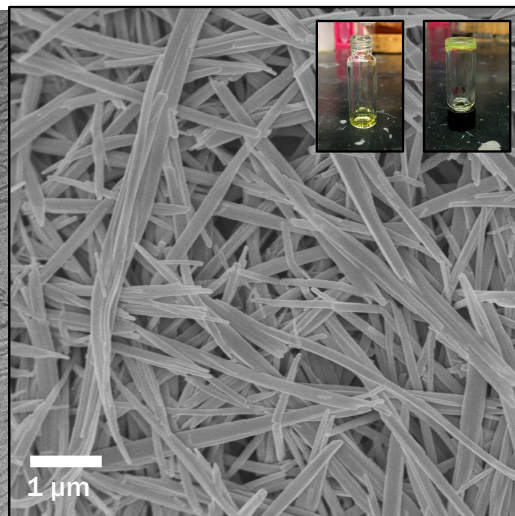
Figure 2.5. SEM image of hydrogel formed by addition of 300 mM CaCl$_2$ to 5 mM **L5** aqueous solution; photographs of solution before and after CaCl$_2$ addition (top right inset)

nanostructures. These data confirm that *N*-annulated perylene amphiphiles assemble into extended ribbon-like nanostructures in aqueous solution.

The extended nanostructures formed by **L5** were able to form hydrogels by addition of a positively charged crosslinking agent such as Ca^{2+}. Images of a solution of **L5** before and after CaCl$_2$ addition are shown in the inset of Figure 2.5. The microstructure of these gels was investigated by scanning electron microscopy (SEM). As shown in Figure 2.5, **L5** appears to form a network of bundled fibrous structures when exposed to CaCl$_2$. The divalent Ca^{2+} likely results
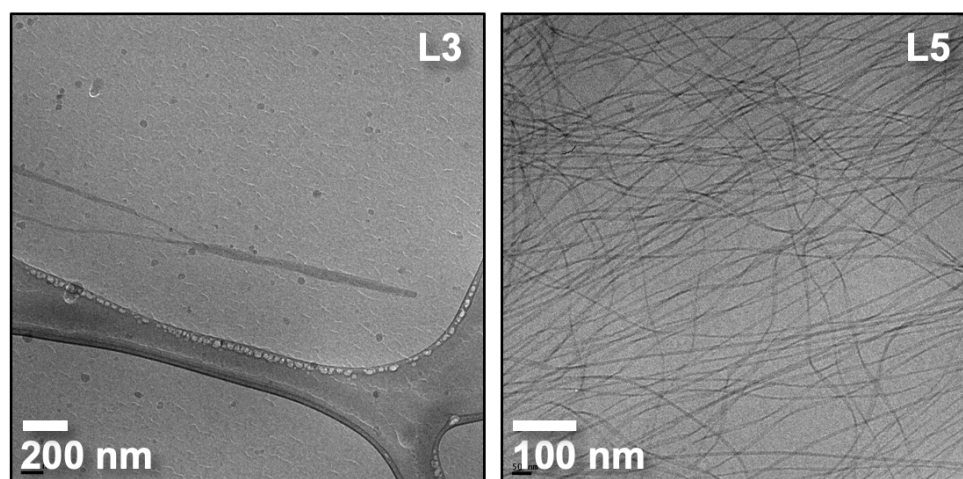
Figure 2.6. Cryogenic TEM images of L3 and L5 in aqueous solution.

in aggregation of the ribbons formed by **L5** in aqueous solution (as observed by TEM in Figure 2.4 and 2.6), as well as linking these bundles together to create a gel network. The network appears to be easily broken, which is unsurprising given that the fibers are composed of supramolecular polymers, held together only by noncovalent forces. **L1-L4** and **L6-L7** also showed promise for gelation through visual inspection after Ca^{2+} addition but were not further explored.

2.3.3   *Photosensitization of CO$_2$ reduction catalyst*

The self-assembled nanostructures formed by **L5** were u sed to photosensitize an iron porphyrin CO_2 reduction catalyst, **FeTMA**, in aqueous solution. This catalyst has previously been shown to be highly efficient and selective for electrochemical reduction of CO_2 to CO over proton reduction[42] and has also been photosensitized to perform photocatalytic CO_2 reduction in nonaqueous solution.[43-44] As discussed in Section 2.2, *N*-annulated perylene has a sufficiently high reduction potential for photoinduced electron transfer to **FeTMA** to occur. **FeTMA** was synthesized by iron metalation of the commercially available free base H_2TMA porphyrin using existing procedures.[42] Photoluminescence quenching, shown in Figure
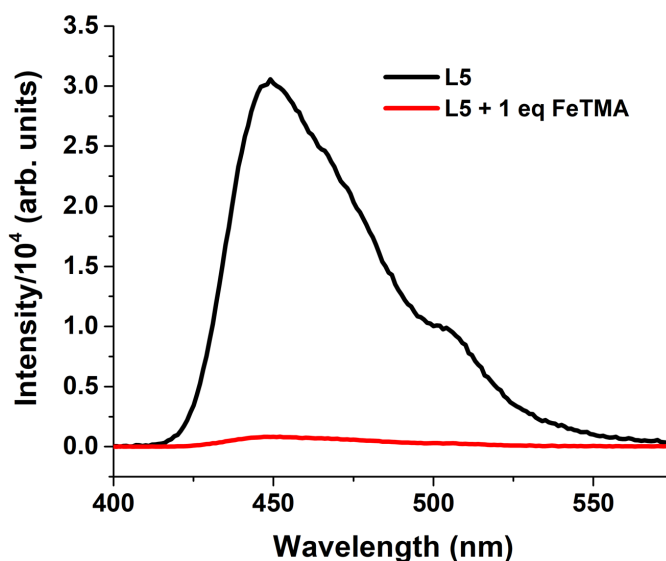
Figure 2.7. Photoluminescence spectra of **L5** without **FeTMA** (black) and with 1 equiv **FeTMA** (red) in aqueous solution.
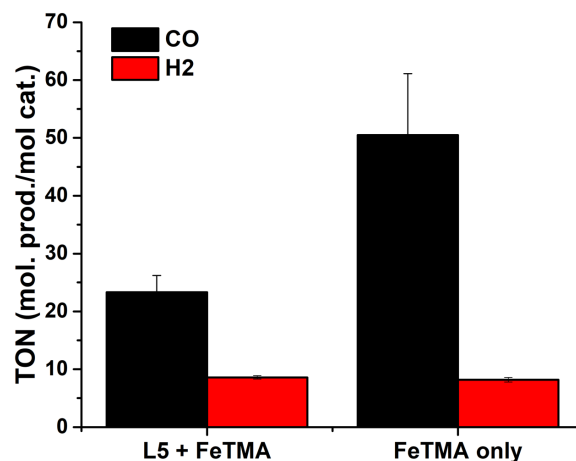
Figure 2.8. Photocatalytic CO and H$_2$ production by **L5 + FeTMA** or **FeTMA** only, both with 50 mM sodium ascorbate and 100 mM NaHCO$_3$ in a 1-mL CO$_2$-degassed aqueous solution, illuminated with a white light for 2 days.

2.7, reveals that **FeTMA** quenches the luminescence of **L5**, suggesting that electron transfer from **L5** to **FeTMA** is occuring. However, due to spectral overlap between the luminescence of **L5** and the absorbance of **FeTMA**, energy transfer could also be responsible for some or all the observed quenching.

Photocatalysis experiments were performed in aqueous solution, with product formation (CO and H_2) measured by gas chromatography (GC). All samples contained 1 mM of **L5** chromophore, 5 μM **FeTMA**, and 50 mM sodium ascorbate. Some variations were made in an attempt to optimize the system. In aqueous solution, dissolved CO_2 reacts with water to form carbonic acid, H_2CO_3, which lowers the pH of the solution to ca. 4.2 when the solution is saturated by degassing at atmospheric pressure.

Figure 2.9. Photocatalytic CO and H_2 production by **L5** + **FeTMA** or **FeTMA** only, both with 50 mM sodium ascorbate in a 1-mL CO_2-degassed aqueous solution, which were adjusted to pH ca. 9.5 after CO_2 degassing by NaOH addition, illuminated with a white light for 2 days.

Solutions of **L5** with sodium ascorbate and **FeTMA** appeared to precipitate after CO_2 degassing, likely due to protonation of the carboxylate group of **L5**. To buffer the solution against significant pH decreases, 100 mM $NaHCO_3$ was added to the catalytic solutions, resulting in a final pH of ca. 6.7 and less **L5** precipitation. These samples were illuminated for 2 days with a white light, resulting in ca. 30 TON, where TON (turnover number) = mol CO/mol catalyst, as shown in Figure 2.8. However, as shown in the same figure, samples containing **L5** actually performed worse than a control sample containing only **FeTMA** and sodium ascorbate. **FeTMA** has visible absorption that overlaps with the white light lamp emission, as can be seen by comparison of Figures 2.10 and 2.11 (see Section 2.5), so it is capable of

photosensitizing itself, as has been reported in the literature.[45] The lower TON observed in samples containing **L5** could be due to unproductive absorbance by **L5** (that does not result in electron transfer to **FeTMA**) and/or from light scattering by **L5** precipitates, which may still be present despite the use of the $NaHCO_3$ buffer. Another approach used to combat the pH issue was to prepare samples of **L5**, **FeTMA**, and sodium ascorbate, degas with CO_2, leading to **L5** precipitation, and then add NaOH to bring the solution pH to ca. 9.5, which re-dissolved **L5**. Illuminating these samples with a white light resulted in 24 TON, which was higher than the control sample without **L5**, which produced 11 TON, as shown in Figure 2.9. In this case, **L5** was well dissolved and therefore more likely to be able to effectively photosensitize **FeTMA**. The TON for the **FeTMA** only control is likely lower at higher pH because the proposed mechanism for CO_2 reduction by this catalyst involves two protons.[44]

Further work is needed to fully understand and optimize this photocatalytic system. A few areas of further study are given here. The pH dependence of **Ln** solubility and self-assembly must be understood in order to make sure that **Ln** is actually solubilized and able to interact with **FeTMA** in solution. The potential for energy transfer from **Ln** to **FeTMA** should also be considered in more depth and possibly requires redesign of the chromophore or use of a different catalyst that does not absorb in the region of **Ln** emission. Finally, a different light source should be used. From comparison of Figure 2.3, which shows **Ln** absorption, and Figure 2.12, which shows the emission spectrum of the white light used in all photocatalysis experiments, it can clearly be seen that there is little spectral overlap. The use of a blue LED would provide the system with significantly more usable light and would almost definitely increase performance.

2.4. Conclusions

Novel *N*-annulated perylene chromophore amphiphiles were synthesized in good yield. These molecules self-assembled in aqueous solution to form long ribbon-like nanostructures, which could form weak gels in the presence of Ca^{2+}. Unlike PMI chromophore amphiphiles, *N*-annulated perylene amphiphiles do not appear to exhibit strong electronic coupling, as exhibited by only minor changes in their UV-vis spectra. Crystal structures of **L1** as well as literature structures suggest that strong edge-to-face interactions are favorable in perylene stacking, which may disrupt strong coupling. The lack of strong electronic coupling may be responsible for the poor performance of these molecules as photosensitizers of the CO_2 reduction catalyst **FeTMA**, but a number of mitigating variables, given in the previous section, make it difficult to provide definitive conclusions regarding photocatalytic performance.

2.5. Experimental Details

2.5.1 Synthesis of compounds

Synthetic characterization

^{1}H NMR spectra were acquired in dimethylsulfoxide-*d$_6$* using a Varian Inova 500 (500 MHz) or a Bruker AVANCE III HD (400 MHz). ^{13}C NMR spectra were acquired using a Bruker AVANCE III (500 MHz, direct cryoprobe). High resolution mass spectrometry was acquired using an Agilent 6210 LC-TOF (ESI).

UV-vis absorption spectroscopy

Spectra were acquired in DMSO or H_2O using a Shimadzu UV-1800 UV Spectrophotometer using a 0.05 mm quartz plate cuvette.

1-nitroperylene

This procedure involves addition of concentrated nitric acid to a hot solution at a relatively large scale and was therefore cautiously performed behind a blast shield. A slightly modified literature procedure was used.[38, 40] 5 g of perylene was suspended in 200 mL of 1,4-dioxane, and the mixture was sonicated and heated to 100 °C until most of the perylene dissolved. A mixture of 4 mL H_2O and 2.5 mL fuming nitric acid was added dropwise to the hot solution. The solution was stirred at 100 °C for 20-30 minutes or until very dark red. The solution was then cooled to room temperature and poured into approximately 3 L of cold water and either collected by vacuum filtration or extracted with dichloromethane (DCM). The crude mixture was purified by column chromatography on silica (25% dichloromethane in hexanes) to afford 1-nitroperylene in ~30% yield. ^{1}H NMR (500 MHz, DMSO-d_6) δ 8.51 (dd, J = 17.6, 7.5 Hz, 2H), 8.02 – 7.92 (m, 4H), 7.80 (dd, J = 8.8, 1.6 Hz, 1H), 7.77 – 7.70 (m, 2H), 7.66 (td, J = 7.8, 1.6 Hz, 1H), 7.56 (td, J = 7.9, 1.6 Hz, 1H).

N-annulated perylene

A modified literature procedure was followed.[38] 1-nitroperylene was dissolved in 5-10 mL of neat triethylphosphite (POEt$_3$) and refluxed at 175 °C overnight. The solution was cooled to room temperature and the resulting orange-yellow crystalline precipitate was collected on filter paper and washed with cold petroleum ether. The product was used in subsequent synthetic steps without further purification. ^{1}H NMR (400 MHz, DMSO-d_6) δ 12.15 (s, 1H), 8.71 (dd, J = 7.6, 0.6 Hz, 2H), 8.14 (d, J = 8.0 Hz, 2H), 7.96 – 7.89 (m, 4H), 7.81 – 7.76 (m, 2H).

General procedure for esterification of bromoalkylcarboxylic acids

Bromoalkylcarboxylic acid (1 g, 1 equiv) was dissolved in 10 mL of methanol and cooled to 0 °C in an ice bath, then 2-3 equiv SOCl$_2$ were slowly added dropwise. The solution was allowed to warm to room temperature and was stirred overnight. The solvent was removed by rotary

evaporation, and the residue was dissolved in ethyl acetate and washed with sat. $NaHCO_3$ and sat. NaCl. The organic layer was dried over Na_2SO_4, then the solvent was removed by rotary evaporation to afford an oil or liquid product, which was typically used without further purification.

General procedure for attachment of bromoalkanoate methyl esters to N-annulated perylene

N-annulated perylene (250 mg, 0.94 mmol, 1 equiv) was dissolved in *N,N*-dimethylformamide (DMF). Three equivalents of cesium carbonate (Cs_2CO_3) were added, and a slight darkening of the solution was observed. The appropriate bromoalkanoate methyl ester (2 equiv) was separately dissolved in approximately 5 mL of DMF and slowly added to the perylene solution. The solution was stirred in the dark at room temperature overnight, then poured into approximately 300 mL of 1 M HCl, typically affording a yellow precipitate that was collected by vacuum filtration. Longer tail length compounds gave oils, which were more easily obtained by extraction of the DMF/HCl mixture with ethyl acetate or dichloromethane. The product was purified by column chromatography on silica (typically ~1:1 dichloromethane:hexanes) and obtained in >85% yield.

General procedure for cleavage of N-annulated perylene methyl ester

NannPerLnCOOMe was dissolved in 1:1:1 THF:MeOH:[4 M NaOH in H_2O] at ~2.5 mg/mL and stirred at room temperature for approximately 4 h. THF and MeOH were removed by rotary evaporation, then the solution was acidified with 1 M HCl, affording a yellow precipitate that was collected by vacuum filtration, washed with warm H_2O and dried under vacuum.

NannPerL1COOMe

^{1}H NMR (500 MHz, CDCl$_3$) δ 8.63 (d, *J* = 7.5 Hz, 2H), 8.11 (d, *J* = 8.0 Hz, 2H), 7.92 (d, *J* = 8.8 Hz, 2H), 7.81 (t, *J* = 7.8 Hz, 2H), 7.74 (d, *J* = 8.7 Hz, 2H), 5.41 (s, 2H). ^{13}C NMR (125 MHz,

CDCl$_3$) δ 169.1, 132.2, 130.5, 129.1, 125.2, 124.9, 124.8, 124.1, 120.9, 117.9, 112.7, 52.7, 47.0.

HR-MS (ESI) m/z [M+H]$^+$: 338.1178 (calc. for C$_{23}$H$_{16}$NO$_2^+$: 338.1176).

NannPerL2COOMe

^{1}H NMR (400 MHz, CDCl$_3$) δ 8.61 (d, *J* = 7.5 Hz, 2H), 8.09 (d, *J* = 8.0 Hz, 2H), 7.90 (d, *J* = 8.8 Hz, 2H), 7.83 – 7.75 (m, 4H), 5.01 (t, *J* = 6.8 Hz, 2H), 3.58 (s, 3H), 3.06 (t, *J* = 6.8 Hz, 2H). ^{13}C NMR (125 MHz, CDCl$_3$) δ 171.6, 131.6, 130.4, 128.9, 125.1, 124.8, 124.7, 123.8, 120.7, 117.7, 113.2, 52.0, 41.4, 35.6. HR-MS (ESI) m/z [M+H]$^+$: 352.1337 (calc. for C$_{24}$H$_{18}$NO$_2^+$: 352.1332).

NannPerL3COOMe

^{1}H NMR (400 MHz, CDCl$_3$) δ 8.63 (d, *J* = 7.5 Hz, 2H), 8.10 (d, *J* = 8.0 Hz, 2H), 7.90 (d, *J* = 8.7 Hz, 2H), 7.82 – 7.75 (m, 4H), 4.79 (t, *J* = 6.7 Hz, 2H), 3.62 (d, *J* = 0.5 Hz, 3H), 2.47 – 2.37 (m, 2H), 2.34 – 2.28 (m, 2H). ^{13}C NMR (125 MHz, CDCl$_3$) δ 173.2, 131.8, 130.4, 128.8, 125.0, 124.8, 124.6, 123.8, 120.8, 117.5, 113.1, 51.7, 44.6, 30.8, 26.2. HR-MS (ESI) m/z [M+H]$^+$: 366.1494 (calc. for C$_{25}$H$_{20}$NO$_2^+$: 366.1489).

NannPerL4COOMe

^{1}H NMR (400 MHz, CDCl$_3$) δ 8.63 (d, *J* = 7.5 Hz, 2H), 8.10 (d, *J* = 8.0 Hz, 2H), 7.90 (d, *J* = 8.8 Hz, 2H), 7.79 (dd, *J* = 8.2, 7.3 Hz, 4H), 4.72 (t, *J* = 6.9 Hz, 2H), 3.59 (s, 3H), 2.31 (t, *J* = 7.3 Hz, 2H), 2.19 – 2.09 (m, 2H), 1.76 – 1.65 (m, 2H). ^{13}C NMR (125 MHz, CDCl$_3$) δ 173.5, 131.8, 130.4, 128.8, 125.0, 124.8, 124.6, 123.7, 120.7, 117.5, 113.2, 51.6, 45.5, 33.5, 30.6, 22.5. HR-MS (ESI) m/z [M+H]$^+$: 380.1646 (calc. for C$_{26}$H$_{22}$NO$_2^+$: 380.1645)

NannPerL5COOMe

^{1}H NMR (500 MHz, CDCl$_3$) δ 8.68 (dd, *J* = 7.9, 2.4 Hz, 2H), 8.18 – 8.12 (m, 2H), 7.95 (dd, *J* = 8.8, 2.4 Hz, 2H), 7.83 (td, *J* = 8.0, 2.2 Hz, 4H), 4.81 – 4.70 (m, 2H), 3.63 (d, *J* = 2.9 Hz, 3H), 2.28 (t, *J* = 7.8 Hz, 2H), 2.20 – 2.11 (m, 2H), 1.71 (p, *J* = 7.7 Hz, 2H), 1.44 (dp, *J* = 13.6, 7.8 Hz, 2H).

^{13}C NMR (125 MHz, CDCl$_3$) δ 173.9, 131.8, 130.4, 128.8, 125.0, 124.9, 124.5, 123.7, 120.7, 117.5, 113.3, 51.5, 45.6, 33.8, 30.9, 26.6, 24.6. HR-MS (ESI) m/z [M+H]$^+$: 394.1809 (calc. for C$_{27}$H$_{24}$NO$_2{}^+$: 394.1802)

NannPerL6COOMe

^{1}H NMR (400 MHz, CDCl$_3$) δ 8.64 (d, J = 7.5 Hz, 2H), 8.11 (d, J = 8.0 Hz, 2H), 7.91 (d, J = 8.8 Hz, 2H), 7.83 – 7.76 (m, 4H), 4.70 (t, J = 6.9 Hz, 2H), 3.60 (s, 3H), 2.23 (t, J = 7.4 Hz, 2H), 2.16 – 2.04 (m, 2H), 1.56 (dt, J = 11.9, 6.2 Hz, 2H), 1.37 (dq, J = 7.0, 3.5 Hz, 4H). ^{13}C NMR (125 MHz, CDCl$_3$) δ 174.0, 131.9, 130.3, 128.8, 125.0, 124.9, 124.5, 123.7, 120.7, 117.4, 113.3, 53.4, 51.5, 45.7, 33.9, 31.0, 30.9, 28.8, 26.8, 24.7.

NannPerL7COOMe

^{1}H NMR (500 MHz, CDCl$_3$) δ 8.65 (dd, J = 7.6, 1.6 Hz, 2H), 8.13 (dd, J = 8.1, 1.6 Hz, 2H), 7.92 (dd, J = 8.7, 1.6 Hz, 2H), 7.84 – 7.77 (m, 4H), 4.70 (td, J = 7.0, 1.7 Hz, 2H), 3.63 (s, 3H), 2.24 (td, J = 7.5, 1.6 Hz, 2H), 2.10 (m, J = 7.2 Hz, 2H), 1.61 – 1.53 (m, 2H), 1.44 – 1.31 (m, 4H), 1.30 – 1.22 (m, 2H).

NannPerL1COOH (L1)

^{1}H NMR (500 MHz, DMSO-d_6) δ 13.17 (s, 1H), 8.76 (d, J = 7.5 Hz, 2H), 8.18 (d, J = 8.0 Hz, 2H), 8.02 (d, J = 8.8 Hz, 2H), 7.96 (d, J = 8.8 Hz, 2H), 7.82 (t, J = 7.8 Hz, 2H), 5.68 (s, 2H). ^{13}C NMR (125 MHz, DMSO-d_6) δ 171.1, 132.8, 130.1, 128.9, 125.7, 125.3, 124.4, 124.1, 121.5, 117.0, 114.9, 47.0.

NannPerL2COOH (L2)

^{1}H NMR (400 MHz, DMSO-d_6) δ 12.35 (s, 1H), 8.73 (d, J = 7.5 Hz, 2H), 8.16 (d, J = 8.0 Hz, 2H), 8.06 (d, J = 8.8 Hz, 2H), 7.94 (d, J = 8.8 Hz, 2H), 7.80 (t, J = 7.8 Hz, 2H), 5.03 (t, J = 6.6 Hz, 2H), 3.00 (t, J = 6.6 Hz, 2H).

*NannPerL3COOH (**L3**)*

^{1}H NMR (400 MHz, DMSO-d_6) δ 8.74 (d, J = 7.5 Hz, 2H), 8.16 (d, J = 8.0 Hz, 2H), 8.03 (d, J = 8.8 Hz, 2H), 7.95 (d, J = 8.8 Hz, 2H), 7.80 (t, J = 7.8 Hz, 2H), 4.87 – 4.80 (m, 2H), 2.23 (dd, J = 4.7, 3.0 Hz, 4H). ^{13}C NMR (125 MHz, DMSO-d_6) δ 174.4, 132.1, 130.0, 128.8, 125.6, 125.2, 124.5, 124.1, 121.5, 116.8, 114.8, 49.1, 44.8, 26.7.

*NannPerL4COOH (**L4**)*

^{1}H NMR (500 MHz, DMSO-d_6) δ 11.95 (s, 1H), 8.78 (d, J = 7.3 Hz, 2H), 8.20 (d, J = 8.0 Hz, 2H), 8.12 – 8.06 (m, 2H), 8.01 – 7.96 (m, 2H), 7.87 – 7.81 (m, 2H), 4.86 (t, J = 6.9 Hz, 2H), 2.26 (t, J = 7.5 Hz, 2H), 2.06 (t, J = 7.7 Hz, 2H), 1.55 (p, J = 7.7 Hz, 2H).

*NannPerL5COOH (**L5**)*

^{1}H NMR (500 MHz, DMSO-d_6) δ 11.94 (s, 1H), 8.76 (d, J = 7.5 Hz, 2H), 8.18 (d, J = 8.0 Hz, 2H), 8.06 (d, J = 8.8 Hz, 2H), 7.96 (d, J = 8.8 Hz, 2H), 7.82 (t, J = 7.8 Hz, 2H), 4.81 (t, J = 6.9 Hz, 2H), 2.13 (t, J = 7.3 Hz, 2H), 2.03 (p, J = 7.1 Hz, 2H), 1.54 (p, J = 7.5 Hz, 2H), 1.31 (tt, J = 9.8, 6.3 Hz, 2H).

*NannPerL6COOH (**L6**)*

^{1}H NMR (400 MHz, DMSO-d_6) δ 11.91 (s, 1H), 8.73 (d, J = 7.5 Hz, 2H), 8.15 (d, J = 8.0 Hz, 2H), 8.02 (d, J = 8.8 Hz, 2H), 7.93 (d, J = 8.8 Hz, 2H), 7.79 (t, J = 7.8 Hz, 2H), 4.77 (t, J = 6.9 Hz, 2H), 2.09 (t, J = 7.2 Hz, 2H), 1.97 (p, J = 7.0 Hz, 2H), 1.37 (tq, J = 10.2, 5.1, 3.2 Hz, 2H), 1.27 (m, J = 4.1, 3.2 Hz, 4H).

*NannPerL7COOH (**L7**)*

^{1}H NMR (400 MHz, DMSO-d_6) δ 8.74 (d, J = 7.5 Hz, 2H), 8.16 (d, J = 8.0 Hz, 2H), 8.04 (d, J = 8.8 Hz, 2H), 7.94 (d, J = 8.8 Hz, 2H), 7.80 (t, J = 7.8 Hz, 2H), 4.79 (t, J = 6.9 Hz, 2H), 2.08 (t, J = 7.4 Hz, 2H), 1.99 (t, J = 7.0 Hz, 2H), 1.38 (p, J = 7.4 Hz, 2H), 1.26 (dd, J = 6.7, 3.2 Hz, 4H),

1.19 – 1.10 (m, 2H). ^{13}C NMR (125 MHz, CDCl$_3$) δ 174.5, 131.6, 129.5, 128.3, 125.2, 124.7, 124.0, 123.6, 121.0, 116.3, 114.4, 45.1, 33.7, 30.7, 28.5, 28.3, 26.3, 24.4.

Iron^{III} 5,10,15,20-Tetra (4'-N,N,N-Trimethylanilinium) Porphyrin Pentachloride (FeTMA)

The commercially available free-base porphyrin 5,10,15,20-Tetra (4′-N,N,N-Trimethylanilinium) porphyrin tetrachloride (Frontier Scientific) was metalated using an existing literature procedure[42] and characterized by UV-vis spectroscopy as shown in Figure 2.10.

*UV-vis spectrum of **FeTMA** in aqueous solution*
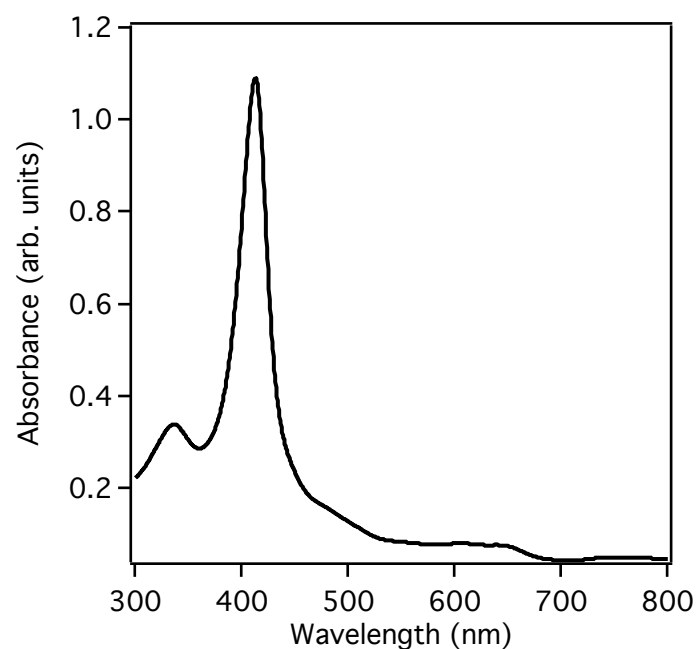
Figure 2.10. UV-vis absorbance spectrum of **FeTMA** in aqueous solution.

Transmission electron microscopy

Transmission electron microscopy imaging was performed on a JEOL 1230 microscope, operating at 100 kV. A ca. 7 µL droplet was placed on a lacey carbon copper grid (Electron Microscopy Science) and allowed to evaporate. The grid was then stained with 10 µL of 1 wt % uranyl acetate. The images were recorded with an AMT camera system.

Cryogenic transmission electron microscopy

Cryogenic transmission electron microscopy imaging was performed on a JEOL 1230 microscope, operating at 100 kV. A ca. 7 μL droplet was placed on a lacey carbon copper grid (Electron Microscopy Science). The grid was held by tweezers mounted on a Vitrobot Mark IV equipped with a controlled humidity and temperature environment. The temperature was set to 24 °C and humidity was held at 90%. The specimen was blotted and plunged into a liquid ethane reservoir cooled by liquid nitrogen. The vitrified samples were transferred to a Gatan 626 cryo-holder through a cryo-transfer stage cooled by liquid nitrogen. During observation of the vitrified samples, the cryo-holder temperature was maintained below -180 °C. The images were recorded with a CCD camera.

Scanning electron microscopy

SEM was performed on a Hitachi S-4800 II SEM. The samples were dried using CO_2 critical point drying. The samples were placed in a metallic cage and soaked in 25% ethanol/water solutions for 10 minutes. This process was repeated with 50, 60, 70, 80, 90, 95, and 100% ethanol solutions. The ethanol exchanged samples were then critical point dried with supercritical CO_2 for 10 minutes using a Tousimis Samdri 795. Samples were placed on a carbon tape-coated aluminum stub and coated with 20 nm osmium metal using a Filgen Osmium Plasma Coater OPC60A.

Photocatalysis

The following describes the general procedure used for performing photocatalysis experiments. A 1-mL aqueous solution was prepared containing 1 mM chromophore, 5 µM **FeTMA**, 50 mM sodium ascorbate, 100 mM $NaHCO_3$ (in some cases, see section 2.3.3). The solution was sealed in an 8.5-mL vial with septum screw top cap and degassed with CO_2 for 10 minutes, after which NaOH was added in some experiments to adjust the pH. The samples were then illuminated with a white light source for two days. The emission spectrum of this light source is shown in Figure 2.11. After illumination, the vial
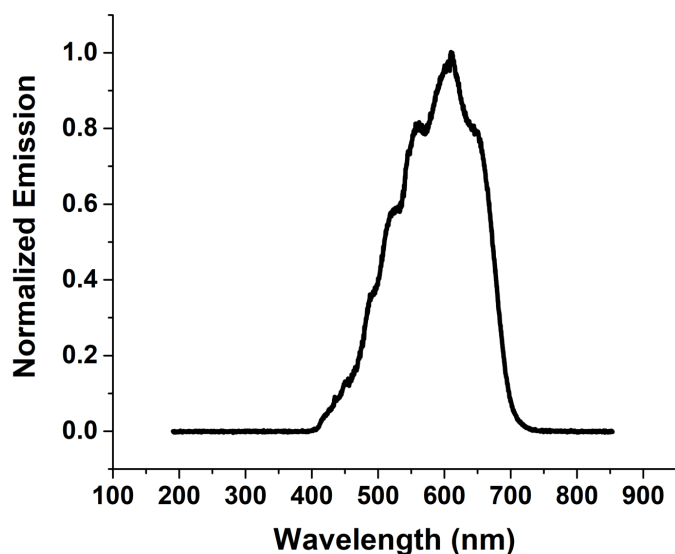
Figure 2.11. Emission of white light source used in photocatalysis experiments.

headspace gases were identified and quantified using gas chromatography (Shimadzu GC-2014, ShinCarbon ST column, Ar carrier gas, TCD detector) by injection of 500 µL of the headspace gas and comparison of the resulting peak areas to a calibration curve.

Chapter 3 : Investigating the interaction between $CuInS_2$@ZnS quantum dots and an iron porphyrin CO_2 reduction catalyst

3.1.　Chapter Summary

This chapter describes the investigation of potential binding interactions between an iron porphyrin CO_2 reduction catalyst (FeTPP) and mercaptopropanol (MPO)-capped $CuInS_2$@ZnS (CIS) QDs. Motivated by previous observation of ultrafast electron transfer from CIS QDs to FeTPP, ^{1}H NMR, UV-vis, and X-ray spectroscopies as well as cyclic voltammetry were used to probe the possibility of a nonspecific hydrophobic interaction between CIS QDs and FeTPP. The data clearly indicate that CIS QD solutions, which contain both bound and free MPO, chemically reduce the iron center of FeTPP from Fe^{III} to Fe^{II} (in the dark), and that FeTPP dimerization can occur under some conditions. Firm NMR spectroscopic evidence for FeTPP binding to CIS QD surfaces could not be obtained, generally due to complications resulting from the paramagnetic iron center. Experiments with a diamagnetic ZnTPP analog suggest but do not prove that a nonspecific hydrophobic interaction between FeTPP and CIS QDs could occur, but more experiments are needed to make stronger conclusions.

3.2.　Introduction

As discussed in Chapter 1, photocatalytic CO_2 reduction is a key component in the overall generation of solar fuels, but has numerous inherent challenges, one of which is efficient charge transfer from photosensitizer to CO_2 reduction catalyst. One method to increase the rate of charge transfer is supramolecular assembly, which in this case aims to co-localize photosensitizer and catalyst via non-covalent forces such as electrostatic attraction or hydrophobic collapse.

QDs have emerged as viable photosensitizer candidates for CO_2 reduction due to their high absorption cross-sections in the visible region and tunable surface chemistry.[12] In particular, $CuInS_2$@ZnS QDs (CIS QDs) are promising candidates due to the aforementioned features as well as their high reduction potentials (ca. -2.4 V vs. SCE) which generate a strong driving force for

electron transfer to catalysts, and potential lower toxicity relative to other QDs, which typically contain cadmium or lead.

Recently, Weiss *et al.* used CIS QDs to photosensitize an iron porphyrin CO_2 reduction catalyst, iron tetraphenylporphyrin (FeTPP), in dimethylsulfoxide (DMSO) solution.[46] In terms of turnovers of CO per photon absorbed, the system was considerably more efficient than similar published systems employing FeTPP and transition-metal complexes or organic dyes as photosensitizers.[47] Transient absorption spectroscopy suggested that extremely fast electron transfer from CIS QDs to FeTPP was occurring, on the order of <200 fs. This is considerably faster than the timescale of diffusion in the system, therefore suggesting that FeTPP is likely bound to the surface of CIS QDs. We wished to probe this interaction more closely to determine the mode of interaction, if any, between CIS QDs and FeTPP. Before presenting the results, some relevant key characteristics of FeTPP are reviewed.

3.2.1 *Characteristics of iron tetraphenylporphyrin*

FeTPP has been thoroughly studied since the 1960s,[48] first as a hemin analog[49-50] before it found use as an efficient homogeneous CO_2 reduction electrocatalyst,[51-52] with high selectivity for the two electron, two proton reduction of CO_2 to CO over other carbonaceous products or hydrogen evolution. Its features particularly relevant to our results will be discussed here; for additional information the reader is referred to other texts.[53] FeTPP is typically prepared as [Fe^{III}(TPP)Cl], where TPP is the doubly deprotonated 5,10,15,20-*meso*-tetraphenylporphyrin ring that carries a -2 charge. In polar solvents such as DMSO and *N,N*-dimethylformamide (DMF), the chloride anion typically dissociates,[54] resulting in [Fe^{III}(TPP)]$^+$, which tends to quickly bind a solvent molecule, forming [Fe^{III}(TPP)(solv)]$^+$.

Both electro- and photochemical CO_2 reduction with FeTPP proceeds via three successive reductions of the initially prepared $[Fe^{III}TPP(solv)]^+Cl^-$ species.[55] These reductions are observed by cyclic voltammetry (CV) as shown in Figure 3.1. The first reduction is metal-centered and involves dissociation of Cl^- and/or solvent, resulting in the formation of four-coordinate $Fe^{II}TPP$. The nature of the
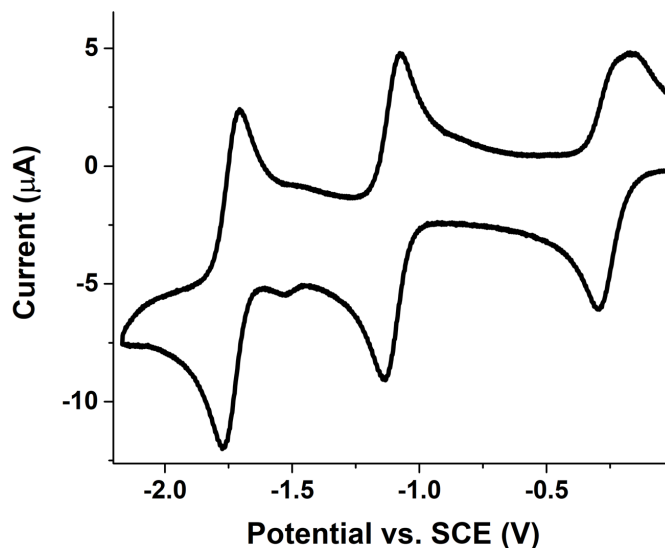
Figure 3.1. Cyclic voltammogram of 1 mM FeTPP dissolved in DMF, with 100 mM $TBAPF_6$ supporting electrolyte, collected at 50 mV/s using a glassy carbon working electrode, Pt counter electrode, and Ag wire pseudoreference (a ferrocene internal standard was used and the value converted to SCE).

subsequent two reductions has been debated in the literature, with some thinking them to be metal-centered, resulting in $[Fe^0(TPP)]^{2-}$ and others presenting evidence that they are ligand-centered, resulting in $[Fe^{II}TPP)^{2-}]^{2-}$, where the TPP has accepted both electrons and now has a total -4 charge.[56] As can be seen from the voltammogram in Figure 3.1, $Fe^{III}TPP$ is reduced to $Fe^{II}TPP$ at a relatively low potential. Thiols have been commonly used to perform this reduction chemically.[57] If the thiol is deprotonated to a thiolate, it may weakly bind to $Fe^{II}TPP$, forming $[Fe^{II}TPP(RS^-)]^-$. An overall summary of these interactions is given in Scheme 3.1.

Porphyrins exhibit strong visible-light absorption. Their most intense visible band is called the Soret band, located around 400-420 nm. The Soret band shifts when the porphyrin is metalated and is diagnostic of the oxidation state of the complex. Porphyrins also exhibit a number of lower energy bands called Q bands, which are often complicated but can sometimes be used to identify coordination and/or oxidation states. While the Soret band has a high molar absorptivity, it is

relatively narrow and only absorbs blue light, while the Q bands have significantly lower oscillator strength. Photosensitization by QDs or other appropriate light-absorbing species is therefore desirable in order to absorb more visible light (and thus harness more energy in that spectral range).

Due to the iron metal center, FeTPP is paramagnetic at all oxidation states. This makes it challenging, but not impossible, to study by NMR spectroscopy, as unpaired electrons interact with nuclear spins, resulting in significant broadening and/or line shifts.[53, 58]

$$[Fe^{III}TPP]_2O$$

$$\text{base} \updownarrow \text{acid}$$

$$O_2$$

$$[Fe^{III}TPPCl] \rightleftharpoons [Fe^{III}TPP(solv)]^+Cl^-$$

$$\downarrow RSH \text{ or } RS^-BA^+$$

$$[Fe^{II}TPP] \rightleftharpoons [Fe^{II}TPP(RS^-)]^-BA^+$$
(if RS^-BA^+ used)
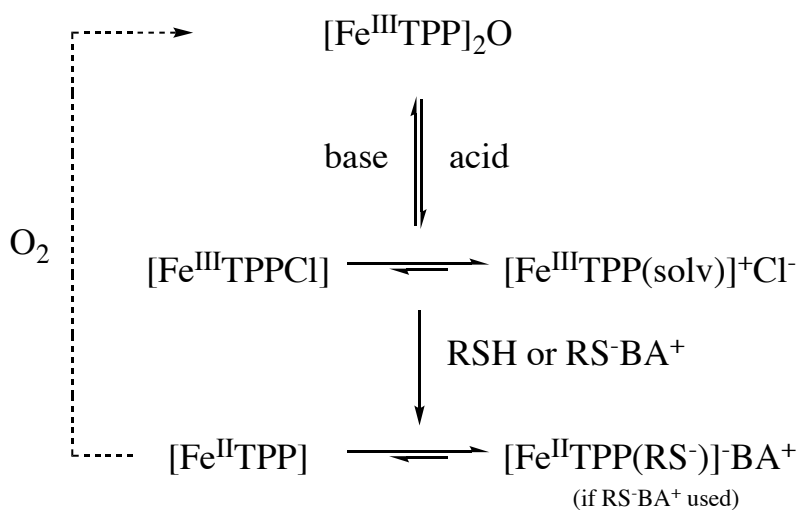
Scheme 3.1. Diagram of common oxidation states and ligand coordination of FeTPP in polar solvents.

FeTPP is also prone to dimerization to the μ-oxo dimer $[Fe^{III}TPP]_2O$, two FeTPP units bridged by an Fe-O-Fe bond.[59] This dimer is formed by either i) treatment of $Fe^{III}TPP$ with base or ii) the oxidation of $Fe^{II}TPP$ by oxygen to form a peroxo dimer that rapids decomposes to the oxo dimer. The dimer has a slightly blue-shifted Soret band due to weak coupling between the two porphyrin units, and also exhibits changes in the Q bands. The electrochemical properties of the dimer are slightly different than the monomer,[55] as will be further discussed later. Scheme 3.1 summarizes these interactions.

3.2.2 Investigation of FeTPP-QD binding interactions

This work aimed to further investigate the existence and nature of any interactions between FeTPP and CIS QDs that would explain the previous observation of sub-diffusional electron transfer from QDs to FeTPP.[46] We hypothesized that the most likely mode of interaction was a

nonspecific solvophobic interaction, because i) the rigid planar geometry and π system of FeTPP is not highly soluble in DMF or DMSO and ii) there is no obvious mode of coordination of FeTPP to QDs besides coordination of the hydroxyl group of MPO to the iron center, but that interaction is known to be very weak. We investigated this potential interaction via UV-vis, ^{1}H NMR and T_2 relaxation ^{1}H NMR experiments, and *in-situ* electrochemical X-ray absorbance near edge spectroscopy (XANES). We were unable to confirm any binding interaction between FeTPP and QDs but did find that addition of QDs (as a solution that also contains excess MPO ligands) to FeTPP causes spontaneous chemical reduction from Fe[III]TPP to Fe[II]TPP.

3.3.   Results and Discussion

3.3.1   QD synthesis and ligand exchange to MPO

CIS QDs were synthesized using a previously published thiol-free procedure, which yields QDs with a diameter around 2.5 nm.[60] The QDs are coated with a sub-monolayer shell of ZnS, which greatly improves colloidal and photo-stability, and oleate ligands. Ligand exchange was performed to replace these oleate ligands with 3-mercaptopropanol (MPO), which solubilizes QDs in polar organic solvents such as *N,N*-dimethylformamide (DMF) and dimethylsulfoxide (DMSO). Two slightly different procedures were used, as shown in Scheme 3.2. To a solution of oleate-capped CIS QDs in toluene (typically 1-3 mL of concentration 0.6-0.8 mM) was added either i) 200 equiv MPO (neat) or ii) a mixture of 400 equiv MPO and 520 equiv benzyltrimethylammonium hydroxide (also called Triton-B) (all equiv measured per QD). The addition of base to MPO deprotonates the thiol to create thiolates, which strongly bind to the QD surface. The base is not strictly necessary because MPO can also be deprotonated by oleate at the QD surface prior to irreversibly binding as thiolates. The base presumably increases the kinetics of the ligand exchange by deprotonating the thiol beforehand. The mixture was shaken and
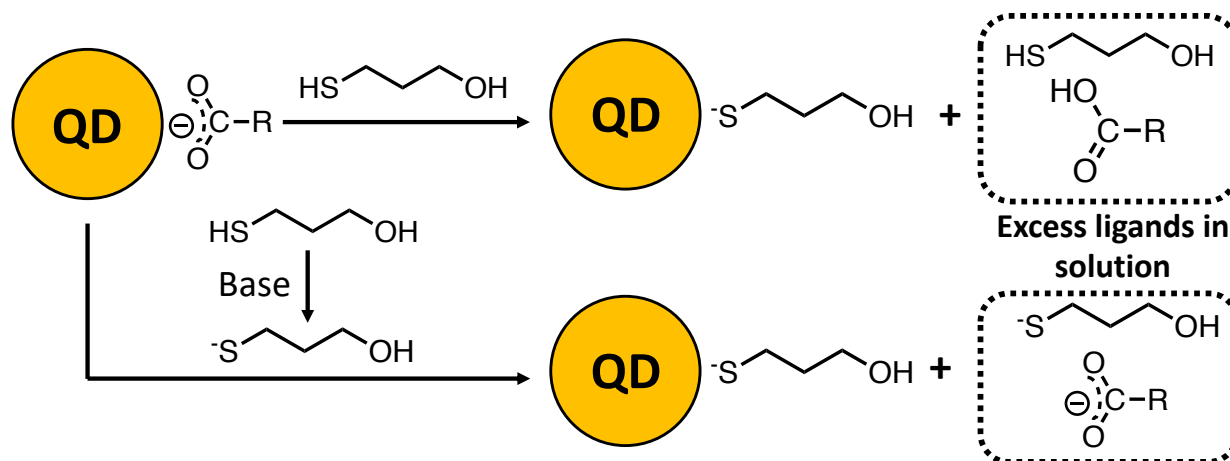
Scheme 3.2. Schematic of thiol(ate) ligand exchange procedure used in this work, with structures of excess ligands remaining in solution after exchange shown on right-hand side.

vortexed, then 1-2 mL of additional toluene was added, and the mixture was shaken and vortexed again. The mixture was centrifuged at 7500 rpm for 5 minutes. The supernatant was decanted, and the remaining reddish orange solid was lightly dried with a flow of N_2 gas. The solid was redissolved in either DMF or DMSO. It is important to note that this procedure does not fully wash out excess ligands. In the exchange without base, the excess ligands in solution are oleate and thiol, while when base is used there are thiolates and oleates present, as shown in Scheme 3.2. The presence of these excess ligands can have a strong effect on the behavior of the QD-FeTPP system, as will be discussed below. The ligand exchange procedure could likely be improved to avoid excess ligands, by using fewer ligands and/or adding additional washing steps, but we intentionally did not do this in order to maintain the same conditions used in the previous experiments[46] on which our hypothesis was based.
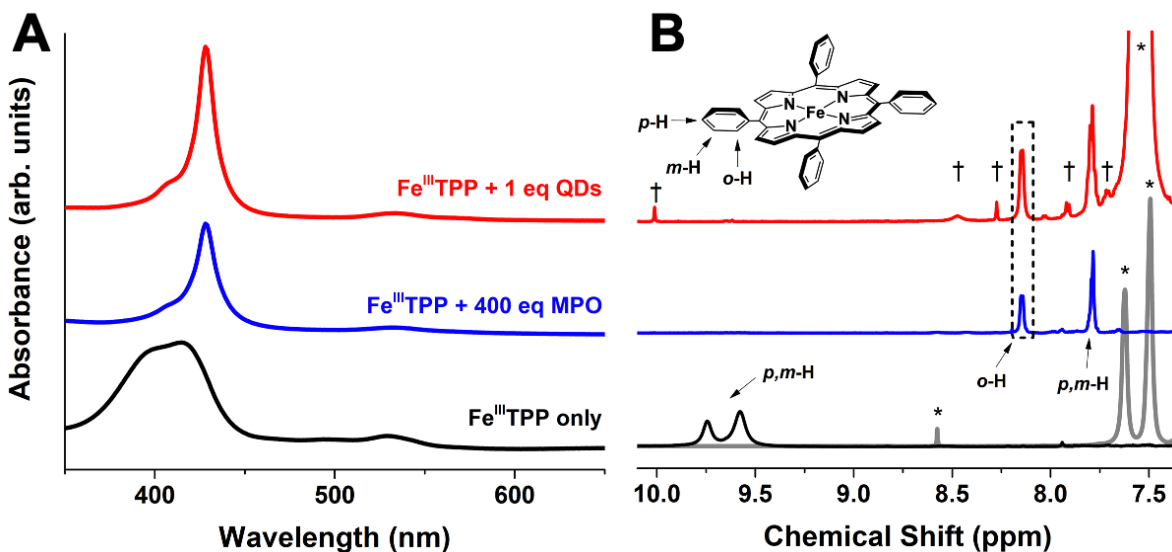
Figure 3.2. (A) UV-vis spectra of DMSO solutions of $Fe^{III}TPP$ alone (black) with 400 equiv MPO (blue) and with 1 equiv MPO-capped CIS QDs (red), all under CO_2 atmosphere. (B) ^1H NMR spectra of DMSO-d_6 solutions of $Fe^{III}TPP$ alone (black) with 400 equiv MPO (blue) and with 1 equiv MPO-capped CIS QDs (red), all under CO_2 atmosphere. The ^1H NMR spectrum of MPO-capped CIS QDs alone is shown in gray. Asterisks (*) denote signals corresponding to Triton-B and crosses (†) denote signals corresponding to $Fe^{II}TPP(RS^-)$.

3.3.2 $Fe^{III}TPP$ is reduced to $Fe^{II}TPP$ in the presence of QDs

Mixing a solution of $Fe^{III}TPP$ with MPO-capped CIS QDs in DMF or DMSO results in reduction of $Fe^{III}TPP$ to $Fe^{II}TPP$. This is clearly observed by a red shift in the Soret band in the UV-vis spectrum of a solution of FeTPP and 1 equiv QDs, shown in Figure 3.2(A). The same shift can be produced by addition of excess MPO to a solution of FeTPP, also shown in Figure 3.2(A). As mentioned in Section 3.2, thiols are relatively electron-rich molecules that are known to reduce the metal center of iron porphyrins from Fe^{III} to Fe^{II}. When two thiols reduce two $Fe^{III}TPP$ molecules, they form a single disulfide molecule. Reduction of $Fe^{III}TPP$ most likely occurs via oxidation of either a free thiol(ate) (left over from ligand exchange, see Scheme 3.2) or a thiol(ate) that has desorbed from a QD surface. Further evidence for the presence of $Fe^{II}TPP$ and thiol oxidation is found in the ^1H NMR spectrum of a mixture of QDs and $Fe^{III}TPP$ in DMSO-d_6. As shown in Figure 3.2(B), peaks in the aromatic region corresponding to the phenyl protons of TPP shift considerably, and match literature assignments for $Fe^{II}TPP$.[58] The additional peaks marked

with crosses are assigned to $Fe^{II}TPP(RS^-)$, where RS^- is a deprotonated MPO thiolate. As shown in Figure 3.3, this species is only formed in the presence of excess thiolates, which exist when base is used in the ligand exchange (see Scheme 3.2). Thiolates can weakly bind to $Fe^{II}TPP$, while thiols are much less likely to bind.[57] The effect of this species will be discussed further in the next section. Figure 3.4 shows the alkyl region of ^1H NMR spectra of a solution of QDs alone (black) and with $Fe^{III}TPP$ added (red), which reveals an increase in signals

Figure 3.3. ^1H NMR spectra of DMSO-d_6 solutions of $Fe^{III}TPP$ with 1 equiv QD (no base used in ligand exchange, see text) (black), $Fe^{III}TPP$ with 400 MPO (no base added) (blue), $Fe^{III}TPP$ with 1 equiv QD (base used in exchange) (yellow), and $Fe^{III}TPP$ with 400 equiv MPO and 520 equiv Triton-B (green), all under CO_2 atmosphere. Asterisks (*) denote signals corresponding to Triton-B and crosses (†) denote signals corresponding to $Fe^{II}TPP(RS^-)$.

assigned to oxidized dithiol after QD addition. The signals were not integrated due to uncertainty about the broad features underlying the peaks (probably contribution from molecules bound to QDs). The generation of disulfide peaks could also be observed in a sample of FeTPP with only free MPO added, shown in Figure 3.5. Confirmation of $Fe^{III}TPP$ reduction to $Fe^{II}TPP$ was also made using X-ray absorption near edge spectroscopy (XANES), which revealed reduction of the Fe center in the presence of QDs (without any applied electrical potential), as shown in Figure 3.10. The XANES data are further discussed in section 3.3.4. Taken together, the UV-vis, ^1H NMR, and XANES data indicate that excess MPO, either as protonated thiol or deprotonated thiolate, present in solution with MPO-capped CIS QDs, chemically reduce $Fe^{III}TPP$ to $Fe^{II}TPP$. This has implications for the proposed mechanism of photosensitized CO_2 reduction by QDs, as

initially it was thought that three electron transfers were needed for catalysis to occur (at least for the initial catalytic cycle), but initial chemical reduction to $Fe^{II}TPP$ would suggest that only two electron transfers are required.

3.3.3 ^1H NMR T_2 decay experiments to detect binding of porphyrins to QDs

We measured the T_2 relaxation time of the phenyl protons of FeTPP in the presence of QDs to determine whether it was adsorbed to QD surfaces. T_2 is inversely related to the rotational correlation time of a species; therefore, for molecules adsorbed to the surfaces of larger, more slowly rotating nanoparticles, T_2 decreases relative to the freely diffusing species.[61-63] The Carr-Purcell-Meiboom-Gill (CPMG) pulse sequence applies a 90° pulse to the sample, followed by a 180° spin echo pulse at varying delay times. The decay in the nuclear spins refocused by the spin echo pulse is measured by the integrated
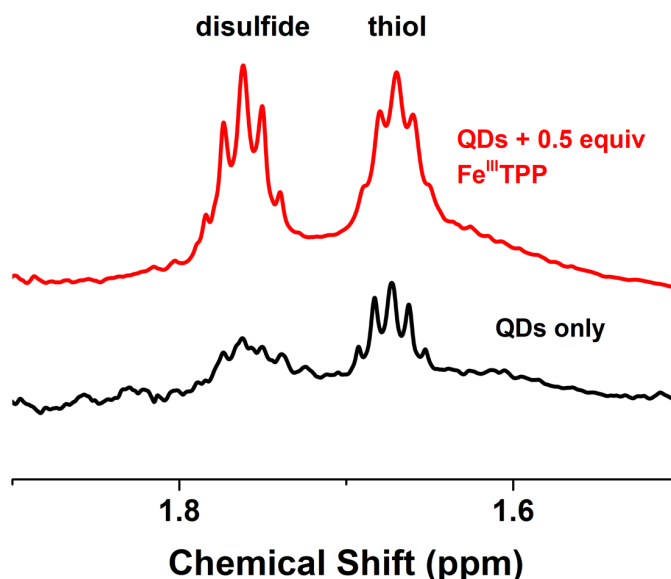
Figure 3.4. ^1H NMR spectra of 1 mM MPO-capped CIS QDs alone (black) and 1 mM QDs with 0.5 equiv $Fe^{III}TPP$ (red), showing thiol and disulfide proton resonances.
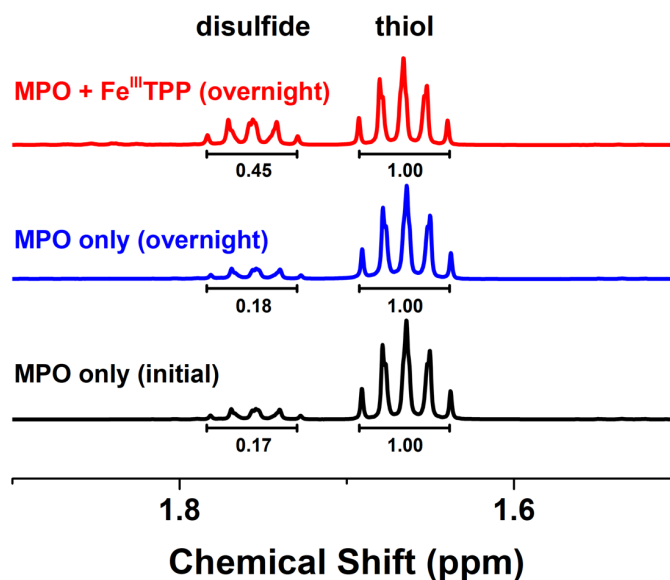
Figure 3.5. ^1H NMR spectra of 20 mM MPO (initially dissolved in DMSO-d_6, black, and after sitting under ambient atmosphere overnight, blue) and 20 mM MPO with 333 µM $Fe^{III}TPP$ after sitting under ambient atmosphere overnight (red). The values below the peaks are the peak integration values.

intensities of the resulting peaks, which, plotted as a function of delay time, are fit to Equation 3.1 to give T_2 for the integrated peak.

$$M_y(t) = M_0 e^{-t/T_2} \text{ (Equation 3.1)}$$

As mentioned in the introduction, a major drawback in using this method for our system is that the iron center in FeTPP is paramagnetic at all oxidation states. The presence of an unpaired electron can have a strong yet not easily predictable effect on the T_2 relaxation times of nearby protons. Nevertheless, we hypothesized that we might see a significant difference between T_2 of $Fe^{II}TPP$ alone (chemically reduced by free MPO) and T_2 of $Fe^{II}TPP$ mixed with CIS QDs. As shown in Figure 3.6, we initially did observe a decrease in T_2 of the phenyl protons of FeTPP after mixing with QDs. However, careful examination of the ^{1}H NMR spectrum of this sample revealed that multiple FeTPP species were present. We determined that while nearly all $Fe^{III}TPP$ was
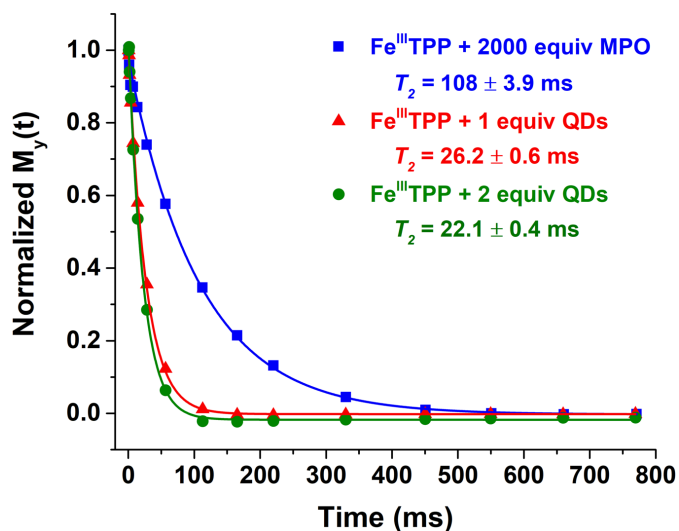
Figure 3.6. Spin-spin (T_2) relaxation measurements of o-phenyl proton resonance (at 8.17 ppm) of 500 µM FeTPP in the presence of 2000 equiv MPO (blue), 1 equiv MPO-capped CIS QDs (red), or 2 equiv MPO-capped CIS QDs (green), under CO_2 in DMSO-d_6. The data were fit to single exponential decays, with extracted T_2 values listed in the legends. MPO-capped CIS QDs were prepared using a ligand exchange with base, see Scheme 3.2 and main text.
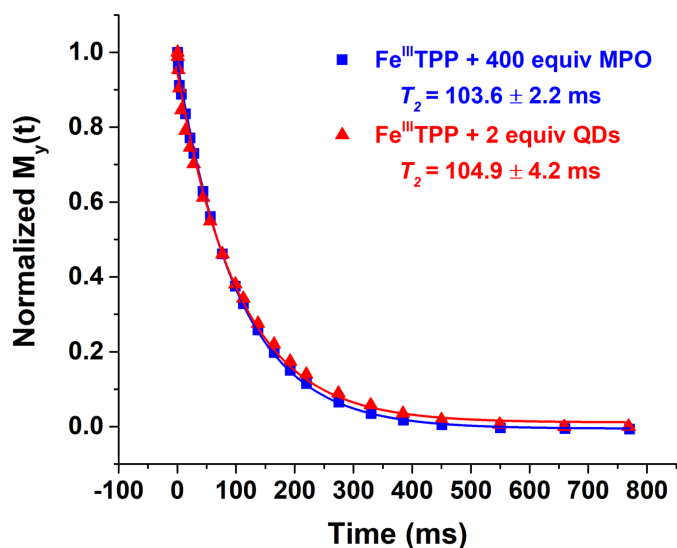
Figure 3.7. Spin-spin (T_2) relaxation measurements of o-phenyl proton resonance (at 8.17 ppm) of 500 µM FeTPP in the presence of 400 equiv MPO (blue) or 1 equiv MPO-capped CIS QDs (red) under CO_2 in DMSO-d_6. The data were fit to single exponential decays, with extracted T_2 values listed in the legends. MPO-capped CIS QDs were prepared using a ligand exchange without base, see Scheme 3.2 and main text.

reduced to $Fe^{II}TPP$, some $Fe^{II}TPP$ also coordinated thiolates, forming $[Fe^{II}TPP(RS^-)]$, where RS^- is a deprotonated MPO thiolate. The NMR signals corresponding to this species are marked with a cross in Figure 3.2(B) and 3.3. These initial T_2 experiments were performed using the aforementioned ligand exchange that used the base Triton-B to form thiolates. Some thiolates probably remained in the QD mixture even after the washing step of the ligand exchange. We
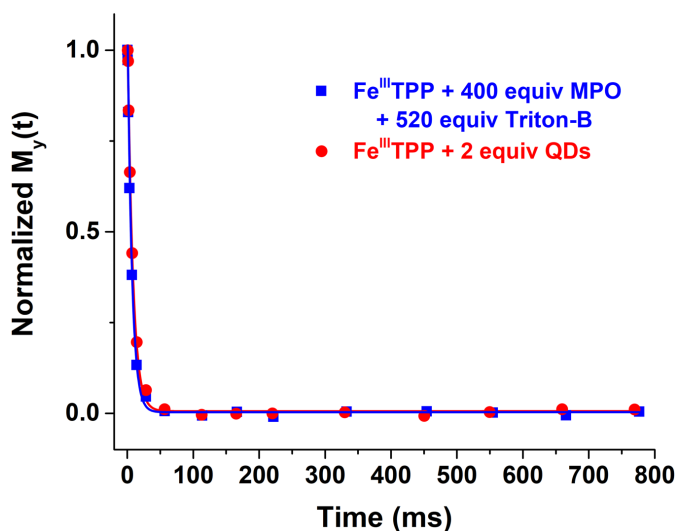
Figure 3.8. Spin-spin (T_2) relaxation measurements of $Fe^{II}TPP(RS^-)$ phenyl proton resonance at 10.8 ppm in presence of 400 equiv MPO and 520 equiv Triton-B (blue) or 2 equiv MPO-capped CIS QDs (red). All samples were prepared at [FeTPP] = 500 μM in DMSO-d_6 under N_2 atmosphere. The data were fit to single exponential decays: without QDs, $T_2 = 6.7 \pm 0.2$ ms; with 2 equiv QDs, $T_2 = 8.0 \pm 0.2$ ms.

found that this $[Fe^{II}TPP(RS^-)]$ species, which is also paramagnetic, had phenyl proton resonances with extremely short T_2 times, as shown in Figure 3.8. We hypothesized that the presence of this paramagnetic species may affect the T_2 lifetime of other species in the solution as well. We repeated the experiment performing the QD ligand exchange without any additional base, which avoids the formation of excess thiolates. As shown in Figure 3.3 (blue spectrum), when no excess thiolates are present, ^1H NMR signals corresponding to $[Fe^{II}TPP(RS^-)]$ do not appear. More consequentially, T_2 of the phenyl proton resonances of $Fe^{II}TPP$ do not change in the presence of QDs, as shown in Figure 3.7. This indicates that i) the presence of paramagnetic $[Fe^{II}TPP(RS^-)]$ likely affects the T_2 decay time of protons of $Fe^{II}TPP$ and ii) $Fe^{II}TPP$ may not be adsorbed to QDs, as T_2 should decrease if the tumbling rate of $Fe^{II}TPP$ was decreased by adsorption to QDs.

We also considered the possibility that the paramagnetic effect on the T_2 of the phenyl protons of FeTPP is so large that it prevents us from observing any change in T_2 upon FeTPP adsorption to QDs. In fact, T_2 is nearly an order of magnitude shorter for $Fe^{II}TPP$ than its diamagnetic analog, ZnTPP. We hypothesized that if FeTPP were binding to QDs via a nonspecific solvophobic interaction, the same interaction would likely be observed between QDs and ZnTPP. Figure 3.9 shows the T_2 decays for one of the phenyl proton resonances of
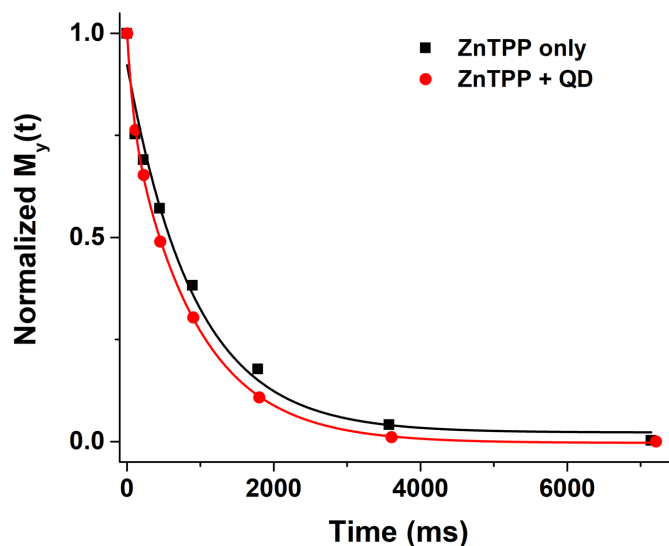
Figure 3.9. Spin-spin (T_2) relaxation measurements of the phenyl proton resonance at 8.17 ppm of 500 µM ZnTPP alone or with 2 equiv MPO-capped CIS QDs in DMSO-d_6 under ambient atmosphere. The data without QDs were fit to a single exponential decay, while the data with QDs were fit to a sum of two exponentials, where one time constant was fixed to the time constant obtained from the sample without QDs (914.7 ± 143.4 ms). In the presence of QDs, the additional time constant is 83.6 ± 9.7 ms (18.9 ± 0.9%).

ZnTPP alone and in the presence of 2 equiv QDs. In the presence of QDs, the data were fit to a biexponential decay in which the longer time constant was set to the time constant obtained without QDs, revealing a second, shorter time constant of 83.6 ± 9.7 ms, with ~20% amplitude. The presence of this shorter time constant suggests that ZnTPP may be bound to QDs, decreasing its tumbling rate in solution and therefore decreasing T_2. These data, along with the clear effect of paramagnetic center on the T_2 value in FeTPP, suggest that FeTPP may be bound to QDs but that the resulting change in T_2 is not detectable due to the paramagnetic nature of FeTPP.

3.3.4   Other methods used to probe QD-FeTPP interaction

In-situ electrochemical X-ray absorption near edge spectroscopy (XANES) was performed in collaboration with the Chen lab in order to probe the effect of QDs on the oxidation state of the

iron center of FeTPP at various applied potentials. As shown in Figure 3.10, the Fe K-edge shifts to lower energy in the presence of QDs with no applied potential, which indicates an increase in electron density at the iron center of FeTPP. These samples were prepared using ligand exchanges without additional base, so excess thiolates should not be present. The more reduced iron center could be due to an
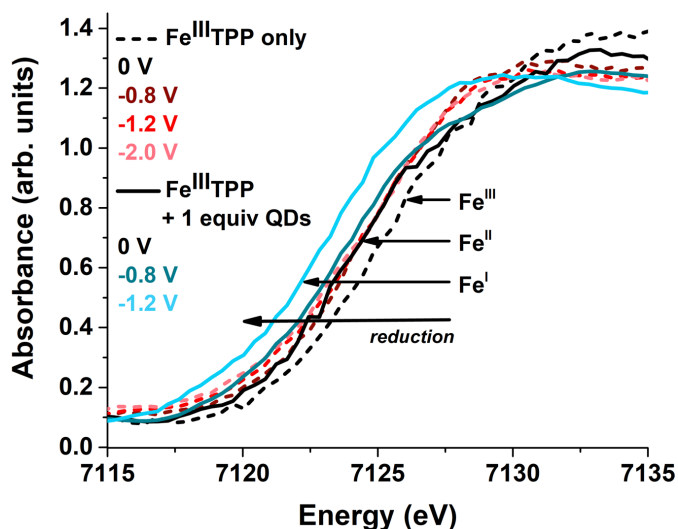
Figure 3.10. *In-situ* electrochemical XANES spectra, Fe K-edge region, of 500 μM FeTPP in DMF at 0 V, -0.8 V, -1.2 V, and -2.0 V applied potentials (dashed lines) and 500 μM FeTPP mixed with 1 equiv MPO-capped CIS QDs in DMF at 0 V, -0.8 V, and -1.2 V applied potential (solid lines).

electronic interaction between the QD surface and FeTPP. For instance, if the iron center may be coordinated to an unpassivated electron-rich S atom on the QD surface. Such an interaction may have passed undetected by ^{1}H NMR spectroscopy if FeTPP is tightly bound to QDs, as the NMR signals would likely be so broadened as to be undetectable. The XANES data also reveal differences in the electronic structure of FeTPP under applied electrochemical potential when in the presence of QDs. As shown in Figure 3.10, when FeTPP is the only species in solution, applying a potential of -0.8 V vs. SCE reduces Fe^{III}TPP to Fe^{II}TPP, resulting in a shift of the K-edge to lower energy, as expected for a metal-centered reduction. Applying additional potential to this species results in no further shift in K-edge energy, despite the presence of two additional CV waves (shown in Figure 3.1). This is evidence that the two additional reductions are ligand-centered and therefore do not change the electron density on the iron center, as has been shown in similar experiments in the literature.[56] However, when QDs are present, the K-edge shifts to lower energy when a potential of -1.2 V vs. SCE is applied. This could indicate the presence of electronic

interactions between QDs and FeTPP that result in a metal-centered reduction of Fe^{II}TPP. Further work is needed to fully understand this phenomenon.
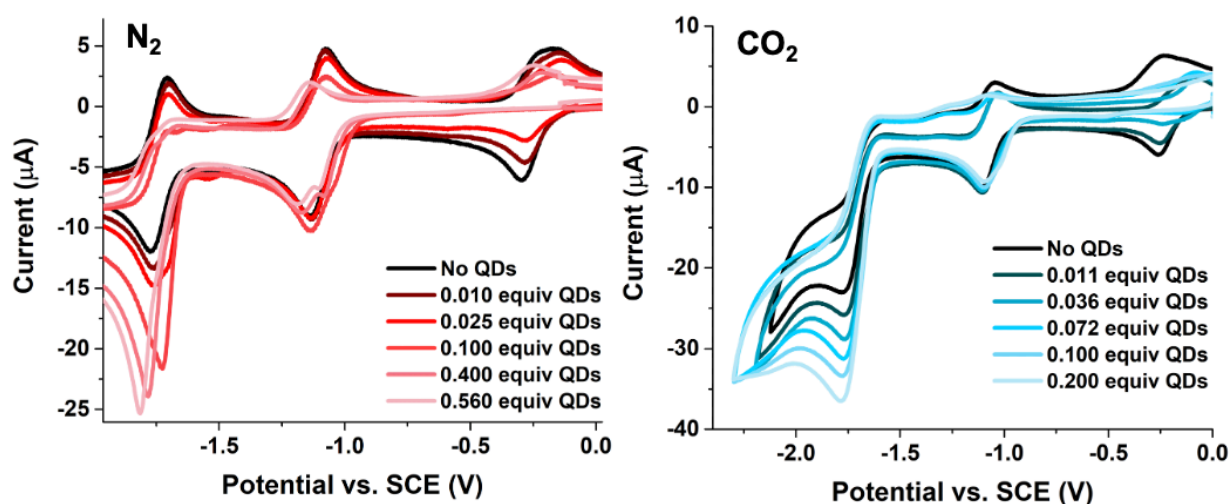
Figure 3.11. Cyclic voltammagrams of 1 mM FeTPP with various equivalents of MPO-capped CIS QDs added, under N_2 (left) or CO_2 (right) atmosphere. All samples are anhydrous DMF solutions containing 100 mM TBAPF$_6$, collected at 50 mV/s using a glassy carbon working electrode, Pt counter electrode, and Ag pseudoreference electrode (internally referenced to ferrocene and converted to SCE).

Cyclic voltammetry was also used to investigate QD-FeTPP interactions. Initial experiments found that addition of QDs to FeTPP in DMF resulted in a loss of the Fe^{III}/Fe^{II} couple, as shown in Figure 3.11, and an increase in current and loss of reversibility in the formal Fe^{I}/Fe^{0} couple, attributed to proton reduction due to an increase in protons in solution (from MPO ligands). The loss of the Fe^{III}/Fe^{II} couple was initially attributed to the chemical reduction of Fe^{III}TPP to Fe^{II}TPP, which was already established by UV-vis and NMR spectroscopic data, as discussed in Section 3.3.2. However, even if a chemical reductant is present to perform this reduction, cyclic voltammetry should still detect the Fe^{III}/Fe^{II} couple, as the electrode is initially set at a potential at which all FeTPP at the electrode surface should be in the Fe^{III} oxidation state. Even if Fe^{III}TPP has been chemically reduced to Fe^{II}TPP, the species at the electrode (which is what is being detected and shown in the voltammogram) will be re-oxidized to Fe^{III}TPP. This effect becomes more apparent when the CV scan is started at the open circuit potential, which is the potential of the

solution when no current is flowing. When MPO or QDs were added to a solution of Fe^{III}TPP, the open circuit potential drifted to more negative potentials, indicating that the solution had become more reducing. When a voltammogram was collected starting from the open circuit potential, the Fe^{III}/Fe^{II} couple could be observed when either QDs or free MPO only were added, as shown in Figure 3.12. The apparent loss of the Fe^{III}/Fe^{II} couple in the earlier experiments appears to be attributable to dimerization of Fe^{II}TPP to [Fe^{III}TPP]$_2$O, which appeared to occur more easily in DMF solution, as seen in the UV-vis spectra shown in Figure 3.13, which show the appearance, as QDs are added to FeTPP, of a blue-shifted shoulder corresponding to the dimer, in addition to the red-shifted Fe^{II}TPP Soret band. When the dimer is formed, the Fe^{III}/Fe^{II} couple shifts to significantly more negative

Figure 3.12. Cyclic voltammograms of MPO-capped CIS QDs only (gray), Fe^{III}TPP only (black), Fe^{III}TPP with 1 equiv MPO-capped CIS QDs (red), and Fe^{III}TPP with 500 equiv MPO (blue). All samples are anhydrous DMSO solutions under N$_2$ containing 100 mM TBAPF$_6$, collected at 50 mV/s using a glassy carbon working electrode, Pt counter electrode, and Ag pseudoreference electrode (internally referenced to ferrocene and converted to SCE).
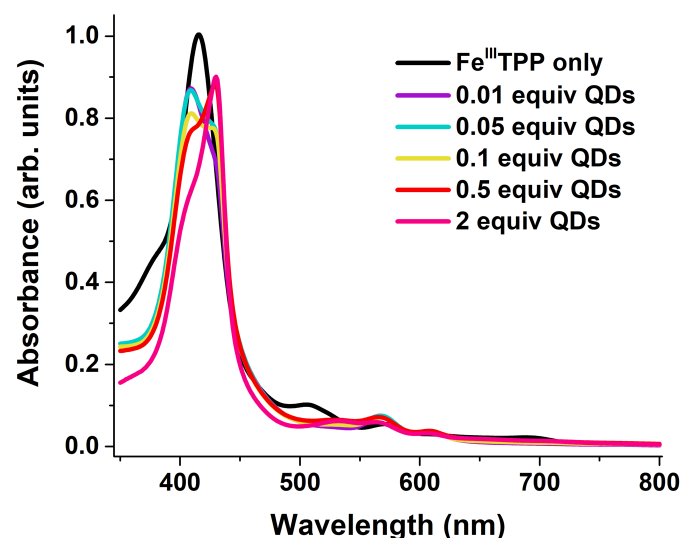
Figure 3.13. UV-vis spectra of Fe^{III}TPP alone (black) and with various equivalents of MPO-capped CIS QDs added (colored) in DMF solution.

potential,[55] which may be responsible for the shoulder observed at the Fe^{II}/Fe^{I} couple in the initial

data. In addition, another feature appearing at around -1.8 V vs. SCE corresponds with another dimer reduction feature. To confirm this assignment, the dimer was synthesized by treatment of $Fe^{III}TPPCl$ with base in $CHCl_3$, followed by purification through an alumina plug.[59] A cyclic voltammogram of the dimer was collected under similar conditions and was found to match literature data well. The dimer voltammogram is shown overlaid with the FeTPP + QD data in Figure 3.14.
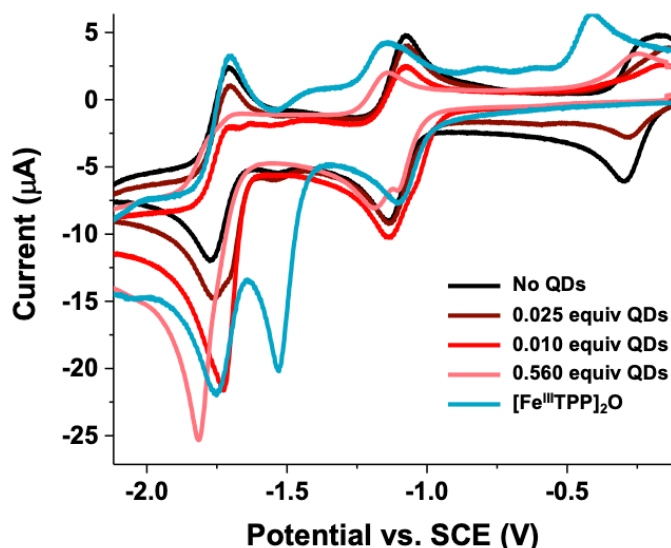
Figure 3.14. Cyclic voltammagram of FeTPP with various equivalents of MPO-capped CIS QDs (black and red traces) and [FeTPP]$_2$O dimer (blue), all under N$_2$ in anhydrous DMF solutions containing 100 mM TBAPF$_6$, collected at 50 mV/s using a glassy carbon working electrode, Pt counter electrode, and Ag pseudoreference electrode (internally referenced to ferrocene and converted to SCE).

Fairly good agreement between the peak potentials in the FeTPP + QD sample and dimer sample are observed. We were unable to extract any further information about the nature of potential interactions of FeTPP with QDs from our existing CV data. However, recent studies suggest that careful study of voltammograms of varying scan rate can characterize binding of substrates to QD surfaces by determination of the diffusion coefficient, which is lower when the species is bound to the relatively large and slowly diffusing QDs.[64] Collection of scan rate dependent CV data for this system may allow for a similar analysis, but the concurrent chemical reduction of $Fe^{III}TPP$ to $Fe^{II}TPP$ by the MPO ligands of QDs, and subsequent dimerization in some solvents, may complicate the analysis, as demonstrated in Figures 3.3 and 3.14.

3.4. Conclusions

This work attempted to elucidate a binding interaction between MPO-capped CIS QDs and FeTPP, which was proposed on the basis of ultrafast electron transfer previously observed by transient absorption spectroscopy. We found that $Fe^{III}TPP$ is chemically reduced to $Fe^{II}TPP$ in the presence of CIS QDs, but most likely occurs due to the presence of excess MPO thiols in solution rather than any specific QD interaction. We observed no change in T_2 decay of ^1H NMR signals associated with FeTPP in the presence of QDs relative to FeTPP alone, suggesting that FeTPP does not adsorb to QDs. We did find that T_2 decay for the diamagnetic analog ZnTPP does appear to have a shorter time component, suggesting that some fraction of ZnTPP molecules are bound to CIS QDs. It is possible that we were unable to make this observation for FeTPP due to the paramagnetic effects of the iron center. Finally, electrochemical XANES suggests that the iron center may be perturbed in the presence of QDs. Further work is needed to better understand this system.

3.5. Experimental Details

3.5.1 Quantum dot synthesis

Zinc sulfide shelled copper indium sulfide quantum dots ($CuInS_2@ZnS$ QDs or CIS QDs) were synthesized via an existing literature procedure.[46]

3.5.2 FeTPP and [FeTPP]$_2$O

Iron(tetraphenylporphyrinato) chloride (FeTPPCl) was purchased from Sigma Aldrich and used as received. The μ-oxo dimer [FeTPP]$_2$O was synthesized using existing procedures.[59]

3.5.3   Ground-state absorption spectroscopy

All ground state UV-vis absorption spectra were acquired using a Cary 5000 spectrometer. Samples were prepared in DMF or DMSO in a 0.2 mm quartz cuvette. Background correction was performed with blank solvent samples before sample spectra collection.

3.5.4   NMR spectroscopy

^{1}H NMR spectra were collected in deuterated dimethyl sulfoxide (DMSO-d_6) on a Bruker Avance HD III 500 MHz spectrometer. T_2 relaxation measurements were performed using the Carr-Purcell-Meiboom-Gill (CPMG) pulse sequence. 16 scans per spectrum were collected. The relaxation delay was 5 s. The 90° pulse length (pw90) was 10 µs and the 180° pulse length (pw180) was 20 µs. The echo time t was 0.1 ms. The evolution time was given by this expression: ($2t$ + pw180) × (# of echo loops).

3.5.5   In-situ electrochemical X-ray absorption near edge spectroscopy

A description of this experiment can be found in the dissertation of our collaborator Jiyun Hong (Chen Lab, Northwestern), who was instrumental in completing these experiments.

3.5.6   Cyclic voltammetry

Cyclic voltammetry was performed using a Princeton Applied Instruments VERSASTAT 3 potentiostat. All samples were dissolved in anhydrous DMF or DMSO with 100 mM tetrabutylammonium hexafluorophosphate (TBAPF$_6$) supporting electrolyte and degassed with N$_2$ or CO$_2$ before measurement. A three-electrode setup was used, with glassy carbon as the working electrode, a platinum wire as the counter electrode, and a silver wire as a pseudoreference electrode. The voltammograms were internally referenced to ferrocene, which was dissolved in the analyte solutions, and then referenced to SCE based on the potential of the ferrocene couple.

Chapter 4 : Towards a QD Triplet-Triplet Energy Transfer-Mediated aza Paterno-Buchi Reaction

4.1. Chapter Summary

This chapter describes work towards the development of an aza Paterno-Buchi reaction facilitated by triplet-triplet energy transfer from QDs to olefin and/or imine substrates. Triplet-triplet energy transfer in QDs and the definition of and motivation for the aza Paterno-Buchi reaction is discussed. In the work presented, QDs were unable to catalyze this reaction due to unproductive isomerization of at least one of the imines substrates used. Reasons for lack of aza Paterno-Buchi reactivity are discussed and the investigation of alternative imine substrates is reported.

4.2. Introduction

4.2.1 Triplet-triplet energy transfer photocatalysis in QDs

Triplet-triplet energy transfer (TT-EnT) from photoexcited QDs to organic substrates was first observed by Castellano *et al.* in 2016, when the researchers demonstrated that CdSe QDs could sensitize the triplet state of a pyrene dye bound to the QD surface via a carboxylate.[65] The heavy metal cadmium atoms within the QD structure allow for spin-orbit coupling in the excited state, resulting in a conduction band with triplet-like character that can sensitize the dark triplet state of pyrene, as observed by transient absorption spectroscopy. Since then, various groups have studied this phenomenon in greater detail and with various types of QDs.[66-68] Recently, the Weiss lab reported the use of CdSe QDs in sensitizing the triplet states of olefins to drive the formation of cyclobutanes via [2+2] cycloaddition.[69] As with TT-EnT from QDs to previously reported triplet acceptors, it was found that for TT-EnT to occur the olefin substrates required a suitable functional group, carboxylates in this case, to bind to QD surfaces. The use of these binding groups also enabled the sensitized [2+2] cycloaddition to occur with high regio- and diastereoselectivity, as substrates were aligned in a specific manner on QD surfaces. This preorganization of substrates

on QD surfaces has potential application in a myriad of other TT-EnT-driven organic reactions, which have been extensively studied in recent years.[7]

4.2.2 Challenges in realizing an aza Paterno-Buchi reaction

Azetidines are four-membered rings containing a nitrogen atom, and are found in many pharmaceutical target molecules.[70] However, synthesis of these rings by traditional chemical methods is challenging, typically involving harsh conditions and limited substrate scope.[71] Significant efforts have been made to synthesize azetidines by photochemical methods, namely by an aza Paterno-Buchi reaction. The Paterno-Buchi reaction is the [2+2] photocycloaddition of an olefin to a carbonyl, forming an oxetane, a four-membered ring containing an oxygen atom. The reaction can
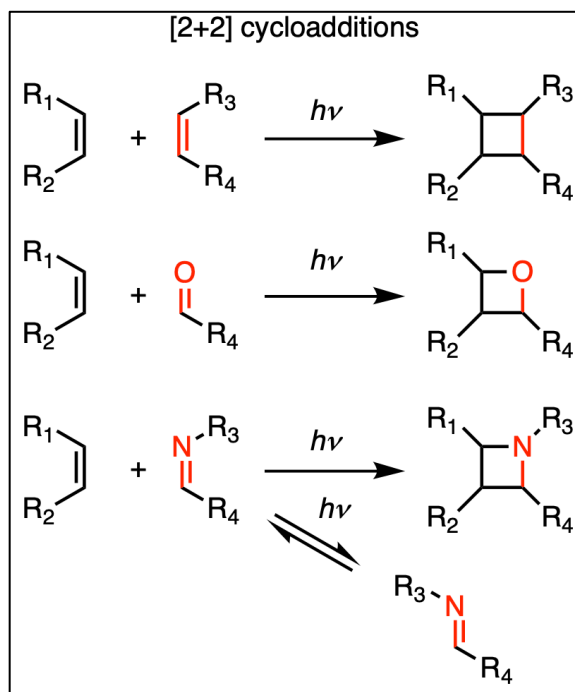
Scheme 4.1. Reaction schemes for olefin-olefin [2+2] photocycloaddition (top), Paterno-Buchi reaction (middle), and aza Paterno-Buchi reaction, with unproductive imine isomerization (bottom).

proceed either by direct excitation of the carbonyl or sensitization by an external chromophore.[72] An aza Paterno-Buchi reaction is the analogous reaction with an imine rather than a carbonyl, leading to an azetidine, as outlined in Scheme 4.1. Unfortunately, direct excitation or sensitization of imines generally leads to rapid isomerization about the C=N bond, dissipating the excited state energy and leading to little or no cycloaddition to olefins.[73-74] As a result, substrate scope has generally been restricted to cyclic imines, in which C=N bond rotation cannot occur,[75-76] or

intramolecular systems in which the olefin and imine are brought into close contact by covalent linkage to each other.[77-78]

4.2.3 Motivation for use of QDs in aza Paterno-Buchi reaction

The general motivation for utilizing QDs in an aza Paterno-Buchi reaction is twofold. First, if the substrates have functional groups that can bind to QD surfaces, they can be brought into close contact on QD surfaces in order to increase the likelihood of cycloaddition between them. Nonproductive relaxation via rapid isomerization might be minimized if bringing substrates into close proximity enables cycloaddition to occur on a faster timescale than isomerization. Second, the tunable nature of QDs could allow for selective sensitization of only olefins, leaving imines in the ground state and unable to undergo unproductive isomerization. As shown previously by the Weiss lab, the triplet energy of QDs can be tuned (by changing the size of the QD nanocrystals) such that lower substrates are selectively excited in the presence of higher energy substrates.[69] While the triplet energies of the imines used in this study were not initially known, similar imines were found to have higher triplet energies than those of the olefins used, suggesting that the olefins could be selectively excited with QDs. Another benefit of the proposed approach is the diastereo-

and regioselectivity that could be imposed by substrate binding, as seen in the QD olefin [2+2] system. A summary of the proposed system is shown in Scheme 4.2.
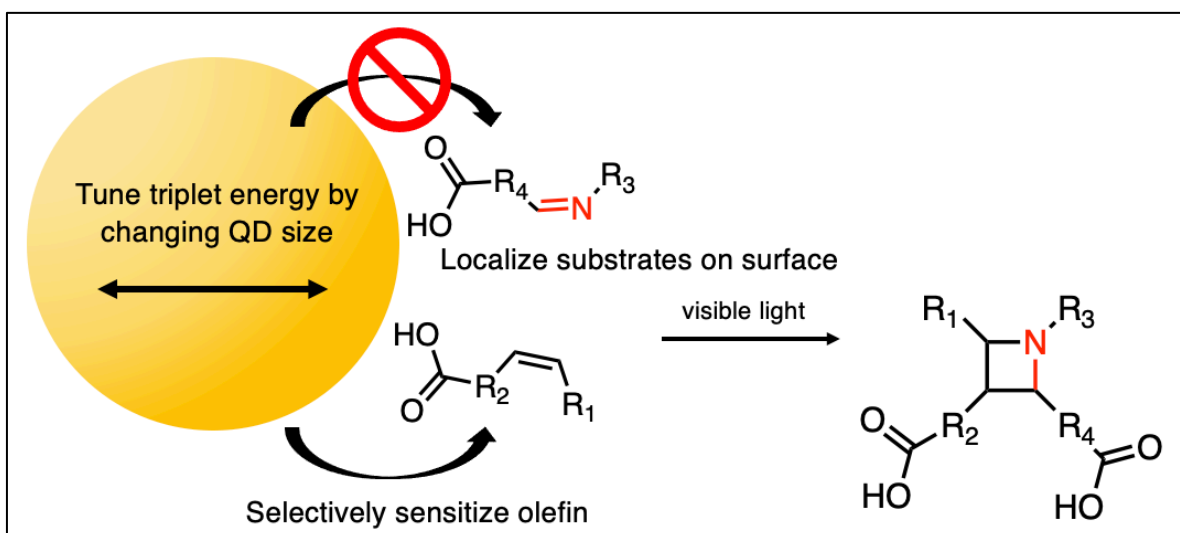
Scheme 4.2. Proposed scheme for a QD TT-EnT-mediated aza Paterno-Buchi reaction.

4.3. Results and Discussion

4.3.1 Initial studies with oxime 1
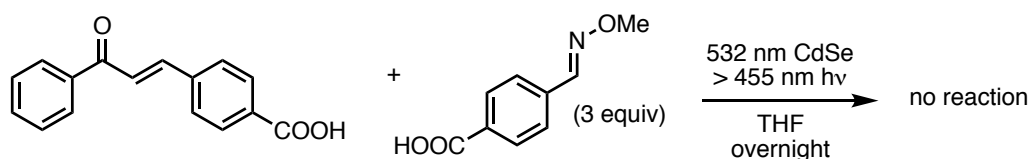
Figure 4.1. Initial reaction conditions for QD-sensitized aza Paterno-Buchi reaction between olefin **C1** and oxime **1**.

For initial attempts at an aza Paterno-Buchi reaction facilitated by QDs, an oxime derived from 4-formylbenzoic acid, 4-[(methoxyimino)methyl]benzoic acid, hereafter referred to as oxime **1**, was prepared for use as the imine substrate. Oximes are generally more stable than imines, particularly when exposed to water, and also undergo less thermal isomerization, which could obfuscate any photochemical isomerization that occurs. They have been successfully used in previous studies on aza Paterno-Buchi reactions.[78] The initial reaction scheme is shown in Figure 4.1. CdSe QDs with a 532 nm first excitonic peak were used as their emission energy is high enough to sensitize the chalcone olefin (**C1**) used but lower than the triplet energy we expected for

oximes such as **1**. The reaction was performed under air-free conditions to prevent undesired sensitization of triplet oxygen. No reaction was observed between oxime **1** and the sensitized olefin substrate **C1**. Some homocoupling between **C1** substrates was observed, indicating successful sensitization of the olefin, but no other products were observed. Similar reactivity was observed when altering a number of factors, including QD size (larger or smaller QDs leading to lower or higher triplet energy, respectively), stoichiometry of substrates, solvent (4:1 toluene:THF), and different QDs (core@shell CdSe@ZnS, CdSe@CdS, or $CuInS_2$@ZnS QDs).

4.3.2   QDs sensitize triplet state of 4-[(methyoxyimino)methyl]benzoic acid
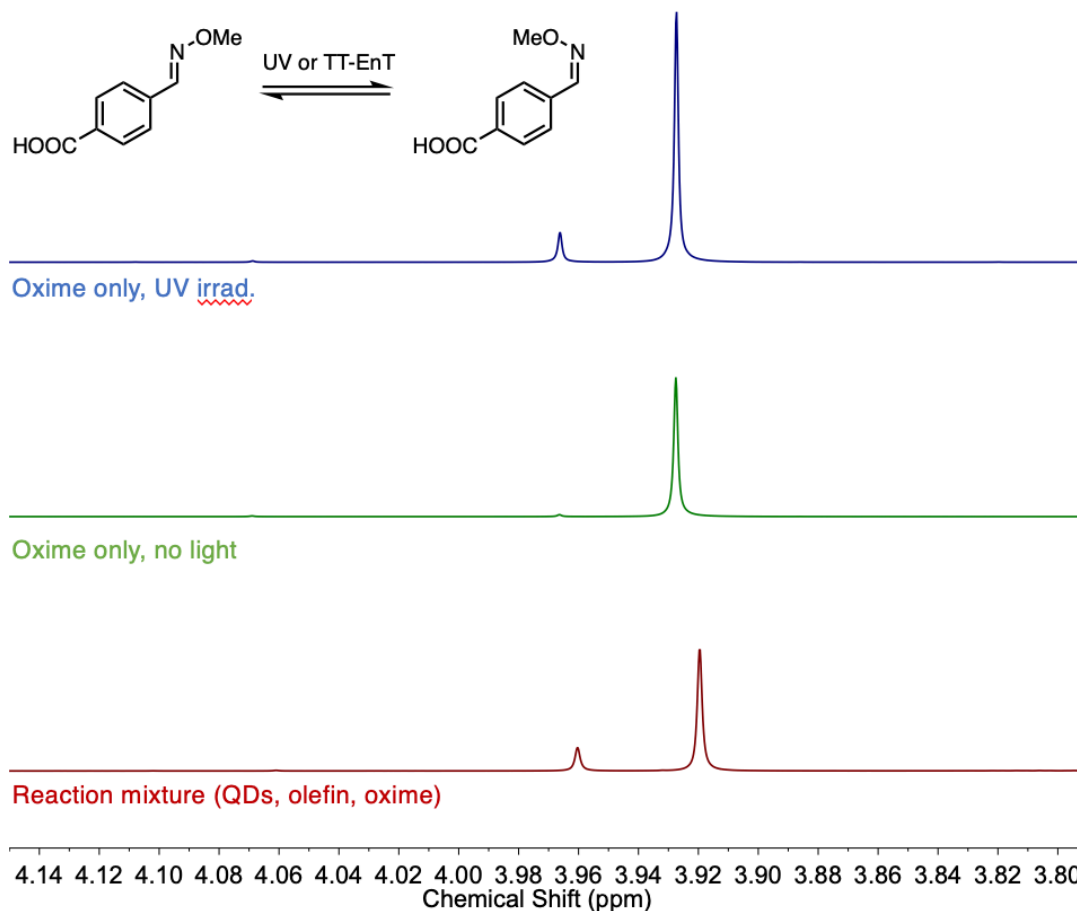
Figure 4.2. ^{1}H NMR spectra of oxime **1** after UV irradiation (top, blue), no irradiation (middle, green), and with after irradiation with visible light in reaction mixture described in Figure 4.3 (QDs and olefin).

Closer examination of the ^{1}H NMR spectra of crude reaction mixtures revealed that oxime **1** was isomerizing over the course of the reaction, likely due to sensitization by QDs, as revealed in Figure 4.2, which shows the methoxy resonance of oxime **1** in the *E* (favored) or *Z* conformation. This result suggested that the triplet state of oxime **1** was not as high in energy as we initially thought. To experimentally measure the triplet energy of oxime **1**, we measured its phosphorescence in 2-methyltetrahydrofuran at 77 K. The resulting spectrum is shown in Figure 4.3. While the phosphorescence peaks are located around 450 nm, a large shoulder exists that overlaps with the photoluminescence of the QDs used, the peak position of which is marked by the red line in the figure. This indicates that QDs could in fact sensitize this particular oxime. We

then synthesized larger CdSe QDs, with first excitonic peak at 576 nm, which should have excited state energies that are too low for TT-EnT to oxime **1**. However, as shown in Figure 4.4, oxime **1** still isomerizes when present both with olefin **C1** and QDs (the entire reaction mixture, top spectrum) and with QDs only (bottom spectrum). The larger extent of
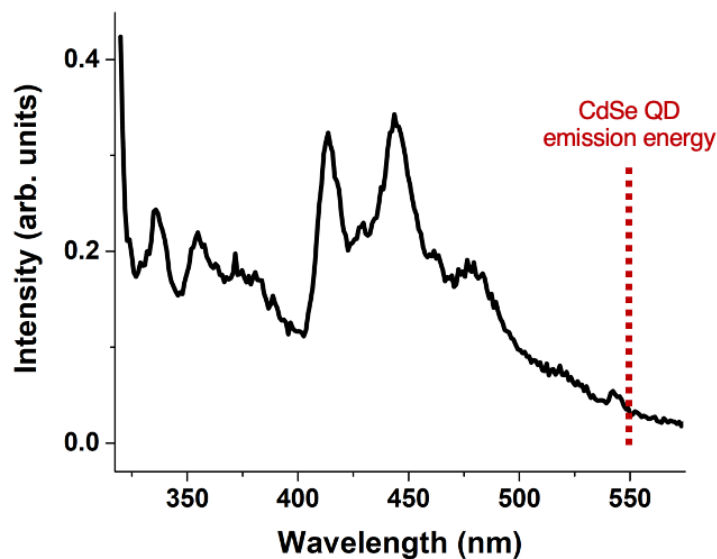
Figure 4.3. Phosphorescence spectrum of oxime **1** taken at 77 K in 2-methyltetrahydrofuran.

isomerization is likely due to the longer reaction time relative to Figure 4.2, so the results are not
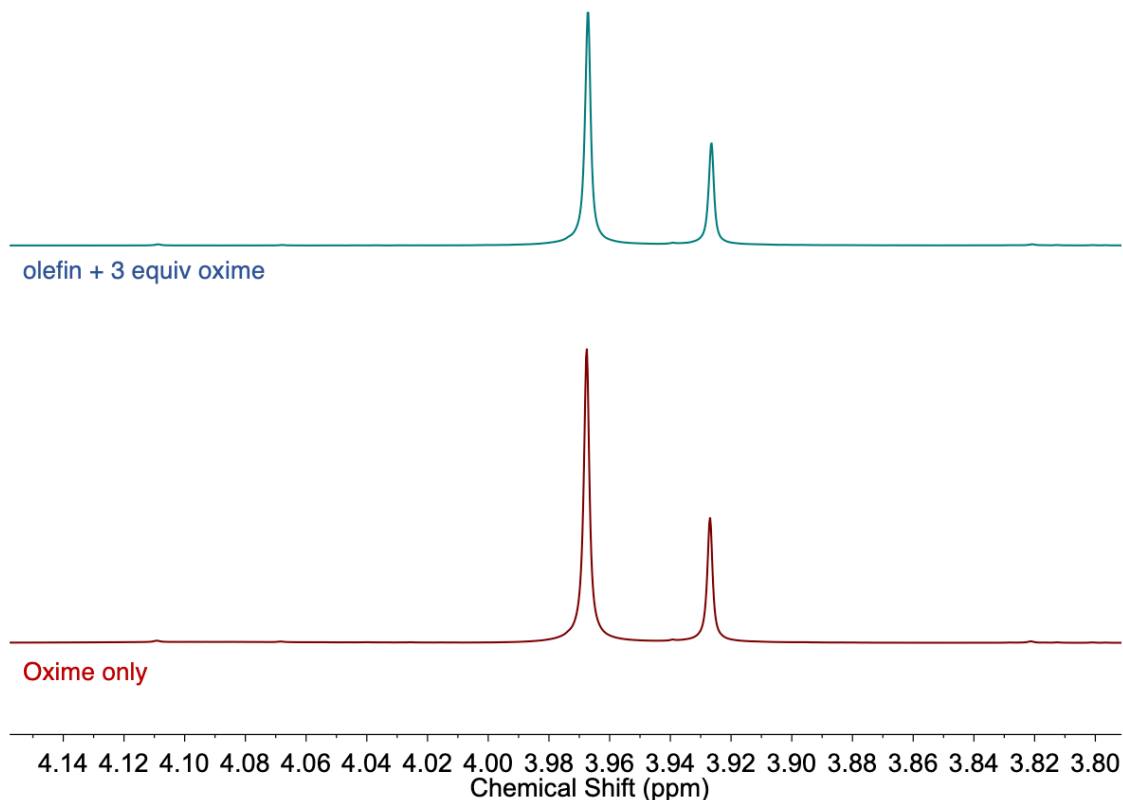
Figure 4.4. ^{1}H NMR spectra of oxime **1** after 3.5 days of visible light irradiation in presence of 576 nm CdSe QDs only (red, bottom) and QDs and olefin **C1** (blue, top).

comparable in that respect, but nevertheless indicate that QDs with photoluminescence energy below the observed phosphorescence energy of oxime **1** are still able to sensitize isomerization of the oxime. A review of the literature found that similar oximes exhibited this behavior through a mechanism called non-vertical energy transfer, in which thermal motion of the oxime can couple to the energy transfer process in order to decrease the effective energy needed for triplet sensitization.[79] We attempted to remove this thermal component by illuminating mixtures of QDs and oxime **1** at low temperature, as shown in Figure 4.5, but isomerization continued to occur, even at -78 °C.
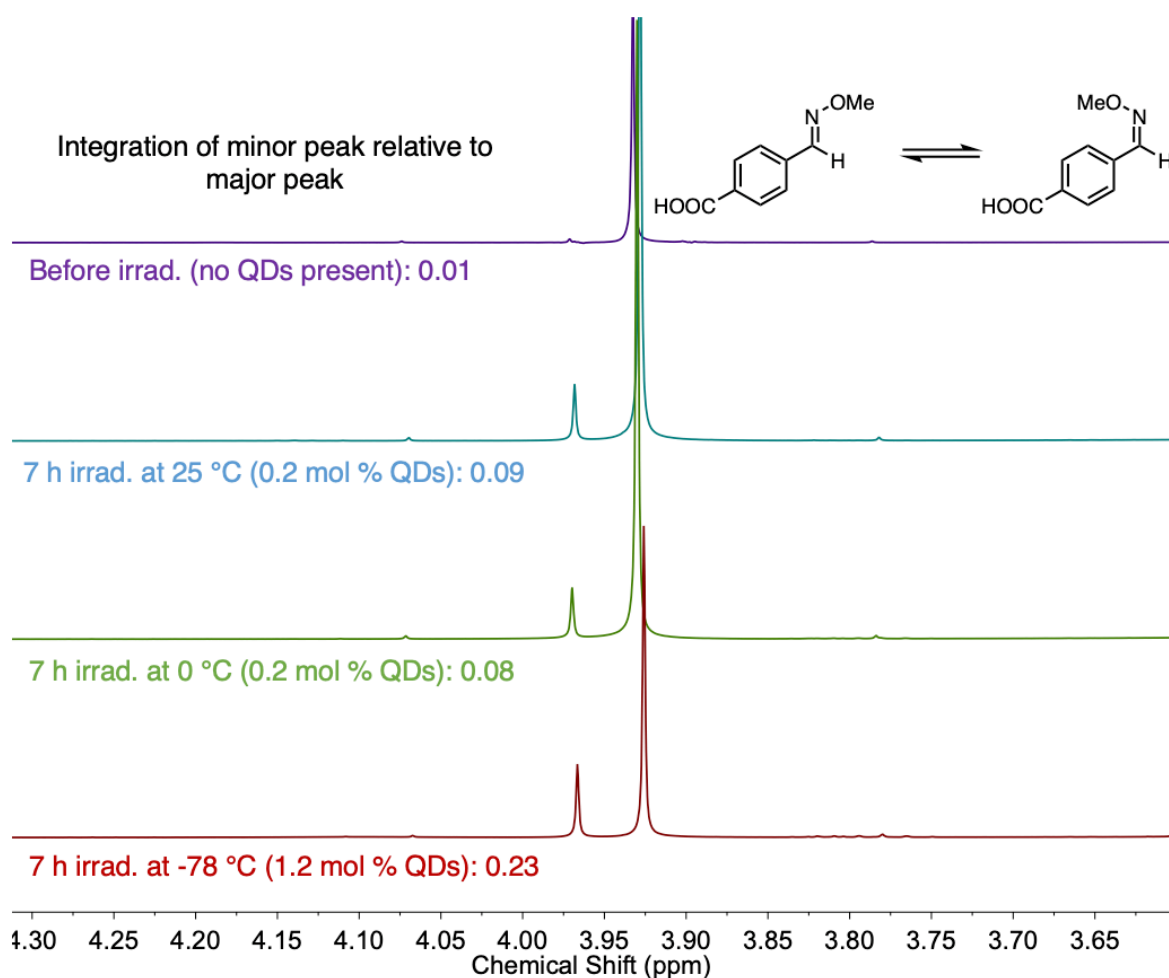
Figure 4.5. ^{1}H NMR spectra of (from top to bottom) oxime **1** alone before irradiation (purple) and with CdSe QDs after 7 h irradiation at 25 °C (blue), at 0 °C (green), and at -78 °C (red, more QDs used). The inset text gives the integration of the minor isomer peak relative to an integration of 1 for the major peak.

4.3.3   Selective sensitization of oxime substrate

After establishing that QDs sensitize the triplet state of oxime **1**, we attempted to sensitize

oxime **1** selectively by choosing an olefin substrate with triplet energy greater than that of QDs.
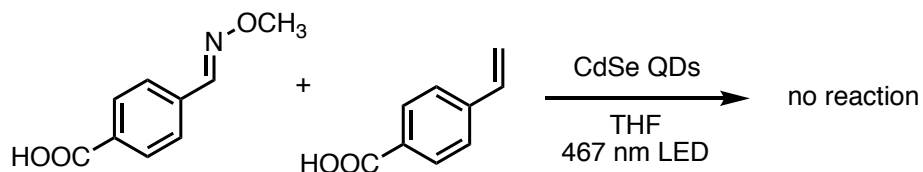
Figure 4.6. Reaction conditions for QD-sensitized aza Paterno-Buchi reaction between oxime **1** and olefin **C2**.

Despite the clear occurrence of isomerization in the oxime, we thought it possible that localizing

the sensitized oxime near a non-sensitized olefin on the QD surface could enable some [2+2]

cycloaddition to occur as well. The reaction scheme, using 4-vinylbenzoic acid (**C2**) as the olefin

substrate, is shown in Figure 4.6. Unfortunately, no reaction was observed. We used ^{1}H NMR

spectroscopy to examine the effect of varying the ratio between oxime **1** and olefin **C2** on the

isomerization of oxime **1**, as shown in Figure 4.7. With no olefin present, the oxime isomerizes to

nearly 1:1 *E:Z* under these conditions, after starting at ~99:1 *E:Z*. However, adding any amount of

olefin **C2** greatly decreases the extent of isomerization. Even 5:1 oxime:olefin, in which only 16%
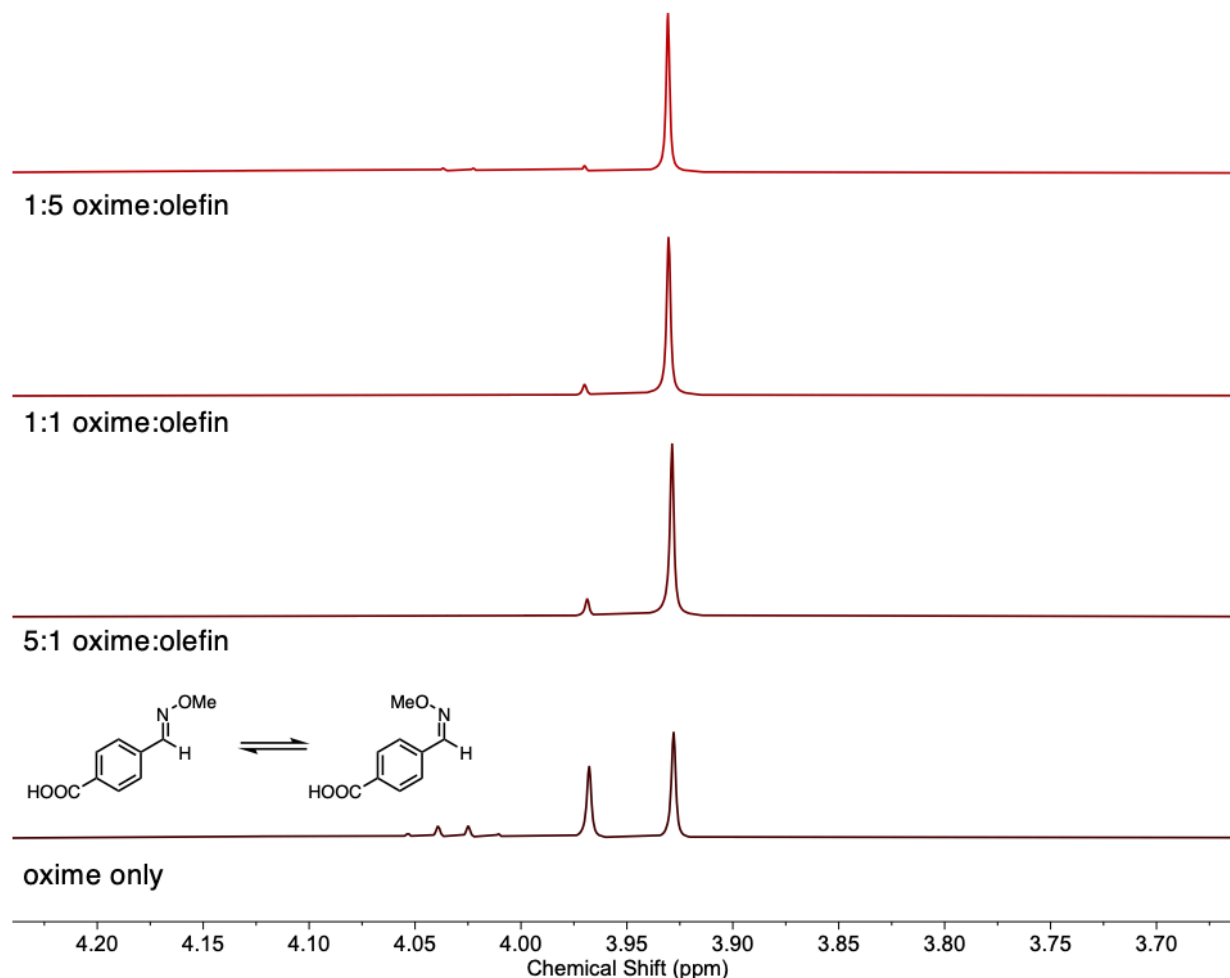
Figure 4.7. ^{1}H NMR spectra of reaction mixtures containing CdSe QDs and oxime **1** alone (bottom) and with 0.2, 1, or 5 equiv olefin **C2** after 2 h irradiation with 467 nm LED.

of the substrates in solution are olefin, isomerization decreases quite significantly. There are at least two possible explanations for this behavior. The first, and more likely, is that olefin **C2** has a greater affinity for the QD surface than oxime **1** and therefore preferentially binds to the QD surface, crowding out the oxime and decreasing TT-EnT to the oxime and subsequent isomerization. To confirm this hypothesis, a detailed ^{1}H NMR spectroscopic binding study could be performed to measure the relative binding strengths of each substrate.[80] The second possibility is that the first step of [2+2] cycloaddition is occurring, but the reaction is unable to go to completion due to instability of the 1,4-biradical intermediate, which may contain a primary alkyl

radical, as illustrated in Figure 4.8. However, in this case more isomerization of the oxime would likely be observed, as C-N bond rotation can occur in the intermediate species, as has been previously observed.[78]
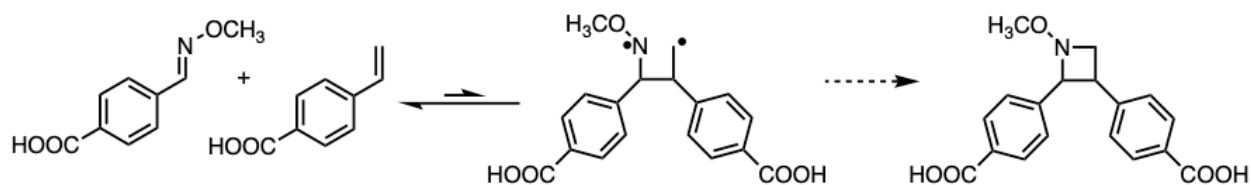
Figure 4.8. Possible reaction mechanism for reversible formation of 1,4-biradical between oxime **1** and olefin **C2**.

4.3.4 Other imine and oxime substrates attempted

A number of alternate imine and oxime substrates were explored for potential [2+2] cycloaddition with a sensitized chalcone olefin, as shown in Figure 4.9. Phenylimines with the carboxylate both on the aldehyde-derived side of the molecule (**2**) and the aniline-derived side (**3**) were tested, as previous work indicated that the position of the binding group could potentially affect sensitization by QDs.[69] No reaction was observed with either substrate, possibly due to effective sensitization and isomerization of the imine. Photosensitized isomerization cannot be
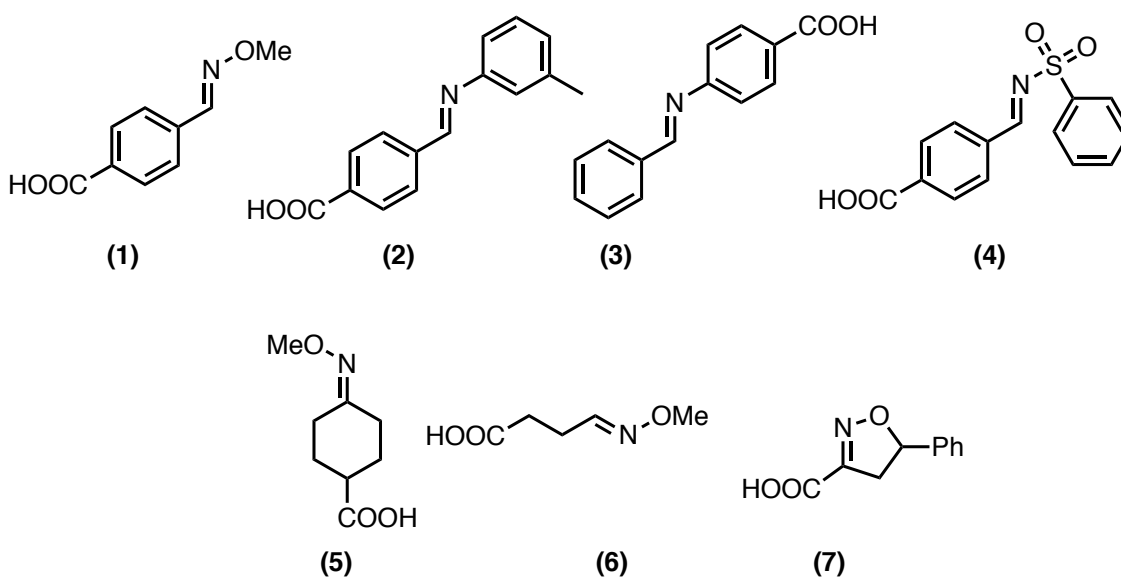
Figure 4.9. Oxime and imine substrates synthesized for use in QD-mediated aza Paterno-Buchi reaction.

easily tracked with imines because thermal isomerization also occurs.[74] The reaction was also attempted with sulfonyl imine **4**, as an analogous imine had previously been used in a rare and limited example of an intermolecular photosensitized [2+2] cycloaddition between olefins and imines.[81] However, the success of the cited reaction was thought to be due to exiplex formation, which is unlikely to occur in our system, and we only observed complex side products.

Alkyl and cyclic oximes **5**, **6**, and **7** were also explored for this reaction, as shown in Figure 4.9. Due to the lack of π conjugation, alkyl oximes should have considerably higher triplet energies than their aromatic counterparts, and thus should not be sensitized by QDs. However, using the
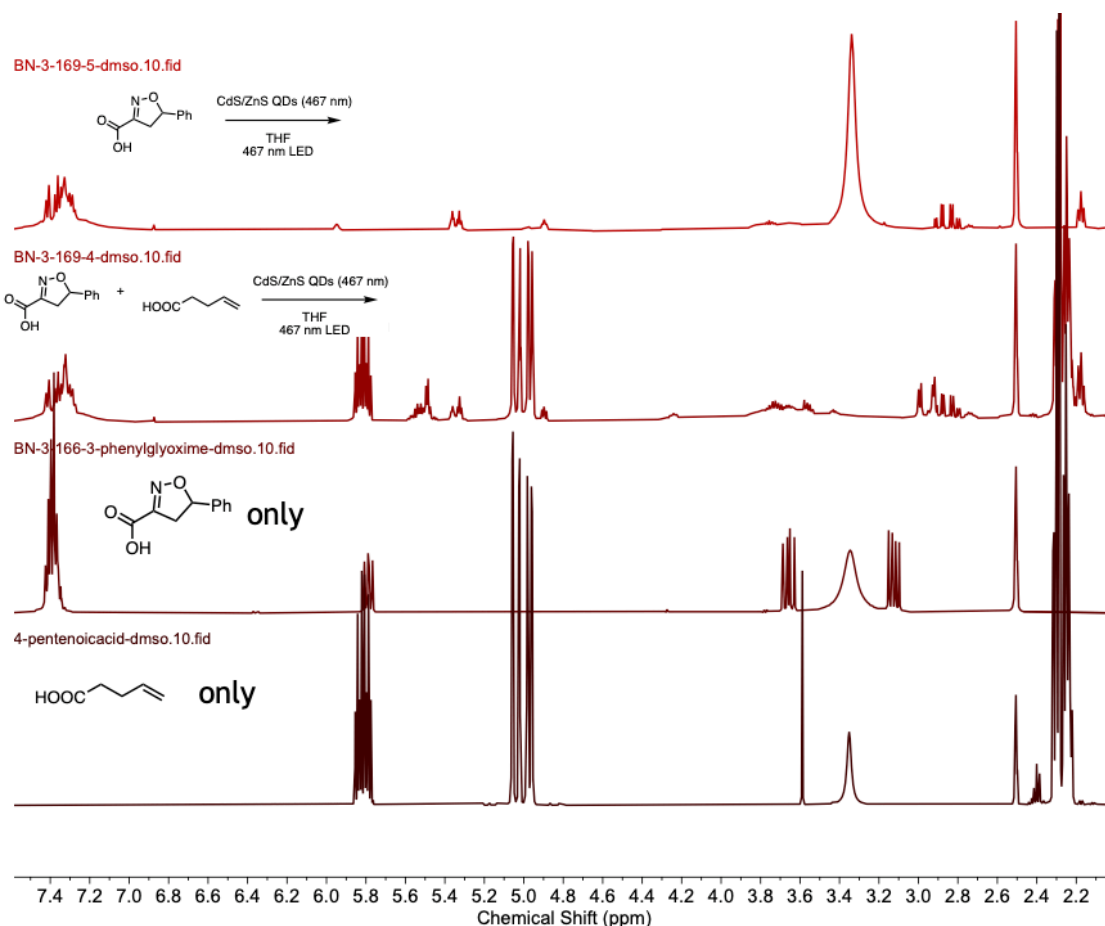
Figure 4.10. ^{1}H NMR spectra of oxime **6** and 4-pentenoic acid alone (bottom two spectra) and spectra of reaction mixtures of CdS@ZnS QDs and oxime **6** (top) and QDs, oxime **6**, and 4-pentenoic acid (second from top) after overnight irradiation with 467 nm LED.

reaction conditions shown in Figure 4.1, in which the olefin **C1** is selectively excited by QDs, no

reaction occurred using oximes **5** or **6**. We then moved to the cyclic 2-isoxazoline-3-carboxylate oxime **7**, as this scaffold was recently used by the Schindler group in a successful intermolecular aza Paterno-Buchi reaction mediated by iridium photocatalysts.[76] However, Schindler *et al.* only used the ethyl ester version of oxime **7**, while we wished to use the free acid in order to bind the substrate to QDs. As shown in Figure 4.10, this oxime exhibits some reactivity with QDs in the absence of any other substrates. CdS@ZnS QDs were used in this reaction, as higher energy QDs were needed to sensitize this oxime.[76] In the presence of 4-pentenoic acid, an olefin that is not sensitized by QDs, additional reactivity appears to take place, but the desired [2+2] product could not be isolated by LC-MS. The Schindler group also reports "complex reactivity" between the free acid oxime and iridium photocatalysts. More work is required to understand the reactivity that is occurring in this system. In addition, it is clear from the scattered literature reports on aza Paterno-Buchi reactions that more detailed mechanistic studies could be valuable in gaining a deeper understanding of the observed limitations in substrate scope.

4.4.   Conclusions

Due to strong spin-orbit coupling, the excited states of QDs exhibit some triplet-like character that can be harnessed in mediating photochemical reactions via TT-EnT. This work attempted to harness QD-mediated TT-EnT to perform an aza Paterno-Buchi reaction, in which a [2+2] cycloaddition between an olefin and an imine or oxime forms an azetidine. Non-vertical energy transfer in oximes made selective sensitization of olefins challenging and allowed the nonproductive isomerization energy relaxation pathway of oximes to dominate. Nonaromatic substrates, while likely not sensitized by QDs, proved to be unreactive with sensitized olefins at QD surfaces. 2-isoxazoline-3-carboxylate oximes may be promising candidates as their esters have been successfully used in aza Paterno-Buchi reactions,[76] but substrates may need to be designed

with binding groups in different positions, as a free acid in the 3-position of the cyclic oxime appears to impart some complex reactivity. Other methods of binding imines or oximes to QD surfaces, such as hydrogen bonding,[82] could also be explored.

4.5.   Experimental Details

4.5.1   QD synthesis

CdSe QDs were synthesized via a previously reported heterogeneous method.[69, 83] CdSe@ZnS and CdSe@CdS core@shell QDs were synthesized in two steps. CdSe cores were synthesized via a homogeneous method, then ZnS or CdS shelling was completed via previously reported SILAR methods.[28, 84] CdS@ZnS QDs were synthesized using a previously reported procedure.[85]

4.5.2   Substrate synthesis

Synthetic characterization

^{1}H NMR spectra were acquired in chloroform-d_3 or dimethylsulfoxide-d_6 using a Varian Inova 500 (500 MHz) or a Bruker AVANCE III HD (400 MHz).

4-[(methoxyimino)methyl]benzoic acid (1)

The compound was synthesized by adapting a literature procedure.[86] 4-formylbenzoic acid (1.0 equiv) was dissolved in EtOH and methoxylammonium chloride (3 equiv) was added. The mixture was stirred briefly, then a saturated aqueous solution of NaHCO$_3$ was added until the solution became neutral. The reaction was stirred at room temperature overnight, then CH$_2$Cl$_2$ was added to the flask. 1 M HCl was added to acidify the solution, and the solution was mixed in a separatory funnel and separated. The organic layer was washed with saturated NaCl and dried with MgSO$_4$, then dried under reduced pressure. The final product was obtained by recrystallization from EtOH. ^{1}H NMR (500 MHz, DMSO) δ 8.32 (s, 1H), 7.99 – 7.95 (d, 2H), 7.75 – 7.70 (d, 2H), 3.93 (s, 2H).

4-[[(3-methylphenyl)imino]methyl]benzoic acid (2)

The compound was synthesized by a literature procedure.[87] 4-formylbenzoic acid (1.0 equiv) was dissolved in EtOH, and 2-methylaniline (1.1 equiv) was added. The solution was heated to 60 °C overnight, then CH_2Cl_2 and 1 M HCl was added to the flask, and the solution was extracted. The organic layer was washed with saturated NaCl and dried with $MgSO_4$, then dried under reduced pressure. The product was recrystallized from hot toluene. ^1H NMR (500 MHz, $CDCl_3$) δ 8.54 (s, 1H), 8.25 – 8.19 (m, 2H), 8.04 – 7.97 (m, 2H), 7.31 (t, J = 7.6 Hz, 1H), 7.13 – 7.03 (m, 3H), 2.41 (s, 3H).

4-[(phenylmethylene)amino]benzoic acid (3)

The compound was synthesized by a literature procedure.[88] 4-aminobenzoic acid (2.74 g, 1 equiv), benzaldehyde (2.13 g, 1.01 equiv), and glacial acetic acid (2 drops) were dissolved in 150 mL toluene and refluxed for 4 hours. After cooling to room temperature, a white solid formed and was collected by filtration, washed with toluene, and recrystallized from methanol to obtain the product. ^1H NMR (500 MHz, DMSO) δ 12.87 (s, 1H), 8.65 (s, 1H), 8.02 – 7.93 (m, 4H), 7.62 – 7.51 (m, 3H), 7.36 – 7.29 (m, 2H).

4-[[(phenylsulfonyl)imino]methyl]benzoic acid (4)

The compound was synthesized by an adapted literature procedure.[81] 4-formylbenzoic acid (330 mg, 1.0 equiv) and benzenesulfonamide (157 mg, 1.0 equiv) were dissolved in 10 mL anhydrous toluene over molecular sieves. A few drops of p-toluenesulfonic acid were added, and the solution was refluxed overnight. The resulting pink opaque mixture was brought to room temperature and filtered to yield a light pink solid. ^1H NMR (500 MHz, DMSO) δ 9.26 (s, 1H), 8.18 – 8.11 (m, 2H), 8.11 – 8.05 (m, 2H), 8.04 – 7.97 (m, 2H), 7.82 – 7.75 (m, 1H), 7.72 – 7.65 (m, 2H).

4-(methyoxyimino)cyclohexanecarboxylic acid (5)

The compound was synthesized by a method similar to that of compound **1**. 4-oxocyclohexanecarboxylic acid (73 mg, 1.0 equiv) and methoxylammonium chloride (73 mg, 1.5 equiv) were dissolved in 5 mL MeOH, then 140 µL pyridine (3.0 equiv) was added, and the solution was stirred overnight. The solution was then acidified and extracted with EtOAc. The organic layer was washed with saturated NaCl, dried with MgSO$_4$, and concentrated under reduced pressure. ^{1}H NMR (500 MHz, CDCl$_3$) δ 3.82 (s, 3H), 3.11 – 3.02 (m, 1H), 2.60 (m, 1H), 2.49 – 2.40 (m, 1H), 2.17 – 1.99 (m, 4H), 1.86 – 1.64 (m, 2H).

4-(methyloximino)butanoic acid (6)

The compound was synthesized in two steps using literature procedures. In the first step,[89] succinic semialdehyde was prepared by the following procedure. *L*-glutamic acid potassium salt monohydrate (500 mg, 1 equiv) was dissolved in 15 mL H$_2$O and heated to 37 °C, then 6 wt % NaOCl in H$_2$O (2.75 mL, 2.46 mmol, 1.0 equiv) was added dropwise. The solution was stirred at 37 °C for 1 hour, then 1 M HCl (2.75 mL) was added and the solution was stirred until effervescence stopped. The solution was cooled to room temperature, saturated NaCl was added, and the solution was extracted with diethyl ether (3 × 20 mL). The organic portions were combined, dried with MgSO$_4$ and concentrated under reduced pressure. The product was then immediately dissolved in methanol and treated with methoxylammonium chloride (3 equiv, based on 100% yield of product) and pyridine (1 equiv relative to methoxylammonium chloride) and stirred overnight. H$_2$O was added and the product was extracted with ethyl acetate. The organic layer was washed with saturated NaCl, dried with MgSO$_4$ and concentrated under reduced pressure to provide a mixture of isomers. NMR spectroscopic data for major isomer given. ^{1}H NMR (500 MHz, CDCl$_3$) δ 7.43 (t, 1H), 3.82 (s, 3H), 2.63 – 2.56 (m, 4H).

5-phenyl-4,5-dihydroisoxazole-3-carboxylic acid (7)

The compound was synthesized by literature procedures in three steps.[90] First, ethyl chlorooximidoacetate (CEFNO) was prepared. Glycine ester hydrochloride (69.7 g, 0.5 mol) was dissolved in 95 mL H_2O, 41.5 mL of concentrated HCl was added, and the mixture was cooled to -5 °C. A solution of 1 equiv of sodium nitrite in 50 mL H_2O was added dropwise, followed by a second equivalent of conc. HCl and a second equivalent of sodium nitrite, added in the same manner. The mixture was extracted with diethyl ether, dried with $MgSO_4$ and concentrated under reduced pressure. The product was obtained by recrystallization from hexanes. The ^1H NMR spectrum matched the reported spectrum. CEFNO (1.16 g, 7.6 mmol) and styrene (0.87 mL, 7.6 mmol, 1 equiv) were dissolved in 17 mL diethyl ether, and a solution of TEA (1.06 mL, 7.6 mmol) in 10 mL diethyl ether was added dropwise over a ~30 minute period. The solution was stirred overnight, then washed with water, dried with $MgSO_4$ and concentrated under reduced pressure. The ethyl ester product was obtained in good purity and immediately treated with 10% NaOH in an EtOH/H_2O solution to cleave the ester and provide the title compound. ^1H NMR (500 MHz, DMSO) δ 7.49 – 7.31 (m, 5H), 5.79 (dd, J = 11.4, 9.1 Hz, 1H), 3.66 (dd, J = 17.7, 11.4 Hz, 1H), 3.12 (dd, J = 17.7, 9.1 Hz, 1H).

*(E)-4-(3-oxo-3-phenylprop-1-en-1-yl)benzoic acid (**C1**)*

The compound was synthesized by a literature procedure.[69] Acetophenone (500 mg, 1.0 equiv) and 4-formylbenzoic acid (625 mg, 1.0 equiv) were dissolved in 20 mL EtOH. KOH (700 mg, 3.0 equiv) was dissolved in 1.6 mL H_2O and added to the reaction mixture, which was stirred for 12 h at room temperature. The solution was then acidified to pH 2 using 1 M HCl. The precipitate was collected by filtration and recrystallized from EtOH to provide the title compound. ^1H NMR (500 MHz, DMSO) δ 13.13 (s, 1H), 8.22 – 8.16 (m, 2H), 8.06 (d, J = 15.7 Hz, 1H), 8.04 – 7.98 (m, 4H), 7.79 (d, J = 15.7 Hz, 1H), 7.73 – 7.66 (m, 1H), 7.60 (t, J = 7.7 Hz, 2H).

4.5.3   General procedure for photocatalytic reaction setup

In a 4-mL vial, the appropriate volume of QD stock solution was dried under reduced pressure, and a stir bar was added. If the substrate was a solid, the appropriate volume of a stock solution of the substrate was added to a separate vial and dried under reduced pressure. If the substrate was a liquid, it was added to a vial with a septum and degassed with nitrogen for 20 minutes. QD and substrate vials were both then brought into a nitrogen glovebox, where a total of 1 mL of non-stabilized tetrahydrofuran was used to dissolve and mix QD and substrates. The vial was sealed with a septum cap, removed from the glovebox, and irradiated with a CFC white light bulb or 467 nm LED (Kessil) while stirring.

4.5.4   General procedure for reaction workup

When irradiation was stopped, the reaction mixture was transferred to a centrifuge tube, 9 mL of methanol was added, and the mixture was centrifuged for 5-10 minutes at 7500 rpm to separate QDs from the reaction mixture. The supernatant was dried under reduced pressure and redissolved in dimethylsulfoxide-d_3 for ^{1}H NMR spectroscopic analysis.

Chapter 5 : Conclusions

5.1. Dissertation Summary

This dissertation explored the use of both organic and semiconductor nanocrystal chromophores as photosensitizers or photocatalysts in light-driven reactions. Chapter 1 introduced the motivation for studying light-driven processes and briefly discussed the basic chemistry behind them. Supramolecular chemistry was introduced as one method to potentially improve the performance of photocatalytic systems.

In Chapter 2 the synthesis of a series of amphiphilic *N*-annulated perylene chromophores and their self-assembly in aqueous solution was presented. A modular synthesis enabled easy synthesis of *N*-annulated perylenes with water-solubilizing carboxylate tails with 1 to 7 methylene spacers between the carboxylate and perylene. These molecules generally self-assembled into extended ribbon-like nanostructures in aqueous solution. This self-assembly resulted in weak electronic coupling between the perylene monomers, as evidenced by UV-vis spectroscopy. The self-assembled nanostructures were used to photosensitize a CO_2 reduction catalyst in fully aqueous conditions, leading to some photocatalytic reduction of CO_2 to CO. However, more work is needed to optimize the system and determine definitively whether or not photosensitization is occurring.

Chapter 3 discusses the investigation of possible binding interactions between CIS QDs and an iron porphyrin CO_2 reduction catalyst FeTPP. Solutions of CIS QDs, which were capped with MPO ligands for this study, were found to contain free MPO, which chemically reduced $Fe^{III}TPP$ to $Fe^{II}TPP$, as confirmed by UV-vis, ^1H NMR and X-ray absorption near edge spectroscopies. T_2 relaxation was used to probe whether or not FeTPP was bound to the surface of CIS QDs, but the paramagnetic nature of the FeTPP iron center precluded definitive conclusions.

The challenges and potential advantages of using QDs as TT-EnT mediators of an aza Paterno-Buchi reaction are discussed in Chapter 4. Imine substrates were sensitized by QDs but underwent

unproductive isomerization and could not undergo [2+2] cycloaddition with olefins, even when nominally co-localized on QD surfaces. Alternative imine substrates that allowed for selective sensitization of olefin only also did not lead to any cycloaddition products.

5.2.   Future Directions

5.2.1   Alternative water-solubilizing groups for N-annulated perylene chromophore amphiphiles

N-annulated perylenes could easily be functionalized with alkylammonium water-solubilizing groups instead of carboxylates, simply by replacing bromoalkanoates with bromoalkylammoniums in the substitution reaction shown in Figure 2.1. It is possible that this change could alter the extent of electronic coupling between the perylenes, though this seems unlikely as the electronics of the core itself will not be strongly perturbed. However, using alkylammonium solubilizing groups would ensure that the perylene amphiphiles are soluble at low pH, which should allow the chromophores to remain in solution when the pH is lowered by saturation with CO_2, as discussed in Section 2.3.3. This might increase photocatalytic activity significantly, as precipitated carboxylate perylene amphiphiles would not have been able to efficiently sensitize the dissolved catalyst. Additionally, a negatively-charged variant of the iron porphyrin catalyst (tetraphenylporphyrin with four sulfonyl groups appended to the phenyl rings) could be used to promote electrostatic attraction to the alkylammonium perylene assemblies.

5.2.2   Synthetic tuning of electronic structure of N-annulated perylene core

The *N*-annulated perylene amphiphiles synthesized in this study likely exhibit weak electronic coupling due to a quadrupole moment that encourages edge-to-face stacking, which prevents π orbital overlap.[91] The *N*-annulated core can be brominated at the 3 and 10 positions. Further functionalization from this starting point could tune the electronic structure of the *N*-annulated perylene such that face-to-face stacking might be preferred, leading to stronger electronic

coupling. DFT calculations could be performed to obtain electron density maps, which might help predict the most promising targets for synthesis, as larger dipole moments may encourage face-to-face stacking.

5.2.3   Covalent attachment of catalysts to chromophore amphiphile assemblies

Another future direction for improved application of chromophore amphiphile assemblies in photocatalytic applications is localization of a catalyst on the self-assembled nanostructure surface. While this was previously attempted using electrostatics,[34] the electrolyte concentration in solution was quite high due to the sodium ascorbate sacrificial electron donor, which may screen the
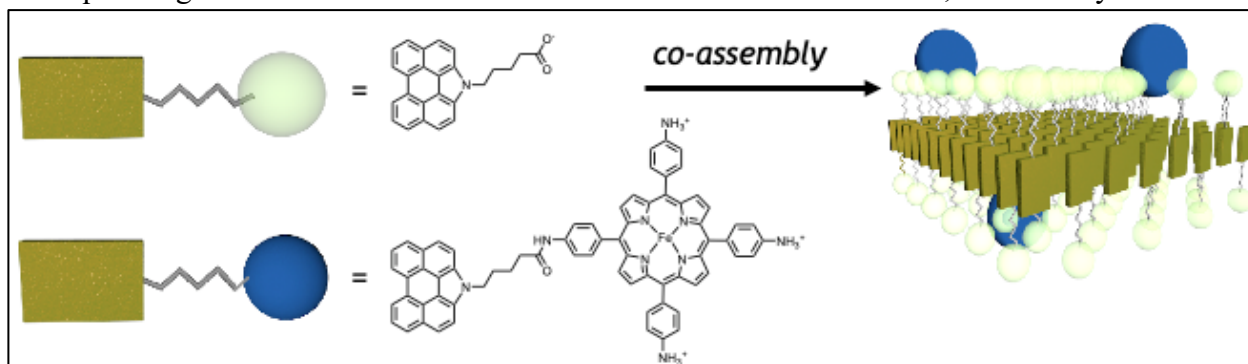
Scheme 5.1. Proposed co-assembly of chromophore amphiphile and chromophore-catalyst dyad amphiphile.

negatively charged amphiphile assemblies and prevent any specific binding of a positively charged catalyst. Instead, one could envision a co-assembly of chromophore amphiphiles with a chromophore-catalyst dyad, as depicted in Scheme 5.1. Covalent tethering would ensure that the catalyst remained close to the nanostructure surface. Linker length between chromophore and catalyst could be varied, as the optimal length is not necessarily obvious – on one hand, a shorter linkage keeps the catalyst close to the chromophore to which it is attached, but on the other hand, a longer flexible linkage could allow the catalyst to "reach over" to other chromophores within the assembly, which might result in more efficient charge transfer.

5.2.4   Continued study of porphyrin-QD conjugates by T_2 relaxation and transient absorption

As shown in Chapter 4, the T_2 relaxation time of ZnTPP may have been decreased in the presence of CIS QDs, which would suggest that ZnTPP is binding to QD surfaces via a nonspecific hydrophobic interaction. A number of additional experiments could be performed to build confidence in this assertion. First, transient absorption spectroscopy could be performed on the CIS QD/ZnTPP system, to see if ultrafast (<200 fs) ET from QDs to ZnTPP is observed as it was previously in the QD/FeTPP system.[46] We recently attempted this experiment while also hoping to reproduce the QD/FeTPP results but were unable to observe ultrafast ET in either system. This could be due to a number of factors, including the presence or absence of excess MPO ligands (see Scheme 3.2) and may be worth further exploration. Another interesting avenue would be to study binding of a Zn porphyrin with functional groups that would clearly bind to QDs, such as carboxylates. This would enable measurement of T_2 for the porphyrin with more confidence that the porphyrin is bound to the QD surface. If the change in T_2 is similar to the change observed with ZnTPP (see Figure 3.9), it could lend credence to the hypothesis that ZnTPP is bound to QD surfaces.

5.2.5   Intramolecular substrates for aza Paterno-Buchi [2+2] at QD surfaces

The challenges in achieving a TT-EnT-mediated intermolecular [2+2] cycloaddition between imines (or oximes) and olefins at QD surfaces outlined in Chapter 4 suggest it could be beneficial to investigate intramolecular reactions of substrates containing the imine and olefin moieties on the same molecule, despite their obvious synthetic limitations. As previously discussed in Chapter 4, intramolecular substrates have previously been used to mitigate the effect of fast isomerization of imines from their triplet excited states, which prevents [2+2] cycloaddition from occurring. As our work showed, QDs easily sensitize the triplet states of aromatic oximes, even when the QDs'

triplet energies are below those of the oximes', likely due to non-vertical energy transfer. The oximes then go on to rapidly isomerize rather than participate in cycloaddition. If QDs can successfully mediate [2+2] cycloaddition in an intramolecular substrate of similar design, such as the one shown in Figure 5.1, the result would confirm that [2+2] aza Paterno-Buchi reactions can in fact occur at QD surfaces. This would show that there aren't any other QD EnT or surface effects that prevent coupling from occurring, at least in an intramolecular substrate, and would provide motivation to continue work towards an intermolecular reaction at QD surfaces. The location of the binding group could also be altered, or multiple binding groups could be used, as shown in Figure 5.1. Due to the nature of TT-EnT from QDs to bound substrates, in which orbital
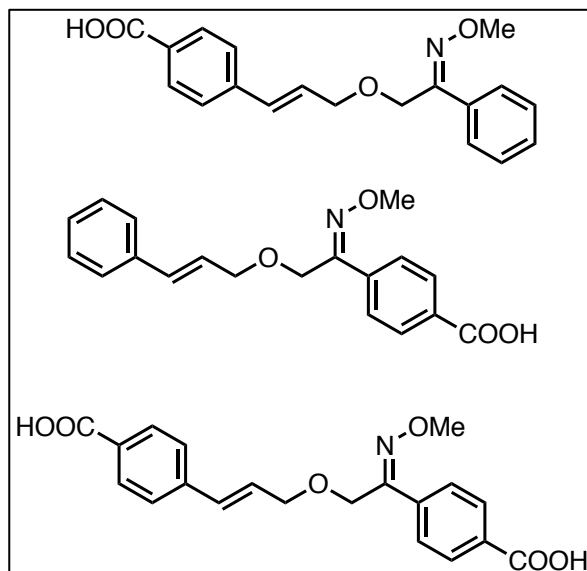
Figure 5.1. Proposed structures for intramolecular substrate for [2+2] aza Paterno-Buchi reaction at QD surfaces.

overlap between QD and acceptor is likely required, this might affect whether or not the oxime moiety is sensitized and undergoes isomerization *vs.* cycloaddition to the olefin moiety.

5.2.6   Continued investigation of olefin and imine substrate binding at QD surfaces

A presumable key to successful [2+2] cycloaddition with QDs is the co-localization of both substrates at the QD surface. The work discussed in Chapter 4 generally followed reaction conditions used in olefin-olefin cycloadditions at QD surfaces.[69] However, this assumes similar binding affinities between olefins and imines. If the binding affinity is much higher for olefins than imines, as our work may suggest (see Section 4.3.3), the probability of an imine and olefin binding next to each other, a requirement for successful cycloaddition, is very low and the reaction

will not occur. Measuring the binding affinities of olefin and imine substrates to QDs using ^{1}H NMR spectroscopy[80] would therefore provide further insight on whether or not substrates are likely to co-localize under the given reaction conditions. This work could direct redesign of the reaction conditions, particularly equivalents of each substrate per QD, which could lead to successful aza Paterno-Buchi reactivity.

5.2.7   *Alternative methods of substrate localization in QD-mediated aza Paterno-Buchi reaction*

Thus far the substrate scope of QD-mediated TT-EnT [2+2] cycloadditions between olefins has been limited to substrates with carboxylate groups that bind to QD surfaces. The work towards a QD-mediated aza Paterno-Buchi reaction presented in Chapter 4 also remained within this scope. However, other methods of substrate localization could be envisioned,[92] which may expand the substrate scope while retaining the advantages of using QDs in this reaction, mainly high regio- and diastereoselectivity. For example, TT-EnT from QDs to anthracene derivatives tethered by phosphonate ligands has recently been demonstrated.[93] Amines are also known to bind to QD surfaces and could be another alternative option for substrate design. These options increase the potential substrate scope and may exhibit less of the undesired side reactivity observed in some oxime carboxylates (see Figure 4.10). Finally, QDs could be prepared with ligands that can hydrogen bond to substrates. Bach and coworkers recently demonstrated that this is an effective method for enantioselective synthesis of azetidines mediated by organic dyes.[82] Imine substrates would require hydrogen bonding sites but no carboxylate group, which again might decrease the chance of side reactions.

5.2.8   *Study of non-vertical triplet energy transfer from QDs to aromatic oximes*

As discussed in Chapter 4, energy transfer from QDs to the aromatic oxime **1** appears to occur via a non-vertical energy transfer (NVET) mechanism. This phenomenon could be further

explored. The easy tunability of the triplet energy of QDs simply by changing their size would allow one to easily study the change in rate of TT-EnT from QDs to **1** as a function of triplet energy. Similar studies have been performed with transition metals complexes of varying triplet energy but the tunability of QDs may allow for more useful data points to be collected. The rate of TT-EnT could be measured by observing the rate of QD ground state bleach decay in transient absorption spectroscopy, and possibly by direct observation of absorption by the triplet state of **1**, if it does not overlap with QD features. The experiments could also be conducted at low temperature to see if the thermal contributions to TT-EnT can be suppressed.

Appendix A: Cyclic Voltammetry of Silyl Bis Enol Ethers

A.1 Introduction

This section describes the electrochemical characterization of a series of silyl bis enol ethers by cyclic voltammetry. Oxidation of these compounds using cerium ammonium nitrate (CAN) results in 1,4-diketones with high diastereoselectivity, as shown in Scheme 1.[94] Recently, we found that this reaction can also proceed via electrochemical or photocatalytic methods. We used cyclic voltammetry to i) estimate the oxidation potentials of our substrates and inform photocatalyst selection (see Section 1.3.2) and ii) use the cyclic voltammograms obtained to glean further insight into the reactivity of the complex under chemical, electrochemical, and photocatalytic conditions. The full results are in preparation and we hope to submit them for publication shortly.
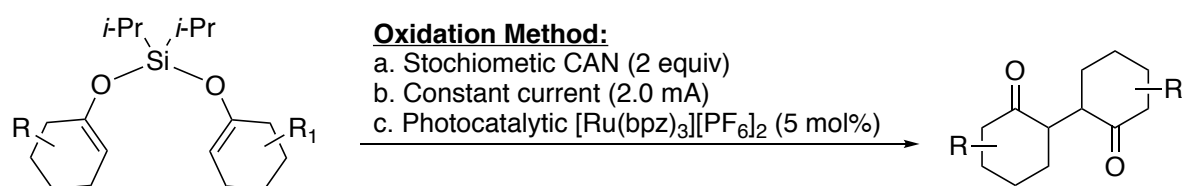
Scheme A.1. Reaction scheme for oxidation of silyl bis enol ethers by a) chemical oxidation, b) electrochemical oxidation, or c) photocatalytic oxidation.

A.2 Results and Discussion

The cyclic voltammograms of substrates 8a-8o are shown in Figures A.1-A.3. All voltammograms were collected by dissolving the substrates in 6:1 anhydrous, distilled MeCN:EtCN with 100 mM tetrabutylammonium hexafluorophosphate, degassing with nitrogen, and immersing a three electrode system (glassy carbon working electrode, platinum counter electrode, silver pseudoreference electrode). The voltammagram potentials were referenced by addition of the internal standard ferrocene or decamethylferrocene (not shown in figures for clarity). They appeared to fall into three general categories, characterized by i) single large oxidative waves, ii) two successive oxidative waves, and iii) poorly defined oxidative waves. All
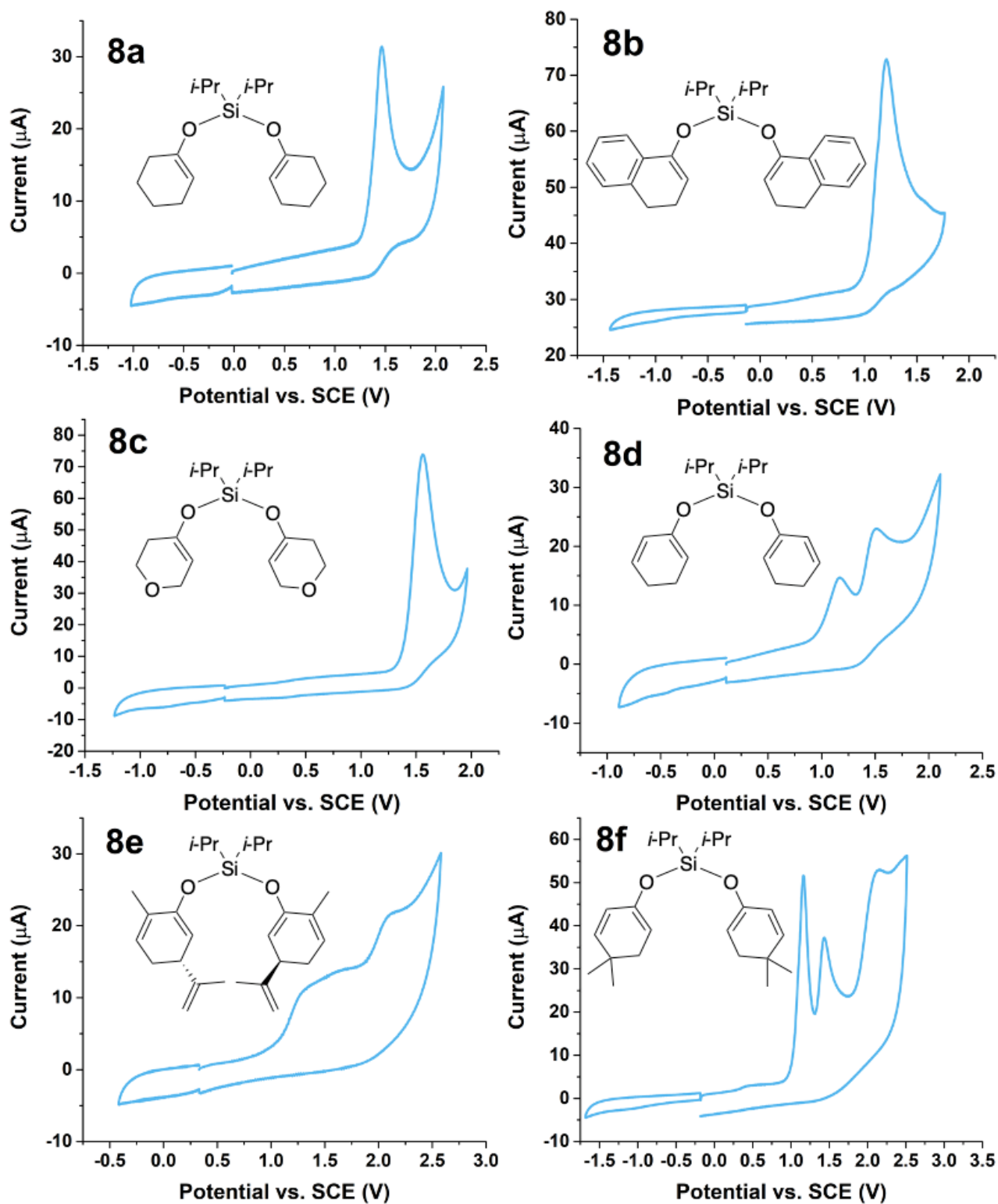
Figure A.1. Cyclic voltammograms of substrates 8a through 8f, collected at 50 mV/s scan rate in 6:1 MeCN:EtCN with 100 mM TBAPF$_6$ supporting electrolyte, using a glassy carbon working electrode, platinum wire counter electrode, and silver wire pseudoreference electrode (corrected by addition of ferrocene or decamethylferrocene, not shown for clarity).

compounds had oxidative waves above ca. +2.0 V vs. SCE but at such high potentials this could
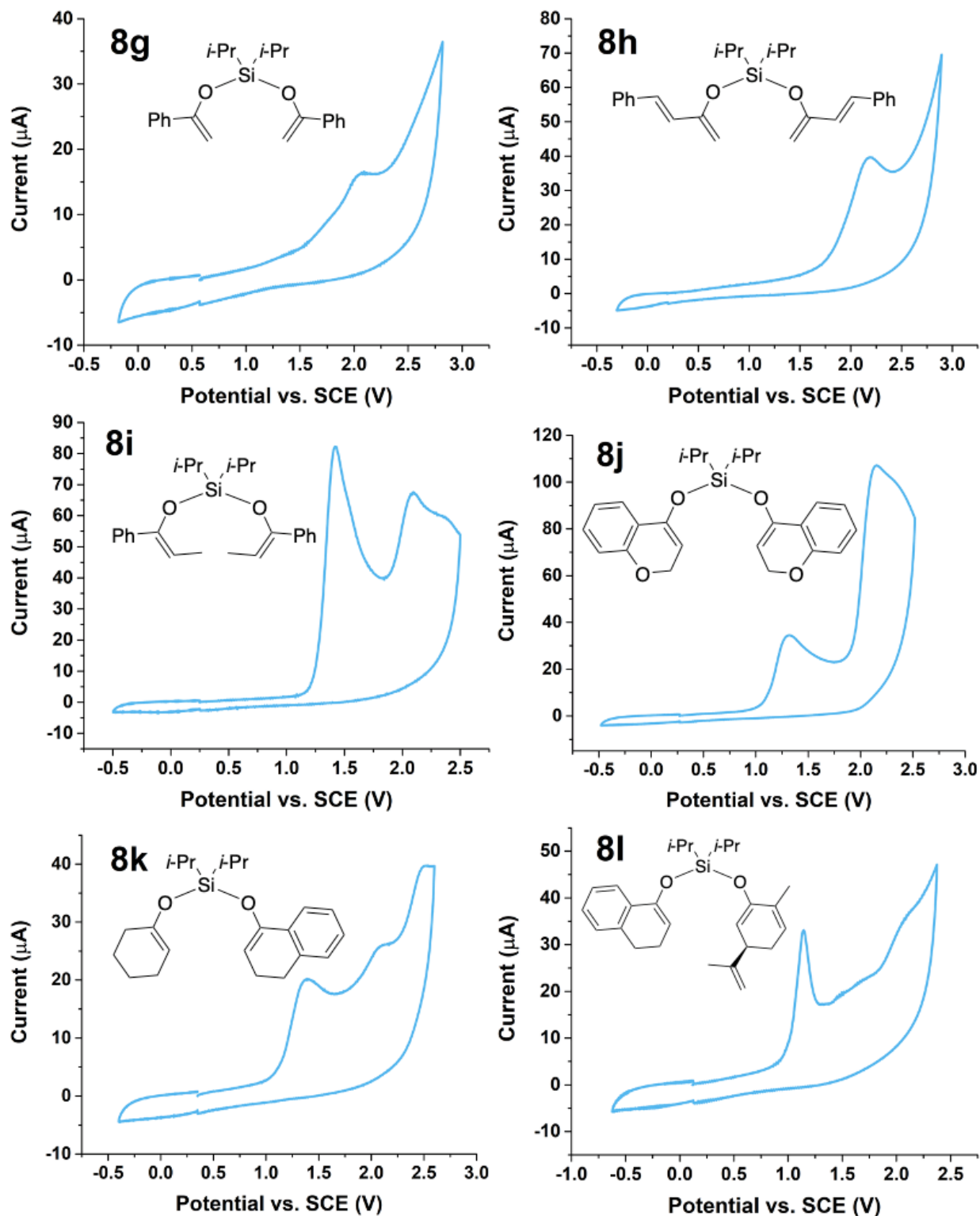
Figure A.2. Cyclic voltammograms of substrates 8g through 8l, collected at 50 mV/s scan rate in 6:1 MeCN:EtCN with 100 mM TBAPF$_6$ supporting electrolyte, using a glassy carbon working electrode, platinum wire counter electrode, and silver wire pseudoreference electrode (corrected by addition of ferrocene or decamethylferrocene, not shown for clarity).

quite likely be due to aromatic C-H bond oxidation.[95] The single large oxidative waves are likely
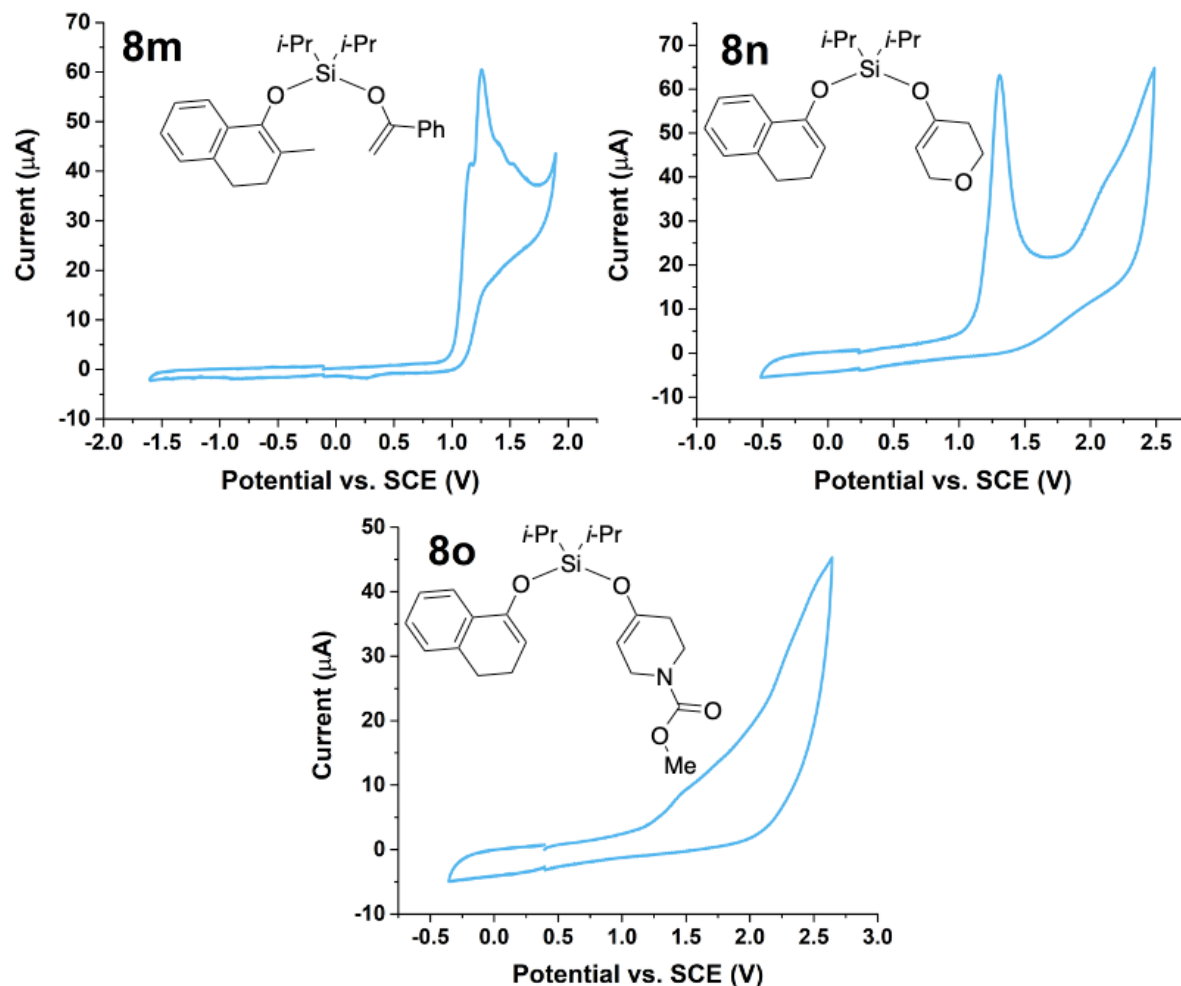
Figure A.3. Cyclic voltammograms of substrates 8m through 8o, collected at 50 mV/s scan rate in 6:1 MeCN:EtCN with 100 mM TBAPF$_6$ supporting electrolyte, using a glassy carbon working electrode, platinum wire counter electrode, and silver wire pseudoreference electrode (corrected by addition of ferrocene or decamethylferrocene, not shown for clarity).

two electron oxidations occurring at the same or very similar potentials; substrate 8m is a good example in which two peaks appear to clearly be nearly overlapping. Poorly defined waves appeared to occur for substrates that had multiple functional groups that might be oxidized in the potential window, such as substrates 8o and 8e. We are still in the process of rationalizing our chemical and electrochemical results in the context of these data. However, we did observe that, as expected, the photocatalyst used in our study, Ru(bpz)$_3{}^{2+}$, was unable to oxidize substrates above a certain potential, ca. +1.45 V vs. SCE, above which the reduction potential and excited state energy of the photocatalyst are insufficient to drive spontaneous electron transfer.[9] As

aforementioned, our full synthetic results will be reported in an upcoming publication (as well as in Aidan Caravana's thesis).

A.3 Experimental Details

A.3.1 Substrate synthesis

Substrates were synthesized by Aidan Caravana (Thomson Lab) using established procedures or adaptations of established procedures.[96] Synthetic data will be reported in an upcoming publication and/or in Aidan's thesis work.

A.3.2 Cyclic voltammetry

Cyclic voltammetry was performed using a Princeton Applied Instruments VERSASTAT 3 potentiostat. All samples were dissolved in distilled, anhydrous 6:1 MeCN:EtCN with 100 mM tetrabutylammonium hexafluorophosphate (TBAPF$_6$) supporting electrolyte and degassed with N$_2$ before measurement. A three-electrode setup was used, with glassy carbon as the working electrode, a platinum wire as the counter electrode, and a silver wire as a pseudoreference electrode. The voltammograms were collected at a scan rate of 50 mV/s and internally referenced to ferrocene or decamethylferrocene, which was dissolved in the analyte solutions, and then referenced to SCE based on the potential of the ferrocene or decamethylferrocene couple.

References

1.   Lakowicz, J. R., *Principles of Fluorescence Spectroscopy*. 3rd ed.; Springer: 2006.

2.   Lewis, N. S.; Nocera, D. G., Powering the planet: chemical challenges in solar energy utilization. *Proc. Natl. Acad. Sci. U. S. A.* **2006,** *103* (43), 15729-15735.

3.   Climate Change 2014: Synthesis Report. Contribution of Working Groups I, II and III to the Fifth Assessment Report of the Intergovernmental Panel on Climate Change. Intergovernmental Panel on Climate Change: Geneva, Switzerland, 2014.

4.   Noyori, R., Insight: Green chemistry: the key to our future. *Tetrahedron* **2010,** *66* (5), 1028.

5.   Schultz, D. M.; Yoon, T. P., Solar Synthesis: Prospects in Visible Light Photocatalysis. *Science* **2014,** *343* (6174), 1239176.

6.   Romero, N. A.; Nicewicz, D. A., Organic Photoredox Catalysis. *Chem. Rev.* **2016,** *116* (17), 10075-10166.

7.   Strieth-Kalthoff, F.; James, M. J.; Teders, M.; Pitzer, L.; Glorius, F., Energy transfer catalysis mediated by visible light: principles, applications, directions. *Chem. Soc. Rev.* **2018,** *47* (19), 7190-7202.

8.   Zhou, Q. Q.; Zou, Y. Q.; Lu, L. Q.; Xiao, W. J., Visible-Light-Induced Organic Photochemical Reactions through Energy-Transfer Pathways. *Angew. Chem., Int. Ed.* **2019,** *58* (6), 1586-1604.

9.   Prier, C. K.; Rankic, D. A.; MacMillan, D. W., Visible light photoredox catalysis with transition metal complexes: applications in organic synthesis. *Chem. Rev.* **2013,** *113* (7), 5322-5363.

10.   Shaw, M. H.; Twilton, J.; MacMillan, D. W., Photoredox Catalysis in Organic Chemistry. *J. Org. Chem.* **2016,** *81* (16), 6898-6926.

11.   Berardi, S.; Drouet, S.; Francas, L.; Gimbert-Surinach, C.; Guttentag, M.; Richmond, C.; Stoll, T.; Llobet, A., Molecular artificial photosynthesis. *Chem. Soc. Rev.* **2014,** *43* (22), 7501-19.

12.   Harris, R. D.; Bettis Homan, S.; Kodaimati, M.; He, C.; Nepomnyashchii, A. B.; Swenson, N. K.; Lian, S.; Calzada, R.; Weiss, E. A., Electronic Processes within Quantum Dot-Molecule Complexes. *Chem. Rev.* **2016,** *116* (21), 12865-12919.

13.   Zhang, Z.; Edme, K.; Lian, S.; Weiss, E. A., Enhancing the Rate of Quantum-Dot-Photocatalyzed Carbon-Carbon Coupling by Tuning the Composition of the Dot's Ligand Shell. *J. Am. Chem. Soc.* **2017,** *139* (12), 4246-4249.

14.   Knowles, K. E.; Tagliazucchi, M.; Malicki, M.; Swenson, N. K.; Weiss, E. A., Electron Transfer as a Probe of the Permeability of Organic Monolayers on the Surfaces of Colloidal PbS Quantum Dots. *J. Phys. Chem. C* **2013,** *117* (30), 15849-15857.

15.   Weiss, E. A., Designing the Surfaces of Semiconductor Quantum Dots for Colloidal Photocatalysis. *ACS Energy Lett.* **2017,** *2* (5), 1005-1013.

16.   Jiang, Y.; Weiss, E. A., Colloidal Quantum Dots as Photocatalysts for Triplet Excited State Reactions of Organic Molecules. *J. Am. Chem. Soc.* **2020,** *142* (36), 15219-15229.

17.   Detz, R. J.; Reek, J. N. H.; van der Zwaan, B. C. C., The future of solar fuels: when could they become competitive? *Energy Environ. Sci.* **2018,** *11* (7), 1653-1669.

18.   Kumar, B.; Llorente, M.; Froehlich, J.; Dang, T.; Sathrum, A.; Kubiak, C. P., Photochemical and photoelectrochemical reduction of CO_2. *Annu. Rev. Phys. Chem.* **2012,** *63*, 541-569.

19.   White, J. L.; Baruch, M. F.; Pander Iii, J. E.; Hu, Y.; Fortmeyer, I. C.; Park, J. E.; Zhang, T.; Liao, K.; Gu, J.; Yan, Y.; Shaw, T. W.; Abelev, E.; Bocarsly, A. B., Light-Driven Heterogeneous Reduction of Carbon Dioxide: Photocatalysts and Photoelectrodes. *Chem. Rev.* **2015,** *115* (23), 12888-12935.

20.   Takeda, H.; Cometto, C.; Ishitani, O.; Robert, M., Electrons, Photons, Protons and Earth-Abundant Metal Complexes for Molecular Catalysis of CO_2 Reduction. *ACS Catal.* **2016,** *7* (1), 70-88.

21.   Morris, A. J.; Meyer, G. J.; Fujita, E., Molecular approaches to the photocatalytic reduction of carbon dioxide for solar fuels. *Acc. Chem. Res.* **2009,** *42* (12), 1983-1994.

22.   Lehn, J.-M., Perspectives in Supramolecular Chemistry—From Molecular Recognition towards Molecular Information Processing and Self-Organization. *Angew. Chem., Int. Ed.* **1990,** *29* (11), 1304-1319.

23.   Krieg, E.; Bastings, M. M.; Besenius, P.; Rybtchinski, B., Supramolecular Polymers in Aqueous Media. *Chem. Rev.* **2016,** *116* (4), 2414-2477.

24.   Aida, T.; Meijer, E. W.; Stupp, S. I., Functional supramolecular polymers. *Science* **2012,** *335* (6070), 813-817.

25.   Boles, M. A.; Engel, M.; Talapin, D. V., Self-Assembly of Colloidal Nanocrystals: From Intricate Structures to Functional Materials. *Chem. Rev.* **2016,** *116* (18), 11220-11289.

26.   Hoeben, F. J.; Jonkheijm, P.; Meijer, E. W.; Schenning, A. P., About supramolecular assemblies of pi-conjugated systems. *Chem. Rev.* **2005,** *105* (4), 1491-1546.

27.   Wurthner, F.; Saha-Moller, C. R.; Fimmel, B.; Ogi, S.; Leowanawat, P.; Schmidt, D., Perylene Bisimide Dye Assemblies as Archetype Functional Supramolecular Materials. *Chem. Rev.* **2016,** *116* (3), 962-1052.

28.   Kodaimati, M. S.; Lian, S.; Schatz, G. C.; Weiss, E. A., Energy transfer-enhanced photocatalytic reduction of protons within quantum dot light-harvesting-catalyst assemblies. *Proc. Natl. Acad. Sci. U. S. A.* **2018,** *115* (33), 8290-8295.

29.   Wang, C.; Kodaimati, M. S.; Schatz, G. C.; Weiss, E. A., The photoluminescence spectral profiles of water-soluble aggregates of PbS quantum dots assembled through reversible metal coordination. *Chem. Commun.* **2017,** *53* (12), 1981-1984.

30.   Kundu, S.; Patra, A., Nanoscale Strategies for Light Harvesting. *Chem. Rev.* **2017,** *117* (2), 712-757.

31.   Lian, S.; Kodaimati, M. S.; Weiss, E. A., Photocatalytically Active Superstructures of Quantum Dots and Iron Porphyrins for Reduction of CO_2 to CO in Water. *ACS Nano* **2018,** *12* (1), 568-575.

32.   Bi, Q.-Q.; Wang, J.-W.; Lv, J.-X.; Wang, J.; Zhang, W.; Lu, T.-B., Selective Photocatalytic CO_2 Reduction in Water by Electrostatic Assembly of CdS Nanocrystals with a Dinuclear Cobalt Catalyst. *ACS Catal.* **2018,** *8* (12), 11815-11821.

33.   Arcudi, F.; Dordevic, L.; Nagasing, B.; Stupp, S. I.; Weiss, E. A., Quantum Dot-sensitized Photoreduction of CO_2 in Water with Turnover Number >80,000. *Submitted*.

34.   Weingarten, A. S.; Kazantsev, R. V.; Palmer, L. C.; McClendon, M.; Koltonow, A. R.; Samuel, A. P.; Kiebala, D. J.; Wasielewski, M. R.; Stupp, S. I., Self-assembling hydrogel scaffolds for photocatalytic hydrogen production. *Nat. Chem.* **2014,** *6* (11), 964-970.

35.   Weingarten, A. S.; Dannenhoffer, A. J.; Kazantsev, R. V.; Sai, H.; Huang, D.; Stupp, S. I., Chromophore Dipole Directs Morphology and Photocatalytic Hydrogen Generation. *J. Am. Chem. Soc.* **2018,** *140* (15), 4965-4968.

36.   Kazantsev, R. V.; Dannenhoffer, A. J.; Weingarten, A. S.; Phelan, B. T.; Harutyunyan, B.; Aytun, T.; Narayanan, A.; Fairfield, D. J.; Boekhoven, J.; Sai, H.; Senesi, A.; O'Dogherty, P. I.; Palmer, L. C.; Bedzyk, M. J.; Wasielewski, M. R.; Stupp, S. I., Crystal-Phase Transitions and Photocatalysis in Supramolecular Scaffolds. *J. Am. Chem. Soc.* **2017,** *139* (17), 6120-6127.

37.   Hestand, N. J.; Kazantsev, R. V.; Weingarten, A. S.; Palmer, L. C.; Stupp, S. I.; Spano, F. C., Extended-Charge-Transfer Excitons in Crystalline Supramolecular Photocatalytic Scaffolds. *J. Am. Chem. Soc.* **2016,** *138* (36), 11762-11774.

38.   Jiang, W.; Qian, H.; Li, Y.; Wang, Z., Heteroatom-Annulated Perylenes: Practical Synthesis, Photophysical Properties, and Solid-State Packing Arrangement. *J. Org. Chem.* **2008,** *73* (18), 7369-7372.

39.   Buendia, J.; Calbo, J.; Orti, E.; Sanchez, L., Flexible Chirality in Self-Assembled N-Annulated Perylenedicarboxamides. *Small* **2017,** *13* (20), 1603880.

40.   Looker, J. J., Mononitration of Perylene. Preparation and Structure Proof of the 1 and 3 Isomers. *J. Org. Chem.* **1972,** *37* (21), 3379-3381.

41.   Pick, A.; Klues, M.; Rinn, A.; Harms, K.; Chatterjee, S.; Witte, G., Polymorph-Selective Preparation and Structural Characterization of Perylene Single Crystals. *Cryst. Growth Des.* **2015,** *15* (11), 5495-5504.

42.   Costentin, C.; Robert, M.; Saveant, J. M.; Tatin, A., Efficient and selective molecular catalyst for the CO_2-to-CO electrochemical conversion in water. *Proc. Natl. Acad. Sci. U. S. A.* **2015,** *112* (22), 6882-6886.

43.   Rao, H.; Schmidt, L. C.; Bonin, J.; Robert, M., Visible-light-driven methane formation from CO_2 with a molecular iron catalyst. *Nature* **2017,** *548* (7665), 74-77.

44.   Rao, H.; Lim, C. H.; Bonin, J.; Miyake, G. M.; Robert, M., Visible-Light-Driven Conversion of CO_2 to CH_4 with an Organic Sensitizer and an Iron Porphyrin Catalyst. *J. Am. Chem. Soc.* **2018,** *140* (51), 17830-17834.

45.   Rao, H.; Bonin, J.; Robert, M., Visible-light Homogeneous Photocatalytic Conversion of CO_2 into CO in Aqueous Solutions with an Iron Catalyst. *ChemSusChem* **2017,** *10* (22), 4447-4450.

46.   Lian, S.; Kodaimati, M. S.; Dolzhnikov, D. S.; Calzada, R.; Weiss, E. A., Powering a CO_2 Reduction Catalyst with Visible Light through Multiple Sub-picosecond Electron Transfers from a Quantum Dot. *J. Am. Chem. Soc.* **2017,** *139* (26), 8931-8938.

47.   Bonin, J.; Robert, M.; Routier, M., Selective and Efficient Photocatalytic CO_2 Reduction to CO Using Visible Light and an Iron-Based Homogeneous Catalyst. *J. Am. Chem. Soc.* **2014,** *136* (48), 16768-16771.

48.   Fleischer, E. B.; Miller, C. K.; Webb, L. E., Crystal and Molecular Structures of Some Metal Tetraphenylporphines. *J. Am. Chem. Soc.* **1964,** *86* (12), 2342-2347.

49.   Collman, J. P.; Sorrell, T. N.; Hoffman, B. M., Models for Cytochrome P-450. *J. Am. Chem. Soc.* **1975,** *97* (4), 913-914.

50.   Collman, J. P.; Groh, S. E., "Mercaptan-tail" Porphyrins: Synthetic Analogs for the Active Site of Cytochrome P-450. *J. Am. Chem. Soc.* **1982,** *104* (5), 1391-1403.

51.   Costentin, C.; Robert, M.; Saveant, J. M., Catalysis of the electrochemical reduction of carbon dioxide. *Chem. Soc. Rev.* **2013,** *42* (6), 2423-36.

52.   Costentin, C.; Robert, M.; Saveant, J. M., Current Issues in Molecular Catalysis Illustrated by Iron Porphyrins as Catalysts of the CO_2-to-CO Electrochemical Conversion. *Acc. Chem. Res.* **2015,** *48* (12), 2996-3006.

53.   Kadish, K.; Smith, K. M.; Guilard, R., *The Porphyrin Handbook*. Elsevier: 2000.

54.   Jones, S. E.; Srivatsa, G. S.; Sawyer, D. T.; Traylor, T. G.; Mincey, T. C., Redox chemistry of iron tetraphenylporphyrin imidazolate-chelated protoheme, and of their iron(II)-superoxide adducts in dimethyl sulfoxide. *Inorg. Chem.* **1983,** *22* (26), 3903-3910.

55.   Kadish, K. M.; Larson, G.; Lexa, D.; Momenteau, M., Electrochemical and spectral characterization of the reduction steps of μ-oxo-bis(iron tetraphinylporphyrin) dimer in dimethylformamide. *J. Am. Chem. Soc.* **1975,** *97* (2), 282-288.

56.   Romelt, C.; Song, J.; Tarrago, M.; Rees, J. A.; van Gastel, M.; Weyhermuller, T.; DeBeer, S.; Bill, E.; Neese, F.; Ye, S., Electronic Structure of a Formal Iron(0) Porphyrin Complex Relevant to CO_2 Reduction. *Inorg. Chem.* **2017,** *56* (8), 4746-4751.

57.   Nolan, K. B., Spectroscopic models for cytochrome P-450 derivatives: hyperporphyrin spectra in thiolatoiron(III)–porphyrin complexes. *Chem. Commun.* **1986,** (10), 760-762.

58.   Boersma, A. D.; Goff, H. M., Multinuclear magnetic resonance spectroscopy of spin-admixed S = 5/2, 3/2 iron(III) porphyrins. *Inorg. Chem.* **1982,** *21* (2), 581-586.

59.   Fleischer, E. B.; Srivastava, T. S., Structure and Properties of μ-Oxobis(tetraphenylporphineiron(III). *J. Am. Chem. Soc.* **1969,** *91* (9), 2403-2405.

60.   So, D.; Konstantatos, G., Thiol-Free Synthesized Copper Indium Sulfide Nanocrystals as Optoelectronic Quantum Dot Solids. *Chem. Mater.* **2015,** *27* (24), 8424-8432.

61.   Zhang, Y.; Fry, C. G.; Pedersen, J. A.; Hamers, R. J., Dynamics and Morphology of Nanoparticle-Linked Polymers Elucidated by Nuclear Magnetic Resonance. *Anal. Chem.* **2017,** *89* (22), 12399-12407.

62.   De Roo, J.; Yazdani, N.; Drijvers, E.; Lauria, A.; Maes, J.; Owen, J. S.; Van Driessche, I.; Niederberger, M.; Wood, V.; Martins, J. C.; Infante, I.; Hens, Z., Probing Solvent–Ligand Interactions in Colloidal Nanocrystals by the NMR Line Broadening. *Chem. Mater.* **2018,** *30* (15), 5485-5492.

63.   Wu, M.; Vartanian, A. M.; Chong, G.; Pandiakumar, A. K.; Hamers, R. J.; Hernandez, R.; Murphy, C. J., Solution NMR Analysis of Ligand Environment in Quaternary Ammonium-Terminated Self-Assembled Monolayers on Gold Nanoparticles: The Effect of Surface Curvature and Ligand Structure. *J. Am. Chem. Soc.* **2019,** *141* (10), 4316-4327.

64.   Henckel, D. A.; Enright, M. J.; Panahpour Eslami, N.; Kroupa, D. M.; Gamelin, D. R.; Cossairt, B. M., Modeling Equilibrium Binding at Quantum Dot Surfaces Using Cyclic Voltammetry. *Nano Lett.* **2020,** *20* (4), 2620-2624.

65.   Mongin, C.; Garakyaraghi, S.; Razgoniaeva, N.; Zamkov, M.; Castellano, F. N., Direct observation of triplet energy transfer from semiconductor nanocrystals. *Science* **2016,** *351* (6271), 369-372.

66.   Okumura, K.; Mase, K.; Yanai, N.; Kimizuka, N., Employing Core-Shell Quantum Dots as Triplet Sensitizers for Photon Upconversion. *Chem-Eur J* **2016,** *22* (23), 7721-7726.

67.   Huang, Z. Y.; Tang, M. L., Designing Transmitter Ligands That Mediate Energy Transfer between Semiconductor Nanocrystals and Molecules. *J. Am. Chem. Soc.* **2017,** *139* (28), 9412-9418.

68.   Han, Y.; He, S.; Luo, X.; Li, Y.; Chen, Z.; Kang, W.; Wang, X.; Wu, K., Triplet Sensitization by "Self-Trapped" Excitons of Nontoxic $CuInS_2$ Nanocrystals for Efficient Photon Upconversion. *J. Am. Chem. Soc.* **2019,** *141* (33), 13033-13037.

69.   Jiang, Y.; Wang, C.; Rogers, C. R.; Kodaimati, M. S.; Weiss, E. A., Regio- and diastereoselective intermolecular [2+2] cycloadditions photocatalysed by quantum dots. *Nat. Chem.* **2019,** *11* (11), 1034-1040.

70.   Vitaku, E.; Smith, D. T.; Njardarson, J. T., Analysis of the Structural Diversity, Substitution Patterns, and Frequency of Nitrogen Heterocycles Among U.S. FDA Approved Pharmaceuticals. *J. Med. Chem.* **2014,** *57* (24), 10257-10274.

71.   Richardson, A. D.; Becker, M. R.; Schindler, C. S., Synthesis of azetidines by aza Paterno-Buchi reactions. *Chem. Sci.* **2020,** *11* (29), 7553-7561.

72.   D'Auria, M., The Paterno-Buchi reaction - a comprehensive review. *Photochem. Photobiol. Sci.* **2019,** *18* (10), 2297-2362.

73.   Pratt, A. C., The photochemistry of imines. *Chem. Soc. Rev.* **1977,** *6* (1), 63-81.

74.   Padwa, A., Photochemistry of the carbon-nitrogen double bond. *Chem. Rev.* **1977,** *77* (1), 37-68.

75.   Howard, K. A.; Koch, T. H., Photochemical Reactivity of Keto Imino Ethers. V. (2 + 2) Photocycloaddition to the Carbon-Nitrogen Double Bond of 3-Ethoxyisoindolone. *J. Am. Chem. Soc.* **1975,** *97* (25), 7288-7298.

76.   Becker, M. R.; Wearing, E. R.; Schindler, C. S., Synthesis of azetidines via visible-light-mediated intermolecular [2+2] photocycloadditions. *Nat. Chem.* **2020,** *12* (10), 898-905.

77.   Kumarasamy, E.; Kandappa, S. K.; Raghunathan, R.; Jockusch, S.; Sivaguru, J., Realizing an Aza Paterno-Buchi Reaction. *Angew. Chem., Int. Ed.* **2017,** *56* (25), 7056-7061.

78.   Becker, M. R.; Richardson, A. D.; Schindler, C. S., Functionalized azetidines via visible light-enabled aza Paterno-Buchi reactions. *Nat. Commun.* **2019,** *10* (1), 5095.

79.   Lalevée, J.; Allonas, X.; Louërat, F.; Fouassier, J. P., Role of Structural Changes in the Triplet−Triplet Energy Transfer Process to Oxime Derivatives. *J. Phys. Chem. A* **2002,** *106* (29), 6702-6709.

80.   Hens, Z.; Martins, J. C., A Solution NMR Toolbox for Characterizing the Surface Chemistry of Colloidal Nanocrystals. *Chem. Mater.* **2013,** *25* (8), 1211-1221.

81.   Sakamoto, R.; Inada, T.; Sakurai, S.; Maruoka, K., [2 + 2] Photocycloadditions between the Carbon-Nitrogen Double Bonds of Imines and Carbon-Carbon Double Bonds. *Org. Lett.* **2016,** *18* (24), 6252-6255.

82.   Li, X.; Grosskopf, J.; Jandl, C.; Bach, T., Enantioselective, Visible Light-mediated Aza Paterno-Buchi Reactions of Quinoxalinones. *Angew. Chem., Int. Ed.* **2020**, DOI: 10.1002/anie.202013276.

83.   Flamee, S.; Cirillo, M.; Abe, S.; De Nolf, K.; Gomes, R.; Aubert, T.; Hens, Z., Fast, High Yield, and High Solid Loading Synthesis of Metal Selenide Nanocrystals. *Chem. Mater.* **2013,** *25* (12), 2476-2483.

84.   Li, J. J.; Wang, Y. A.; Guo, W.; Keay, J. C.; Mishima, T. D.; Johnson, M. B.; Peng, X., Large-Scale Synthesis of Nearly Monodisperse CdSe/CdS Core/Shell Nanocrystals Using Air-Stable Reagents via Successive Ion Layer Adsorption and Reaction. *J. Am. Chem. Soc.* **2003,** *125* (41), 12567-12575.

85.   Chen, D.; Zhao, F.; Qi, H.; Rutherford, M.; Peng, X., Bright and Stable Purple/Blue Emitting CdS/ZnS Core/Shell Nanocrystals Grown by Thermal Cycling Using a Single-Source Precursor. *Chem. Mater.* **2010,** *22* (4), 1437-1444.

86.   Gong, T. J.; Xiao, B.; Cheng, W. M.; Su, W.; Xu, J.; Liu, Z. J.; Liu, L.; Fu, Y., Rhodium-Catalyzed Directed C-H Cyanation of Arenes with *N*-Cyano-*N*-phenyl-*p*-toluenesulfonamide. *J. Am. Chem. Soc.* **2013,** *135* (29), 10630-10633.

87.   Marinković, A. D.; Jovanović, B. Ž.; Assaleh, F. H.; Vajs, V. V.; Juranić, M. I., Linear free energy relationships applied to the reactivity and the ^{13}C NMR chemical shifts in 4-[[(substituted phenyl)imino]methyl]benzoic acids. *J. Mol. Struct.* **2012,** *1011*, 158-165.

88.   Albert, J.; D'Andrea, L. a.; Bautista, J. s.; González, A.; Granell, J.; Font-Bardia, M.; Calvet, T., Unexpected Structure of Palladacycles Containing Carboxylated Schiff Bases. Synthesis of Some Water-Soluble Metallacycles. *Organometallics* **2008,** *27* (19), 5108-5117.

89.   Anorma, C.; Hedhli, J.; Bearrood, T. E.; Pino, N. W.; Gardner, S. H.; Inaba, H.; Zhang, P.; Li, Y.; Feng, D.; Dibrell, S. E.; Kilian, K. A.; Dobrucki, L. W.; Fan, T. M.; Chan, J., Surveillance of Cancer Stem Cell Plasticity Using an Isoform-Selective Fluorescent Probe for Aldehyde Dehydrogenase 1A1. *ACS. Cent. Sci.* **2018,** *4* (8), 1045-1055.

90.   Kozikowski, A. P.; Adamcz, M., Methods for the Stereoselective cis-Cyanohydroxylation and -Carboxyhydroxylation of Olefins. *J. Org. Chem.* **1983,** *48* (3), 366-372.

91.   Martinez, C. R.; Iverson, B. L., Rethinking the term "pi-stacking". *Chem. Sci.* **2012,** *3* (7).

92.   Owen, J., Nanocrystal structure. The coordination chemistry of nanocrystal surfaces. *Science* **2015,** *347* (6222), 615-616.

93.   De Roo, J.; Huang, Z.; Schuster, N. J.; Hamachi, L. S.; Congreve, D. N.; Xu, Z.; Xia, P.; Fishman, D. A.; Lian, T.; Owen, J. S.; Tang, M. L., Anthracene Diphosphate Ligands for CdSe Quantum Dots; Molecular Design for Efficient Upconversion. *Chem. Mater.* **2020,** *32* (4), 1461-1466.

94.   Guo, F.; Clift, M. D.; Thomson, R. J., Oxidative Coupling of Enolates, Enol Silanes and Enamines: Methods and Natural Product Synthesis. *Eur. J. Org. Chem.* **2012,** *2012* (26), 4881-4896.

95.   Weinberg, N. L.; Weinberg, H. R., Electrochemical oxidation of organic compounds. *Chem. Rev.* **1968,** *68* (4), 449-523.

96.   Avetta, C. T., Jr.; Konkol, L. C.; Taylor, C. N.; Dugan, K. C.; Stern, C. L.; Thomson, R. J., Diastereoselective Oxidative Carbon-Carbon Bond Formation via Silyl Bis-enol Ethers. *Org. Lett.* **2008,** *10* (24), 5621-5624.